National Library
of Canada

Acquisitions and
Bibliographic Services Branch

395 Wellington Street
Ottawa, Ontario
K1A 0N4

Bibliothèque nationale
du Canada

Direction des acquisitions et
des services bibliographiques

395, rue Wellington
Ottawa (Ontario)
K1A 0N4

Your file Votre référence

Our file Notre référence

NOTICE

The quality of this microform is heavily dependent upon the quality of the original thesis submitted for microfilming. Every effort has been made to ensure the highest quality of reproduction possible.

If pages are missing, contact the university which granted the degree.

Some pages may have indistinct print especially if the original pages were typed with a poor typewriter ribbon or if the university sent us an inferior photocopy.

Reproduction in full or in part of this microform is governed by the Canadian Copyright Act, R.S.C. 1970, c. C-30, and subsequent amendments.

AVIS

La qualité de cette microforme dépend grandement de la qualité de la thèse soumise au microfilmage. Nous avons tout fait pour assurer une qualité supérieure de reproduction.

S'il manque des pages, veuillez communiquer avec l'université qui a conféré le grade.

La qualité d'impression de certaines pages peut laisser à désirer, surtout si les pages originales ont été dactylographiées à l'aide d'un ruban usé ou si l'université nous a fait parvenir une photocopie de qualité inférieure.

La reproduction, même partielle, de cette microforme est soumise à la Loi canadienne sur le droit d'auteur, SRC 1970, c. C-30, et ses amendements subséquents.

Canada

Properties and Applications of Rare-Earth-Doped Fiber Amplifiers and Lasers

Chris Barnard, B.A.Sc., M.Sc.
12 February 1994

A thesis
submitted to the School of Graduate Studies and Research
in partial fulfilment of the requirements for the
Degree of Doctor of Philosophy
in Electrical Engineering

Ottawa-Carleton Institute for Electrical Engineering
Department of Electrical Engineering
Faculty of Engineering
University of Ottawa
Ottawa, Ontario
Canada

National Library
of Canada

Acquisitions and
Bibliographic Services Branch

395 Wellington Street
Ottawa, Ontario
K1A 0N4

Bibliothèque nationale
du Canada

Direction des acquisitions et
des services bibliographiques

395, rue Wellington
Ottawa (Ontario)
K1A 0N4

Your file   Votre référence

Our file   Notre référence

The author has granted an irrevocable non-exclusive licence allowing the National Library of Canada to reproduce, loan, distribute or sell copies of his/her thesis by any means and in any form or format, making this thesis available to interested persons.

L'auteur a accordé une licence irrévocable et non exclusive permettant à la Bibliothèque nationale du Canada de reproduire, prêter, distribuer ou vendre des copies de sa thèse de quelque manière et sous quelque forme que ce soit pour mettre des exemplaires de cette thèse à la disposition des personnes intéressées.

The author retains ownership of the copyright in his/her thesis. Neither the thesis nor substantial extracts from it may be printed or otherwise reproduced without his/her permission.

L'auteur conserve la propriété du droit d'auteur qui protège sa thèse. Ni la thèse ni des extraits substantiels de celle-ci ne doivent être imprimés ou autrement reproduits sans son autorisation.

ISBN 0-315-93554-5

Canada

UNIVERSITÉ D'OTTAWA
UNIVERSITY OF OTTAWA

Abstract

An analytical model for two-, three-, and four-level system rare-earth-doped fiber amplifiers and lasers is presented. Fiber amplifier gain is expressed in terms of easily measured attenuation coefficients, intrinsic saturation powers, and cross saturation powers at the pump and signal wavelengths. System-independent formulas are given for the slopes and thresholds of ring and linear fiber lasers. Good agreement between theory and experiment is shown for erbium-doped fiber amplifiers and lasers and thulium-doped fiber lasers. Approximate system-independent solutions are also given for fiber amplifiers with excited state absorption at either the pump or signal wavelengths. A novel technique, requiring only one tunable light source, is proposed for finding the best pump wavelength when pump ESA is present. Analysis of erbium doped fiber amplifier (EDFA) gain and noise yields a new expression for the amplifier signal-to-noise ratio (SNR) as a function of the fiber length. This leads to a new expression for the fiber length that optimizes the output SNR.

Optical gain switching of EDFAs with short pulses at wavelengths within the amplifier bandwidth is modelled to determine how the pump and signal powers, pulse energy, fiber length, and dopant concentration affect the switching time and gain compression. Greater than 20 dB gain compression with nanosecond switching times is demonstrated with good agreement between theory and experiment. Remote EDFA switching from as far as 50 km away is demonstrated. The distance is limited by spontaneous Raman scattering of the switching pulses. These limitations are experimentally and theoretically investigated.

Novel configurations are proposed for bidirectional amplification in both single-mode fiber and polarization maintaining fiber. New frequency dependent optical isolators are demonstrated for OTDR testing of amplified fiber links. The new bidirectional amplifier design is much better at attenuating backreflections than a standard EDFA.

Polarization separated bidirectional fiber local area networks are proposed. Point-to-point and reflective N-star coupler networks where $N=M^2$ or $2M^2$ are considered for an integer M. Reflective star coupler networks use a novel proposed fiber device: an orthogonal polarization variable reflector which can act as an orthogonal polarization full or half reflector. A bidirectional fiber amplifier configuration for polarization separated signals is also proposed.

Acknowledgements

The work presented in this thesis was carried out at the Institute for Information Technology at the National Research Council of Canada, .

I am grateful to my supervisors, Drs. Jacek Chrostowski and Mohsen Kavehrad, for their interest, advice, and encouragement. I would also like to thank the members of my examining committee, Drs. David Gibbons, S. Iraj Najafi, Willem Steenaart, and Gary Tarr, for taking the time to read the thesis and for their helpful recommendations.

I am indebted to Dr. Piotr Myslinski for his continual encouragement, valuable suggestions and assistance, especially with the theoretical work of Chapter II, and the experimental work in Chapters IV and V. He conducted the initial experiments on EDFA gain switching reported in Section IV.2. Dr. Xing Pan measured the thulium-doped fiber laser output power reported in Section II.6. The experimental and computer work was made much easier with the technical help of Ross Misner and Alfred Dufour at the NRC. I am also grateful to Leslie Cameron and Paul Amirault at the NRC and Mirella Aiello at the University of Ottawa for their cheerful assistance with some of the figures, to Neil Teitelbaum for assisting with the patent applications, and to Evelyn Kidd at the NRC for proofreading Ref. [44]. For their interest and encouragement I also wish to thank my colleagues at the NRC and the University of Ottawa: Drs. Simon Boothroyd, Weiping Huang, Mansour Irshid, Quan Jiang, Piotr Myslinski, Paparao Palacharla, Xing Pan, Bill Robertson, Tsutomu Shimura, Ellie Simova, and Feng Zhang; and my fellow students at the University of Ottawa, Carleton University and the University of Waterloo: Les Chan, Glenn Cheney, J.P. Decruyenaere, Sudhakar Ghanti, Xin Huang, Noureldin Ibrahim, Farideh Khaleghi, Ryan McDonald, Nick Peereboom, Emil Savov, Nilofar Tayebi, Chenglin Xu, Suet Yuen, Gang Yun, and Denis Zaccarin.

Most importantly, thanks are given to my family for their encouragement and support and, above all, to my wife, Micheline Martin, and daughter, Trisha, for their constant reassurance and support.

Contents

List of Figures

List of Tables

List of Symbols and Abbreviations

Note: Subscripts p and s (replaced here by subscript k) denote values at the pump and signal wavelengths respectively

A_{eff}	Effective dopant area (m^2)
A_k	Normalized complex modal field amplitude at kth wavelength
a	Fiber core radius (m)
b	Dopant radius (m)
e	Electron charge (C)
F	Relative error between overlap integrals
G	Fiber amplifier gain
$\hat{G}$	Fiber amplifier gain at peak of noise spectrum
G_{max}	Maximum fiber amplifier gain
G_{net}	Net fiber amplifier gain
g_R	Raman gain coefficient (m/W)
$g(\nu)$	Normalized ionic lineshape function
h	Planck's constant (J/s)
I_k	Light intensity at kth wavelength (W/m^2)
k	Boltzmann's constant (J/K)
L	Fiber length (m)
L_{min}	Minimum fiber length (m)
L_{opt}	Optimum fiber length (m)
L_w	Walkoff length (m)
$^{2S+1}L_J$	Spectroscopic notation of ionic energy level
NA	Fiber numerical aperture
NF	Amplifier noise figure
NF_{opt}	Amplifier optimum noise figure
N_i	Dopant ions per unit volume in ith energy level (m^{-3})
N_e	Density of dopant ions in upper energy levels (m^{-3})
N_t	Total density of dopant ions (m^{-3})

n	Fiber refractive index
n_2	Nonlinear refractive index coefficient (m^2/W)
n_g	Fiber group refractive index
$\bar{n}_s$	Average number of signal photons in a given time interval
n_{sp}	Spontaneous emission factor
$\bar{n}_{sp}$	Integrated spontaneous emission factor
$\hat{n}_{sp}$	$\bar{n}_{sp}$ at the peak of the noise spectrum
P_{ASE}	Spontaneous emission power (W)
P_k^{ESA}	ESA saturation power at kth wavelength (s^{-1})
P_k^{IS}	Intrinsic saturation power at kth wavelength (s^{-1})
P_k^{abs}	Absorbed power in doped fiber at kth wavelength (s^{-1})
$P_{k,j}$	Power of jth beam at kth wavelength (s^{-1})
$P_{k,j}^{out}$	Output power of jth beam at kth wavelength (s^{-1})
$P_{k,j}^{in}$	Input power of jth beam at kth wavelength (s^{-1})
P_k^{CS}	Cross saturation power at kth wavelength (s^{-1})
P_{las}	Fiber laser output power (W)
P_p^{th}	Fiber laser pump power threshold (W)
P_L^{out}	Output power from left of doped fiber (s^{-1})
P_R^{out}	Output power from right of doped fiber (s^{-1})
P^x, P^y	Power in x-polarized and y-polarized components (W)
$P(n)$	Probability of detecting n photons
R_{eff}	Effective reflectance from discrete reflections and Rayleigh backscattering
q_k	Fiber intrinsic loss at kth wavelength (m^{-1})
r	Fiber radial coordinate (m)
R	Effective mirror reflectivity
R_i	Reflectivity of ith mirror
S_{ASE}	Spectral density of amplified spontaneous emission noise (W/Hz)
$\hat{S}_{ASE}$	Peak value of S_{ASE} (W/Hz)
S_{SE}	Spectral density of spontaneous emission noise (W/Hz)
T	Temperature (K)

T	Bit duration (s)
T_0	Pulse duration (s)
T_{eff}	Effective cavity output transmission
T_{FWHM}	Pulse duration (full-width at half maximum) (s)
T_k	Fiber transmission at kth wavelength
T_{max}	Maximum fiber transmission
T_{min}	Minimum fiber transmission
u_k	Unit vector in z direction of kth wavelength
v_g	Group velocity (m/s)
w	Fiber approximate Gaussian mode radius (m)
α_k	Attenuation coefficient at kth wavelength (m^{-1})
β_{ij}	Ratio of ion density of ith level to density of jth level for weak pumping
β_2	Fiber second order dispersion coefficient (s^2/m)
γ	Small signal gain coefficient (m^{-1})
γ	Fiber nonlinear coefficient ($\mathrm{m}^{-1}\mathrm{W}_{-1}$) (Chapter V)
Γ_i	Overlap integral of mode and dopant ions in ith energy level
δ	Saturation power ratio
Δ_{ASE}	Amplified spontaneous emission bandwidth (Hz)
Δ_{sp-sp}	Spontaneous-spontaneous beat noise bandwidth (Hz)
ΔE	Energy difference between two ionic states (J)
Δf	Raman gain bandwidth (Hz)
ΔT	Change in fiber transmission
ε_i	Transmission of ith cavity loss
ε	Effective cavity transmission (Chapter II)
ε	Ratio of emission cross section to emission cross section (Chapter III)
ζ_k^{IS}	Ratio of ESA saturation power to intrinsic saturation power at kth wavelength
η_i	Fiber amplifier input coupling efficiency
η_o	Fiber amplifier output coupling efficiency
η_p	Pump efficiency
η_q	Quantum efficiency

η	Fiber laser slope efficiency
κ	Power coupling coefficient
η_i	Amplifier input coupling coefficient
λ_k	Wavelength of kth beam (m)
$<\mu_{ASE}>$	Mean number of ASE photons in given time interval
ν_k	Free-space optical frequency of kth wavelength (Hz)
σ_c^2	Photodetector circuit noise density (A^2/Hz)
σ_k^a	Absorption cross section at kth wavelength (m^2)
σ_k^e	Emission cross section at kth wavelength (m^2)
σ_n^2	Variance in photon number
σ_{in}^2	Net amplifier input photon number variance
σ_{out}^2	Net amplifier output photon number variance
σ_k^{ESA}	Excited state absorption cross section at kth wavelength (m^2)
$\sigma^2_{sig\text{-}sh}$	Variance in photon number attributed to signal shot noise
$\sigma^2_{sig\text{-}sp}$	Variance in photon number attributed to signal-spontaneous beat noise
$\sigma^2_{sp\text{-}sh}$	Variance in photon number attributed to spontaneous shot noise
$\sigma^2_{sp\text{-}sp}$	Variance in photon number attributed to spontaneous-spontaneous beat noise
τ_{ij}	Spontaneous decay time from ith to jth energy level (s)
τ_i	Net spontaneous decay rate from ith energy level (s)
τ_{ESA}	Net spontaneous decay rate from ESA energy level (s)
ϕ	Detector decision threshold
$d\Omega$	Fiber acceptance solid angle
APC	Angle-polished connector
AR	Antireflection coating
ASE	Amplified spontaneous emission
CATV	Cable television
CW	Continuous wave
DFB	Distributed feedback
EDFA	Erbium-doped fiber amplifier
EDFL	Erbium-doped fiber laser

ESA	Excited state absorption
FBA	Fiber brillouin amplifier
FC/PC	Fiber connector with physical contact
FDOI	Frequency dependent optical isolator
FWHM	Full width at half maximum
HDTV	High-definition television
ISDN	Integrated services digital network
LAN	Local area network
LED	Light emitting diode
OBF	Optical bandpass filter
OI	Optical isolator
OPFR	Orthogonal polarization full reflector
OPHR	Orthogonal polarization half reflector
OPVR	Orthogonal polarization variable reflector
OTDR	Optical time domain reflectometry
PBS	Polarization beam splitter
PDFA	Praseodymium-doped fiber amplifier
PMDC	Polarization maintaining directional couplers
PMF	Polarization maintaining fiber
SBS	Stimulated Brillouin scattering
SNR	Signal-to-noise ratio
SOA	Semiconductor optical amplifier
SOP	State of polarization
SRS	Stimulated Raman scattering
TDM	Time division multiplexing
WDM	Wavelength division multiplexing
WSC	Wavelength selective coupler

Chapter I

Introduction

I.1 Optical Communications

Information services and products such as ISDN, electronic mail, computer communications, HDTV, interactive television, video conferences, and videophones are constantly being improved, installed, or forecast. Because of its immense bandwith (about 20 THz) and very low loss (about 0.25 dB/km), the medium that has the transmission capacity required by these applications is single-mode optical fiber. Along with its applications in communications, optical fiber is also used for sensing, medicine, optically enhanced computing, and laser sources. Fiber optic communications has evolved from a first generation which used 830 nm LEDs and multimode fiber yielding a transmission capacity of 1 Gb-km/s, to a second generation which used 1320 nm laser sources and single-mode fiber yielding a transmission capacity of almost 100 Gb-km/s, and then to a third generation which used 1550 nm laser sources and single-mode fiber yielding a transmission capacity of hundreds of Gb-km/s. Future generations may use one or more of the following technologies which are presently at the research stage: coherent optical detection, soliton transmission, dense wavelength division multiplexing, and optical switching and routing.

Although fiber loss is very low at 1550 nm, amplification is still necessary for long-haul communications and for distributing signals among millions of subscribers. One technology that has emerged is direct optical amplification. Optical amplifiers offer high gain, low noise, a virtually unlimited bandwidth (DC to THz), an ability to simultaneously amplify many multiplexed signals, and bit-rate and modulation format transparency. They have several applications such as replacing electronic repeaters in long-haul transmission lines and compensating for star coupler splitting loss in cable TV distribution networks [1].

I.2 Overview of Optical Amplifiers

In the last seven years, rapid advances have been made on rare-earth-doped single-mode fiber amplifiers and lasers [2]. Erbium-doped fiber amplifiers (EDFAs) have already established their key role for 1.55 μm optical communication networks. Research is now rapidly advancing on praseodymium and neodymium -doped fiber amplifiers for the 1.3 μm telecommunications window. Efficient amplification and lasing of light from 0.5 to 3 μm has also been shown with other rare-earth dopants. Competitors of rare-earth-doped fiber amplifiers include electrically pumped semiconductor optical amplifiers and optically pumped nonlinear fiber amplifiers employing stimulated Raman scattering, stimulated Brillouin scattering, or four wave mixing. For optical fiber communications the strongest contenders are the semiconductor optical amplifier (SOA) and the EDFA. Development of these devices is progressing rapidly as demand increases for fiber compatible amplifiers and lasers. A brief summary of the various amplifiers follows.

I.2.1 Semiconductor Optical Amplifiers

Semiconductor optical amplifiers (SOAs) amplify signals in the optical communication windows: 0.85, 1.3, and 1.55 μm [3]. An SOA is a laser diode with antireflection (AR) coating on its facets. Gain is provided by stimulated emission in the current-driven population inversion region. About 30 dB internal gain with 6 dB coupling loss has been demonstrated within a 5 THz bandwidth [4]. SOA performance is hindered by fiber coupling loss, polarization dependence, gain ripple, high crosstalk, and high noise figures. EDFAs are therefore favoured for 1.55 μm, and SOAs are used for 1.3 μm. Because they are electrically pumped, SOAs have applications not supported by doped-fiber amplifiers including switching, wavelength conversion, and simultaneous transmission, detection, and amplification [5], [6].

I.2.2 Fiber Brillouin Amplifiers

The energy level diagram in Fig. I.1 illustrates light amplification in silica fibers by stimulated Brillouin scattering (SBS). Through an interaction with the SiO_2 molecules in optical fiber, energy is transferred from pump photons to acoustical phonons and signal (Stokes) photons. In fused silica the signal is downshifted from the pump by 13 GHz, and the pump bandwidth is 23 MHz [7], [8]. These values are determined by the characteristic energy distribution of the acoustical phonons in the glass host. Thus, light input to the optical fiber at the lower pump wavelength amplifies light at the higer signal wavelength. Since SBS requires momentum conservation, it occurs only with backwards pumping. Stokes photons input to the fthat are guided in the fiber are then amplified by SBS. Although fiber Brillouin amplifiers (FBAs) have 20-40 dB small-signal amplification with less

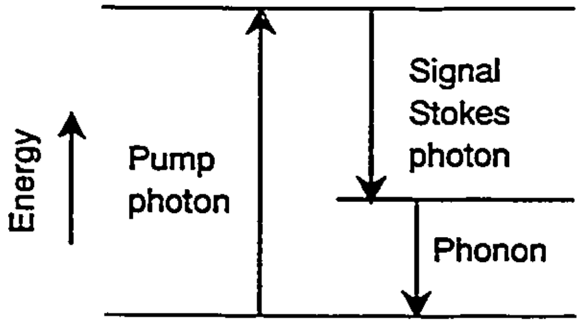

Fig. I.1 Energy level diagram of stimulated Brillouin and Raman scattering.

than 10 mW pumping power, they have the major drawback of a narrow bandwidth (< 100 MHz) which limits the data rate to less than 250 Mb/s. Also, pump laser frequency stabilization to within 10 MHz is required to prevent gain variations. Other drawbacks are the long fiber lengths required (>10 km) and the large excess noise factor caused by the large population of acoustic phonons at room temperature [9]. One advantage of the narrow bandwidth is that a narrow, tunable pump can be used to selectively amplify and demodulate dense wavelength division multiplexed (WDM) channels. FBAs can also selectively amplify a carrier while leaving its modulation side bands unamplified, thereby improving receiver sensitivity. For example, when a 90 Mb/s signal was transmitted over 30 km of fiber only 2.9 mW of pump power improved the receiver sensitivity by 16 dB [9]. One advantage of FBAs is their high output saturation power which can reach about half the input pump power [9]. In conclusion, FBAs have gain greater than 30 dB with low pump power and more than 1 km of fiber, but their narrow bandwidth limits the data rate to less than 250 Mb/s, and the narrow pump linewidth places strict requirements on the pump laser.

I.2.3 Fiber Raman Amplifiers

Stimulated Raman scattering (SRS) also amplifies Stokes photons in optical fibers [10]. The process is similar to that of Brillouin scattering and can be described with a similar energy level diagram as in Fig. I.1. In this case the light interacts with optical phonons of the material which have an energy determined by the vibrational resonance of the glass molecules. In silica fibers the Raman shift is 13.2 THz with a 6 THz bandwidth. Thus the energy shift is larger and broader than that of SBS. Unlike Brillouin amplifiers, fiber Raman amplifiers (FRAs) are self-phase matched and can be either forward or backward pumped. Since, the Raman gain is about 500 times smaller than the Brillouin gain, a Raman amplifier must suppress the pump depleting SBS. SBS can be suppressed by using short pump pulses (<10 ns) or using a multimode pump with a linewidth much larger than the Brillouin linewidth. The major drawback of FRAs is the low gain and associated high pump power and long fiber length. One advantage of FRAs is their broad bandwidth which is useful for simultaneously amplifying WDM signals.

I.2.4 Fiber Parametric Amplifiers Using Four Wave Mixing

Parametric amplification in a fiber occurs when two pump photons are absorbed and, through an interaction with the fiber nonlinear polarization, a signal photon and idler photon are emitted. In comparison with SBS and SRS, parametric frequency conversion is advantageous in that both up and down conversion are possible and the range of possible frequency shifts is broader. The disadvantage is that it requires phase matching to conserve momentum. Phase matching can be achieved by using the different modes of a multimode fiber, by utilizing the birefringence in a polarization maintaining fiber, or by operating close to the zero dispersion wavelength (1.3 μm) [11], [9]. In silica fibers the gain coefficient is about 250 times smaller than that of SBS. Therefore, like fiber Raman amplifiers, parametric amplifiers must also be designed to suppress SBS. Typically, parametric gain typically dominates for short fibers and Raman gain dominates for longer fibers because phase matching is difficult to maintain over long distances due to variations in the fiber core diameter. The total gain is thus limited by the interaction length. Amplifier bandwidths are on the order of 100 GHz and the frequency shift can be as large as 100 THz [9]. In one experiment, 70 W/500 kHz pulses from a Q-switched Nd:YAG pump laser at 1319 nm amplified 1338 nm pulses by 46 dB [12]. Because they require high pump power and phase matching, these amplifiers are impractical for optical communications except for special applications such as spectral inversion for dispersion compensation [13].

I.2.5 Rare-Earth-Doped Fiber Amplifiers

In a rare-earth-doped fiber amplifier light from a pump laser is coupled with light from longer wavelength signals into the doped fiber. The pump excites the rare-earth ions within the fiber core to create a population inversion, from which amplification at the signal wavelength occurs by stimulated emission. Within the 1550 nm telecommunications window, erbium-doped-fiber amplifiers (EDFAs) have demonstrated 51 dB gain and 3 dB noise figure within a 4 THz bandwidth (30 nm) [14]. A typical EDFA is shown in Fig. I.2. The 980 or 1480 nm pump laser is coupled with 1550 nm signal light to the doped fiber by a wavelength selective coupler. The fiber modal confinement

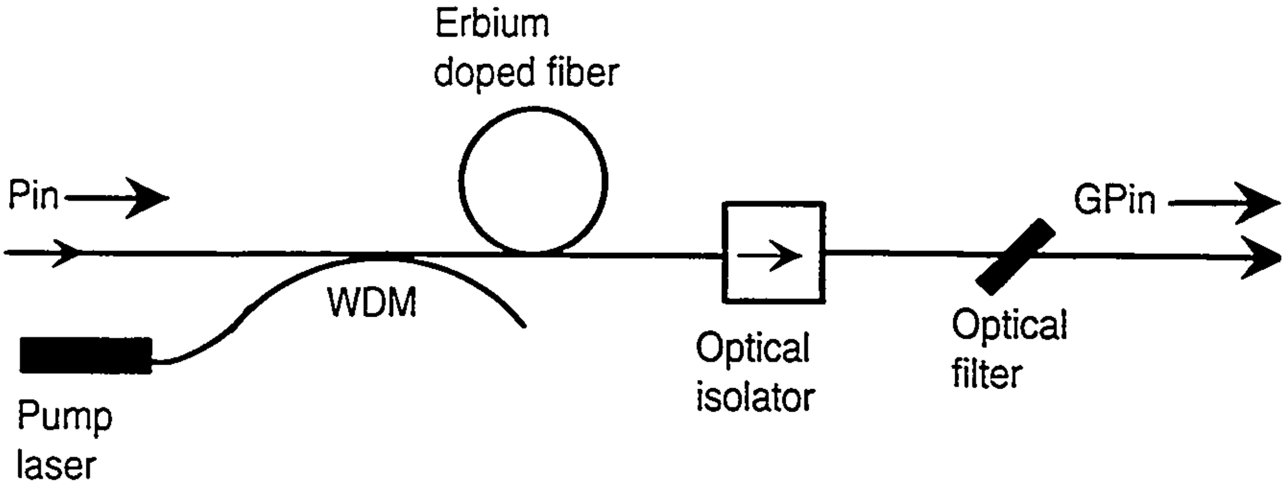

Fig. I.2. Erbium-doped fiber amplifier. WDM is a fiber wavelength division multiplexer.

maintains high pump and signal intensities over long interaction lengths, thus enabling pump to signal differential conversion efficiencies greater than 50% [15]. Efficient amplification is obtained with laser diode pumping since a few milliwatts of pump power gives 30 dB small-signal gain. The saturation output power, limited by the pump power, can be greater than 500 mW [16]. The large gain per pump power that can be achieved with a few meters of fiber is orders of magnitude greater than that given by nonlinear fiber amplifiers. EDFAs can also amplify solitons with negligible pulse distortion [17].

Table I.1 compares the SOA and EDFA. From Table I.1, the EDFA has lower noise, higher gain, polarization independent operation and lower distortion and cross-talk than the SOA. The remarkable performance of erbium-doped fiber amplifiers has stimulated the search for comparable fiber amplifiers for the 1.3 μm window. Two candidates have emerged, neodymium-doped [18] and praseodymium-doped [19] fluoride glass fiber amplifiers. Fluoride glass is chosen for these amplifiers because of its lower phonon energy (see Section II.2). The Pr^{3+}-doped amplifiers have shown the most promise with over 30 dB gain and over 10 dBm saturation output power demonstrated with approximately 1 W of pump power at 1.017 μm [19].

I.2.6 Rare-Earth-Doped Integrated Optical Waveguide Amplifiers and Lasers

The success of rare-earth-doped fiber devices has motivated research in the fabrication of rare-earth-doped integrated optical waveguides [20], [21]. This could be an attractive method to integrate

	EDFA	SOA
Fiber to fiber gain	>40 dB	< 25 dB
Coupling loss	<0.2 dB/side	3-5 dB/side
Polarization sensitivity	insensitive	< 1 dB (best case)
Saturated output power	>20 dBm	<10 dBm
Optical bandwidth	≈ 30 nm Centered on 1530-1550 nm	50-200 nm In both 1310 & 1550 nm windows
Gain modulation	< 10 kHz	> 1 GHz
Noise figure	3-4 dB	5 dB plus coupling loss
Localisation	Discrete and continuous	Discrete
Crosstalk	< -40 dB @ 10^5 Hz	NDFWM Limits channel spacing > 10 GHz
Gain ripple with wavelength	None	-1 dB, 1 nm period
Device lifetime	10^5 Hrs @ 1.48 µm/ 0.98 µm	> 10
Temperature range	± 10°C	±0.5 °C
OTHER	Better linearity Remote optical pumping	Integratable High pump efficiency Versatile: switching, modulation, transmission, detection, filtering add and drop

Table I.1. Comparison of EDFA and SOA.

active components such as lasers, amplifiers, and variable attenuators with other active and passive components on a single substrate. Er^{3+}-doped and Nd^{3+}-doped waveguides and amplifiers have been reported. Fabrication methods include flame-hydrolysis deposition of glass on a silicon substrate followed by solution doping of rare-earth ions and reactive ion etching [22], Er^{3+} diffusion into lithium niobate substrates [23], doping lithium niobate crystals during growth with Nd^{3+} [24], RF-sputter deposition of Er^{3+}-doped soda lime glass films on oxidized silicon substrates [25], and ion-exchange in Er^{3+}-doped glass [26].

In these integrated devices, a very high dopant density compared to that in rare-earth-doped fibers is required because of the relatively short propagation distances. Clustering and upconversion limit the maximum dopant density, which in turn limit the gain per unit length. To date, 3.3 dB/cm is the highest reported gain per unit length in an Er^{3+}-doped waveguide amplifier, obtained with 280 mW pumping at 980 nm [25]. This field is still in its infancy with new materials and fabrication processes being continuously investigated, so significant progress is expected.

I.3 System Applications of Optical Amplifiers

In an optical communications network, optical amplifiers can be used as power amplifiers directly after the signal laser, as in-line amplifiers to replace electronic repeaters, and as preamplifiers directly before the optical receiver. The principal application is in replacing electronic repeaters. This is especially relevant to Gbit/s links where electronic repeaters are more complex and difficult to implement, whereas optical amplifiers are bit-rate transparent. In a joint venture between AT&T and KDD of Japan, a trans-Pacific high-capacity optical communications cable is now being installed with EDFA repeaters every 30-50 km [27]. As preamplifiers, EDFAs can improve optical receiver sensitivity by more than 18 dB [28]. In addition to point-to-point communications, EDFAs are useful in cable TV (CATV) broadcast networks to compensate for the splitting loss, and to amplify the broad range of signals in wavelength division multiplexed networks. One example of this is a demonstration by BTRL of a 39 million-user CATV fed by 12 DFB lasers with two stages of power amplification [29]. At the research level, EDFAs have considerably increased soliton transmission distances to over 12,000 km [30].

I.4 Fiber Lasers

Various fiber lasers that employ a rare-earth-doped fiber amplifier as the gain element in linear or ring cavities have been demonstrated. Lasers are used for applications with stringent light source requirements such as narrow linewidth, wavelength tunability, high power, good spatial beam properties, or short pulse operation. Laser applications include optical communications, optical data storage, spectroscopy, remote sensing, material characterization and processing, medicine, gyroscopes, light detection and ranging (LIDAR), and entertainment [31].

Semiconductor lasers are frequently chosen because of their high efficiency, reliability, low cost, and compact size. However, they presently can not be used effectively in applications where wide tunability, high power, or good spatial beam properties are required. There has recently been strong interest in diode-pumped solid state lasers. These sources deliver high optical power in nearly diffraction limited beams, but they are complex in design and manufacturing. Additional fiber compatible devices are needed to supplement the hybrid semiconductor diode/optical fiber technology currently in use.

Diode-pumped fiber lasers have emerged as an alternative to solid-state and semiconductor lasers. Since the first rare-earth-doped fiber laser was built over 20 years ago [32], many experimental and theoretical results on silica- and fluoride-doped fiber amplifiers and lasers with various rare earth dopants have been reported. Lasing wavelengths range from 0.55 to 2.9 μm based on erbium, neodymium, ytterbium, holmium, thulium, praseodymium, and samarium [2]. Fiber lasers have many potential applications because of their high efficiency, compactness, tunability, high power, fiber compatibility and good spatial beam quality. Because of the high energy-transfer-efficiency in single-mode fibers, it is possible to a obtain very efficient lasing with diode pumping, even on small quantum efficiency transitions which would not normally be considered for lasing.

Fiber lasers offer several advantages over bulk lasers such as their high gain from low pump power. High gain yields low lasing thresholds and high slope efficiencies, allowing the insertion of intracavity elements with large losses. For example, filters can be placed within the cavity to produce very narrow linewidth lasers [33]. The very high gain available from short lengths of fiber allows one to employ high transmission output couplers and reduce the cavity lifetime for Q-switched operation. Q-switching also works particularly well due to the long upper state lifetimes of the common rare-earth dopants in glass [34]. The single-mode nature of the fiber together with a distributed heat dissipation offer excellent mode stability as well as thermal and mechanical stability. These features can be used in seeding oscillators for high-power laser systems. The broadened linewidths of rare earth ions in glass also enable wide tuning ranges [35] and short pulse mode-locking [36].

I.5 Thesis Outline

Chapter II presents an analytical model for two-, three-, and four-level system rare-earth-doped fiber amplifiers and lasers. This is the first ion-independent model for doped fiber devices. Fiber amplifier gain is expressed in terms of attenuation coefficients, intrinsic saturation powers, and cross saturation powers at the pump and signal wavelengths. These parameters can be directly determined from one- and two-beam fiber transmission measurements. Formulas are given for the slopes and thresholds of ring and linear fiber lasers. Because of the finite pump level lifetime, three- and four-level models predict a flattening of the fiber laser slope at higher pumping powers when the fiber is shorter than the optimum length. Approximate solutions are also given for fiber amplifiers with excited state absorption at either the pump or signal wavelengths. A novel technique, requiring only one tunable light source, is proposed for finding the best pump wavelength when pump ESA is present. Experimental measurements of erbium- and thulium-doped fiber lasers and EDFAs show good agreement with the theory.

EDFA noise is discussed in Chapter III. New expressions for the amplifier signal-to-noise ratio are derived leading to an analytical expression for the optimum fiber length. These results are compared to experimental results.

EDFA transient response is modelled in Chapter IV and the model is applied to a novel application, remote all-optical EDFA switching. Experiment and theory show that a strong pulse within the amplifier bandwidth can significantly compress the amplifer gain orders of magnitude faster than previously thought. In the experiments, a mode-locked erbium doped fiber laser is remotely switched by pulses from a Q-switched erbium-doped fiber laser at distances up to 50 km away. Computer simulations show how the signal wavelength and power, pulse wavelength and power, pump power, and fiber length affect the gain compression.

It is experimentally and theoretically demonstrated in Chapter V that transmission of the high energy 1550 nm pulses required for remote EDFA switching is limited by spontaneous Raman scattering in the single-mode fiber. It is shown for the first time that for a given distance and pulse duration, there is an optimum input power that maximizes the transmitted energy. This is important for other applications requiring the transmission of high energy pulses over long fibers.

In Chapter VI new bidirectional amplifiers and frequency dependent optical isolators are proposed and demonstrated for bidirectional networks and fault detection in amplified links. Polarization separated bidirectional networks and related devices are proposed in Chapter VII. The thesis concludes in Chapter VIII with a summary of results to date and suggestions for future work.

Chapter II

Steady-State Modelling of Rare-Earth-Doped Fiber Amplifiers and Lasers

II.1. Introduction

Ongoing development of fiber lasers and amplifiers requires accurate and simple theoretical modelling. The theory of amplification and lasing in fibers differs from traditional laser models in two important aspects. First, the guiding property of single-mode fibers simplifies the analysis since transverse beam and ion profiles can be assumed to be constant along the fiber. Second, the active medium is confined to the central part of the beam profile so that the overlap of the optical modes with the dopant can be assumed to be power independent.

Several numerical models and analytical solutions exist that are based on different simplifying assumptions. Analytical models give solutions for the small signal gain of three- and four-level fiber lasers [37], the threshold of a linear three-level fiber laser with no cavity loss [38], and the slope of a linear two-level fiber laser with no loss and a 100% reflecting rear mirror [39]. The slope, threshold, and lasing wavelength of a linear two-level laser with no cavity loss can also be found graphically [40]. An analytical model also exists for Pr^{3+}-doped fiber amplifiers [41]. However, these approaches require knowledge of fiber parameters that are difficult to measure such as optical mode distributions, dopant ion concentration and distribution within the fiber, emission and absorption cross sections, and decay times.

Preferred models are those that give an analytical solution expressed in terms of easily measured parameters such as attenuation coefficients and saturation powers. Recently, analytical expressions were derived, using a two-level model, to predict EDFA gain from four parameters [42]. These are the fiber attenuation coefficients α_p and α_s and saturation powers P_p^{IS} and P_s^{IS} at the pump and signal wavelengths [42]. The advantage of this method is that these parameters can be easily found by fitting theoretical curves to nonlinear transmission measurements. This model was later expanded to derive expressions for the slope and threshold of ring Er^{3+}-doped fiber lasers (EDFLs) [43]. Experimental results for EDFAs and EDFLs agree with the model [42], [43], since Er^{3+} can be modeled with a two-level system.

However, the model cannot be applied directly to the more complex three- and four-level systems. Analytical expressions are derived in this chapter for the gain of three- and four-level fiber amplifiers and lasers [44]. It is shown that the two-level model is a special case of a three-level system pumped directly to the metastable level (upper lasing level). In this model the absorbed pump power and gain of the amplifier as well as the threshold and slope of the laser are expressed in terms of experimentally determinable attenuation coefficients and intrinsic and cross saturation powers. Two cross saturation power coefficients are introduced, describing the saturating effect of pump light on signal light transmission and vice versa. Pumping a four-level ion directly to the metastable level, as for Pr^{3+}, is also addressed. The threshold, slope efficiency, minimum length, and optimum length of linear and ring fiber lasers are derived. These expressions are differentiated to optimize laser parameters such as the fiber length and output coupler transmission. The resultant amplifier and laser models are the same for all three ionic systems, with system dependent definitions of the saturation powers. Therefore, the model outlines a method, applicable to all systems, for measuring the required fiber parameters and using the parameters to design and optimize amplifiers and lasers.

The theory uses some simplifying assumptions. First, although spontaneous decay is accounted for, amplified spontaneous emission (ASE) is neglected. This is valid for fiber lasers above threshold and for fiber amplifiers when the input signal power is significantly above the equivalent ASE noise input power as discussed in Ref. [42]. ASE noise modelling is discussed in the next chapter. Second, it is assumed that there is no excited state absorption (ESA) at any of the pump or signal wavelengths. (An approximate amplifier solution that includes ESA at either the pump or signal wavelength is given in Section 3.5). Third, it is assumed that field and dopant distributions are independent of fiber position and power levels. This is satisfied for typical doped fibers that have a dopant radius less than the core radius. Background loss is also neglected. This is usually valid for three-level systems where the absorption by the rare earth ions is typically much greater than other losses. However, background loss can be significant for distributed amplifiers and at the signal wavelength in four-level systems. The effect of background loss on transmission measurements is discussed in Section 3.6.

This chapter is organized as follows. Section 2 provides a brief summary of the spectroscopic properties of the common rare earth ion dopants. Section 3 gives the fiber amplifier theory for two-, three-, and four-level ions, beginning with the rate equations in Section 3.1. A solution to the rate equations is then given in terms of transmission parameters in Section 3.2. Section 3.3 has a discussion of the physical meaning of the transmission parameters and Section 3.4 lists some expressions used to describe amplifier and laser performance. Corrections to the model for cases where ESA or distributed loss are significant are given in Sections 3.5 and 3.6, respectively. The fiber laser theory is derived in Section 4 using the formulas for fiber gain given in Section 3. The laser solution procedure is outlined in Section 4.1 and the solutions are discussed in Section 4.2. In Section 5 the theory is compared to previously published results. Experimental verification is presented in Section 6 and conclusions are given in Section 7.

II.2. Spectroscopic Properties of Rare-Earth Ions

This section reviews the spectral properties of Er^{3+}-, Tm^{3+}-, and Yb^{3+}-doped silica glass, and Nd^{3+}- and Pr^{3+}-doped fluoride glass. Devices based on other dopants are reviewed in Ref. [2]. Figures II.1a and II.1b show simplified models of the energy levels of three- and four-level ions and their decay times. The levels are numbered in a particular manner that allows one set of rate equations to be used for both systems. Figure II.1c shows the special case of Pr^{3+}, which contains two intermediate levels between the upper and lower lasing levels. Table II.1 lists the absorption and emission cross sections and decay times for the five ions. Depending on the codopants and dopant concentration, cross sections and decay times can vary substantially from host to host.

Rare-earth-ion optical transitions occur within an inner orbital. Since the electrons are shielded from external perturbations by the outer orbital, the optical transitions are mainly host independent. The host does affect the fine structure of the absorption and emission spectra, the non-radiative decay rates, and the relative strengths of radiative and non-radiative transitions. Two important host properties are the surrounding field it imposes on the rare-earth ion and its phonon energy which affects the non-radiative decay rates. Because SiO_2 molecules have a lower mass than fluoride glass molecules, silica glass has a larger phonon energy (1150 cm^{-1} cf. 590 cm^{-1}). Consequently, non-radiative decay of rare-earth ions in silica is faster since it requires fewer phonons. Many rare-earth optical transitions are therefore observed in doped fluoride glasses, but not in silica glasses, because the non-radiative phonon assisted transitions are slowed to the point that the competing optical transitions dominate. This is the reason why fluoride glass is better for Pr^{3+}-doped fiber amplifiers. The reduced non-radiative transition rate in low-phonon energy doped glass results in a high radiative

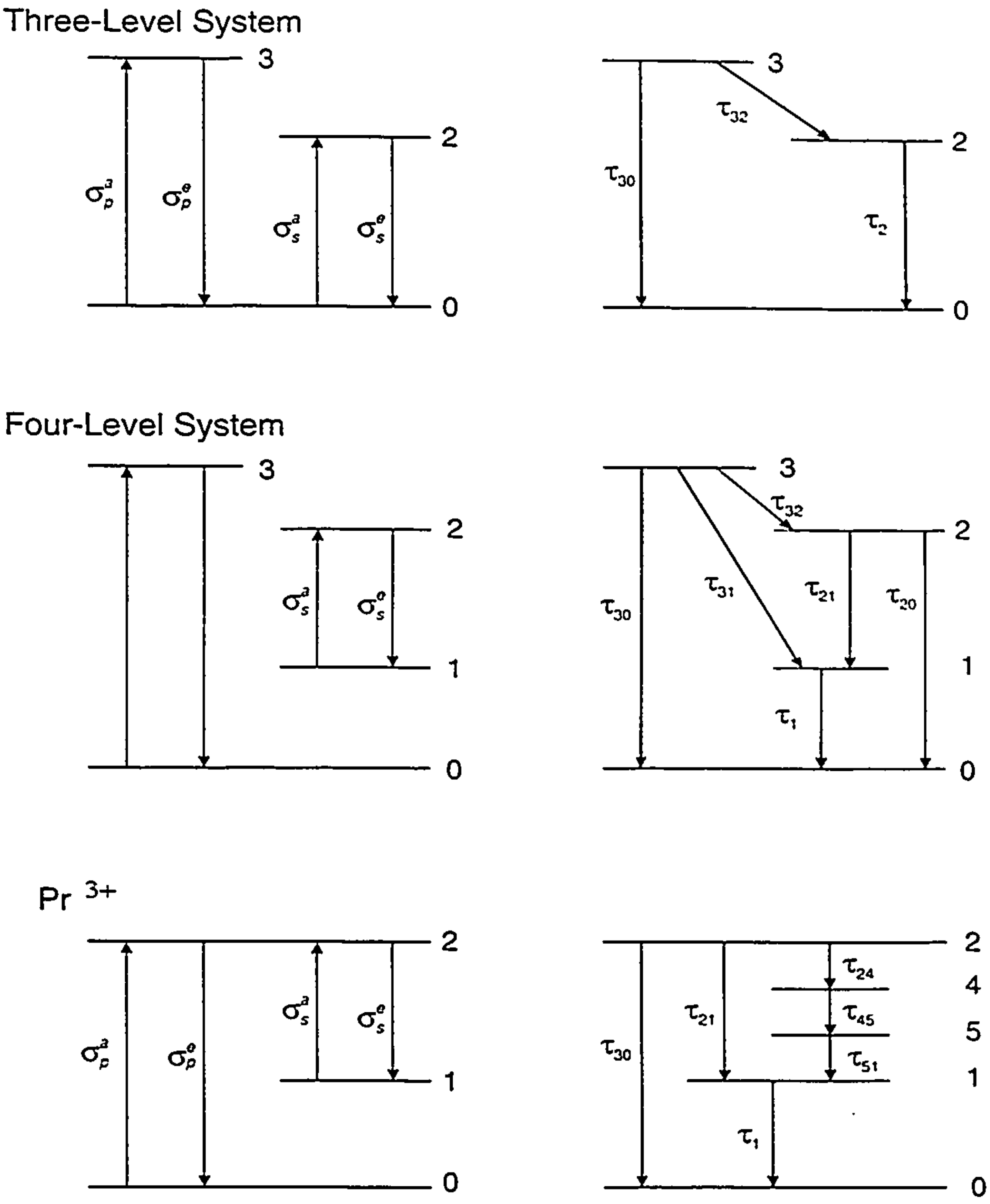

Fig. II.1. Energy level diagrams for (a) three-level systems, (b) four-level systems, and (c) Pr^{3+}.

quantum efficiency. However, it also slows the decay from the pump level to the metastable level, thus limiting the pumping efficiency. Therefore, rare-earth-ion optical transistions in fluoride glass have a higher quantum efficiency and lower pumping efficiency than the corresponding transitions in silica glass. Silica fibers have the added advantage that their fabrication is a well established technology. Efficient lasers with both types of fibers have been demonstrated [2].

Erbium is modeled with a three-level system (Fig. II.1a). It can amplify signals between 1520 and 1565 nm. It is pumped at 515, 532, 650, 807, 980, or 1480 nm with the latter two wavelengths being favoured since they are free of ESA. At 1480 nm, pumping is directly to the upper sub-levels of the metastable manifold. Progress in EDFAs has successfully stimulated research into high-power laser diodes at 980 and 1480 nm. Continuous wave powers as high as 180 mW at 1.48 μm with a GaInAsP diode [45] and 240 mW at 980 nm from a InGaAs/AlGaAs single quantum well laser have been demonstrated [46].

Neodymium is modeled with a four-level system (Fig. II.1b). It is pumped at 800 nm to amplify light at 1060 and 1340 nm. Unfortunately, signal ESA prevents efficient amplification at 1310 nm. Also, it has a stronger competing emission at 1060 nm. At 1320 nm, gain of about 10 dB has been achieved with Nd^{3+}-doped fluoride fiber amplifiers [18].

Praseodymium-doped fluorozirconate fiber can amplify signals between 1280 and 1360 nm. It is pumped at 1007 nm directly into upper sub-levels of the broad metastable manifold. Pr^{3+} is treated as a special case of a four-level system. Its behaviour is also complicated by the presence of two intermediate levels between the metastable level and terminal level, as shown in Fig. II.1c.

Thulium is modeled with a three-level system at longer signal wavelengths and with a four-level system at shorter signal wavelengths. This is because its terminal laser level is only slightly populated at room temperature. It is pumped at 780 nm and amplifies signals from 1.7 to 2.1 μm.

Ytterbium is often used as an activator for energy transfer to another ion, because of its broad absorption around 950 nm. All optical transitions are between two Stark split multiplets. In silica glass it has two absorption peaks centered at 910 and 974 nm and two emission peaks centered at 974 and 1036 nm with potential lasing from 980 to 1160 nm. The short wavelength transition is three level in nature, being to the bottom of the ground state multiplet, and the long wavelength transition is quasi four-level in nature, being to the top of the ground state multiplet. Thus, for shorter laser wavelengths Yb^{3+} is modeled with a three-level system pumped directly to the metastable level, as

Ion	λ (nm)	σ (pm^2)	τ
Er^{3+}	980	$\sigma_p^a = 0.2$	$\tau_{32} = 10\ \mu s$
	1480	$\sigma_p^a = 0.2$ $\sigma_p^e = 0.02$	$\tau_{32} < 1$ ns
	1535	$\sigma_s^e = 0.4\text{-}0.8$ $\sigma_s^a = 0.4\text{-}0.8$	$\tau_2 = 10$ ms
Nd^{3+}	780	$\sigma_p^a = 1\text{-}2$	$\tau_{32} < 100$ ns
	1060	$\sigma_s^e = 1\text{-}4$	$\tau_2 = 0.2\text{-}0.8$ ms $\tau_{10} < 10$ ns
	1320	$\sigma_s^e = 0.3\text{-}1.4$	$\tau_2 = 0.2\text{-}0.8$ ms $\tau_{10} < 10$ ns
Pr^{3+}	1007	$\sigma_p^e = 0.02$ $\sigma_p^a = 0.04$	$\tau_{32} < 1$ ns
	1320	$\sigma_s^e = 0.06$ $\sigma_s^a = 0.07$	$\tau_2 = 10$ ms $\tau_{10} = 100$ ns
Tm^{3+}	790	$\sigma_p^a = 0.8$	$\tau_1 = 20\ \mu s$
	1920	$\sigma_s^e = 0.7$ $\sigma_s^a = 0.03$	$\tau_2 = 250\ \mu s$
Yb^{3+}	910	$\sigma_p^a = 0.6$	$\tau_{32} < 1$ ns
	974	$\sigma^a = 1.5$ $\sigma^e = 3.5$	$\tau_{32} < 1$ ns $\tau_2 = 770\ \mu s$ $\tau_{10} < 1$ ns
	1036	$\sigma_s^e = 0.6$	$\tau_2 = 770\ \mu s$

Table II.1. Spectroscopic properties of Er^{3+} [47], Tm^{3+} [48], and Yb^{3+} [49] in silica glass and Nd^{3+} [50] and Pr^{3+} in fluoride glass [41].

for 1480 nm pumping of Er^{3+}. For longer laser wavelengths, it is modeled with a four-level system pumped directly to the metastable level, as for Pr^{3+}.

II.3. Fiber Amplifier Theory

II.3.1 Rate Equations

The rate equations are based on the energy level diagrams in Fig. II.1. The fiber is doped with $N_t(r,\phi,z,t)$ active ions per unit volume with $N_i(r,\phi,z,t)$ ions per unit volume in the *i*th level at the given position (r,ϕ,z) and time (t). Rate equations are written for K_p pump beams and K_s signal beams. Unlike the two level theory [42], it is necessary to differentiate between pump and signal beams (denoted by *s* and *p* subscripts, respectively) since they interact with different energy levels. A signal beam is defined as one that interacts with the metastable level and the terminal lasing level, and a pump beam is defined as one that interacts with the ground state and the pump level. For direct pumping to the metastable level, such as for 1480 nm pumping of Er^{3+}, the pump is theoretically treated as an additional signal beam. Direct pumping to the metastable level for a four-level ion, such as for 1007 nm pumping of Pr^{3+}, is a special case treated differently. For clarity, powers are expressed in photons per second and symbols indicating the time and positional dependencies of intensities and ion populations are not shown in the rate equations.

Amplification in rare-earth-doped fibers is governed by absorption emission processes described by the rate equations for two-, three-, and four-level systems [14]:

$$N_t = N_0 + N_1 + N_2 + N_3 \tag{1}$$

$$\frac{\partial N_3}{\partial t} = \sum_{k=1}^{K_p} I_{p,k} \left(N_0 \sigma^a_{p,k} - N_3 \sigma^e_{p,k} \right) - \frac{N_3}{\tau_3} \tag{2}$$

$$\frac{\partial N_2}{\partial t} = \sum_{k=1}^{K_s} I_{s,k} \left(N_0 \sigma^a_{s,k} + N_1 \sigma^{a*}_{s,k} - N_2 \sigma^e_{s,k} \right) - \frac{N_2}{\tau_2} + \frac{N_3}{\tau_{32}} \tag{3}$$

where $\sigma_{s,k}^e$, $\sigma_{p,k}^e$ ($\sigma_{s,k}^a$, $\sigma_{p,k}^a$) denote the emission (absorption) cross section of the signal and the pump at the wavelength of the *k*th beam. $I_{s,k}$ ($I_{p,k}$) denotes the intensity of the *k*th signal (pump) beam, and τ_{ij} denotes the combined radiative and non-radiative decay times from the *i*th level to the *j*th level.

The net decay rates from the pump and metastable levels are denoted by τ_3 and τ_2, respectively. In these equations terms proportional to $\sigma_{i,k}^{e}$ describe stimulated emission, terms proportional to $\sigma_{i,k}^{a}$ describe stimulated absorption, and terms with $1/\tau_i$ describe spontaneous emission. Four-level systems also have the following additional equation:

$$\frac{\partial N_1}{\partial t} = -\sum_{k=1}^{K_s} I_{s,k}\left(N_1\sigma_{s,k}^{a*} - N_2\sigma_{s,k}^{e}\right) - \frac{N_1}{\tau_1} + \frac{N_2}{\tau_{21}} + \frac{N_3}{\tau_{31}} \qquad (4)$$

where $\sigma_{s,k}^{a*}$ denotes the cross section for signal absorption from the lower lasing level in a four-level system (see Fig. II.1b). The rate equations (1)-(4) can therefore be used for two-, three-, or four-level systems with the following settings:

Two-level	Three-level	Four-level
$N_1 = N_3 = 0$	$N_1 = 0$	$\sigma_{s,k}^{a} = 0$
$\sigma_{s,k}^{a*} = 0$	$\sigma_{s,k}^{a*} = 0$	

The evolution of the power in each pump and signal beam is given by

$$\frac{\partial P_{p,k}}{\partial z} = u_{p,k} \int\left(N_3\sigma_{p,k}^{e} - N_0\sigma_{p,k}^{a}\right) I_{p,k}\,dA \qquad (5)$$

$$\frac{\partial P_{s,k}}{\partial z} = u_{s,k} \int\left(N_2\sigma_{s,k}^{e} - N_1\sigma_{s,k}^{a*} - N_0\sigma_{s,k}^{a}\right) I_{s,k}\,dA \qquad (6)$$

where $u_{i,k}$ is +1 for propagation in the positive z direction and -1 for propagation in the negative z direction. Integration is over the transverse plane extending to infinity and $dA = r dr d\phi$ in the cylindrical coordinate system. Spontaneous emission is included in the theory by the N_2/τ_2 term in (3), but amplified spontaneous emission (ASE) is neglected.

II.3.2 Solution of Rate Equations

For steady state conditions, the time differentials in (2)-(4) can be set to zero. Equations (1)-(4) are then simplified by performing the transverse integration once only, thus assuming that transverse dependences are independent of longitudinal position. This simplifies the rate equations from being given in terms of difficult to measure constants such as the ionic cross sections, dopant concentration, and dopant and fiber geometry to being given in terms of directly measurable values like attenuation coefficients and saturation powers constants. This simplification is shown using, as an example, a two- or three-level system with only one signal beam present. For steady state conditions the rate equation, (3), reduces to

$$\frac{N_2(r,\phi,z)}{\tau_2} = I_s(r,\phi,z)\left[N_0(r,\phi,z)\sigma_s^a - N_2(r,\phi,z)\sigma_s^e\right] \tag{7}$$

Integrating this equation over the transverse plane and dividing by the effective dopant area A_{eff} gives

$$\frac{\bar{N}_2(z)}{\tau_2} = \frac{P_s(z)}{A_{eff}}\left(\bar{N}_0(z)\Gamma_{s,0}\sigma_s^a - \bar{N}_2(z)\Gamma_{s,2}\sigma_s^e\right) \tag{8}$$

where $\bar{N}_i$ is the ion concentration in the *i*th energy level averaged over the fiber cross section and the effective area of the dopant ions is given by

$$A_{eff} = \int\frac{N_t(r,\phi,z)dA}{N_t(0)} \tag{9}$$

For a uniformly-doped fiber with dopant radius b, $A_{eff} = \pi b^2$. The overlap integral or confinement factor for the *i*th level is given by [14]

$$\Gamma_{s,i}(P_s,z) = \frac{A_{eff}\int I_k(r,\phi,z)N_i(r,\phi,z)dA}{P_s(z)\int N_i(r,\phi,z)dA} \tag{10}$$

Integrating the equation for power evolution (6) over the transverse plane yields:

$$\frac{\partial P_s(z)}{\partial z} = u_s P_s(z)\left(\bar{N}_2\Gamma_{2,s}\sigma_s^e - \bar{N}_0\Gamma_{0,s}\sigma_s^a\right) \tag{11}$$

The transverse integration results in the transverse dependence being contained in the power dependent parameters $\Gamma_{s,i}$ and A_{eff}. The resulting equations are given in terms of optical powers which depend on longitudinal distance z, only, instead of intensities which also depend on transverse coordinates.

Overlap integrals depend on: (i) the energy level occupied by the ions since the distribution is different for each level, (ii) the power since the ion dopant distribution is power dependent, and (iii) the wavelength since the optical mode profile is wavelength dependent. In principle, the overlap integrals are also functions of z due to variations in doping level along the fiber and mode coupling if more than one mode is supported. For a fundamental mode approximated by a Gaussian profile $I(r)=(2P/\pi w^2)\exp(-2r^2/w^2)$ and a uniformly-doped fiber with dopant radius b, the overlap of the mode with the total ion profile $N_t(r,\phi,z)$ is given by

$$\Gamma_t = 1 - e^{-\frac{2b^2}{w^2}} \tag{12}$$

In the low-power limit the overlap integral with the ions in the ground state is also given by (12) [14]. In the low-power limit all excited-state overlap integrals reduce to

$$\Gamma_{1,2,3,4}(P \rightarrow 0) = \left(\frac{b}{w}\right)^2 \frac{1 - e^{-\frac{4b^2}{w^2}}}{1 - e^{-\frac{2b^2}{w^2}}} \tag{13}$$

A distinction between the confinement factors for the different levels was stated in [14] but the approximate form (13) for the upper levels has not been given previously. This difference is shown in Fig. II.2, which plots $F = (\Gamma_2-\Gamma_t)/\Gamma_t$, the difference in overlap integrals for the excited state population and the total population in the low power limit. Typically, the fiber dopant radius is less than or equal to the core radius ($b/w \leq 0.8$), so the overlap integral for all levels can be well approximated by the expression for Γ_t in Table II.2. For $b/w \leq 0.8$ the integrals also have weak power dependence [14]. It is thus assumed that overlap integrals are power independent and are equal to Γ_t for ions in all the energy levels. Overlap integrals for higher modes were discussed in Ref. [51]. The strong power dependence of the overlap integrals when $b > w$ is the main difficulty in extending this theory to bulk lasers.

The rate equations in terms of optical power (11) are simplified by introducing absorption coefficients and saturation powers. The small-signal absorption coefficient is given by

$$\alpha(\lambda_k) = \Gamma(\lambda_k)\tilde{N}_t\sigma_k^a(\lambda_k) \tag{14}$$

and the saturation power constants are defined in Table II.3 in terms of the material constants given in Table II.2. The pump efficiency η_p specifies what fraction of the total ions excited to the pump level decays to the metastable level, thus becoming potentially useful for stimulated emission. Ions with a high pump efficiency are characterized by having η_p close to unity. For a four-level system, β_{12} is the ratio of the number of ions in level 1 to the number in level 2 when only weak pump light is present (P_s=0). This factor is found by solving (2) for steady state conditions while $I_{s,k} = 0$. β_{ie} is the ratio of the number of ions in the ith excited level to the total number of excited ions, $N_e = N_t - N_0$ when only weak pump light is present (P_s=0). For four-level systems pumped directly to the metastable manifold the values of β_{il} are listed separately. Praseodymium is more complex since it has two intermediate levels, which allow a competing multiphonon transition from the lasing level (see Fig. II.1c on p. 13). Its β_{il} ratios are also listed separately in Table II.2.

The solution to the rate equations is now given in terms of the attenuation coefficients and saturation powers. Substituting the integrated form of (5) into (2) gives an equation for N_3 as a sum of $\partial P_{p,k}/\partial z$ terms. Substituting this expression and the integrated (6) into (3) gives an equation for N_2 as a sum of $\partial P_{p,k}/\partial z$ and $\partial P_{s,k}/\partial z$ terms. These equations are substituted into the integrated forms of (5) and (6) to give the final differential equations for pump and signal beams:

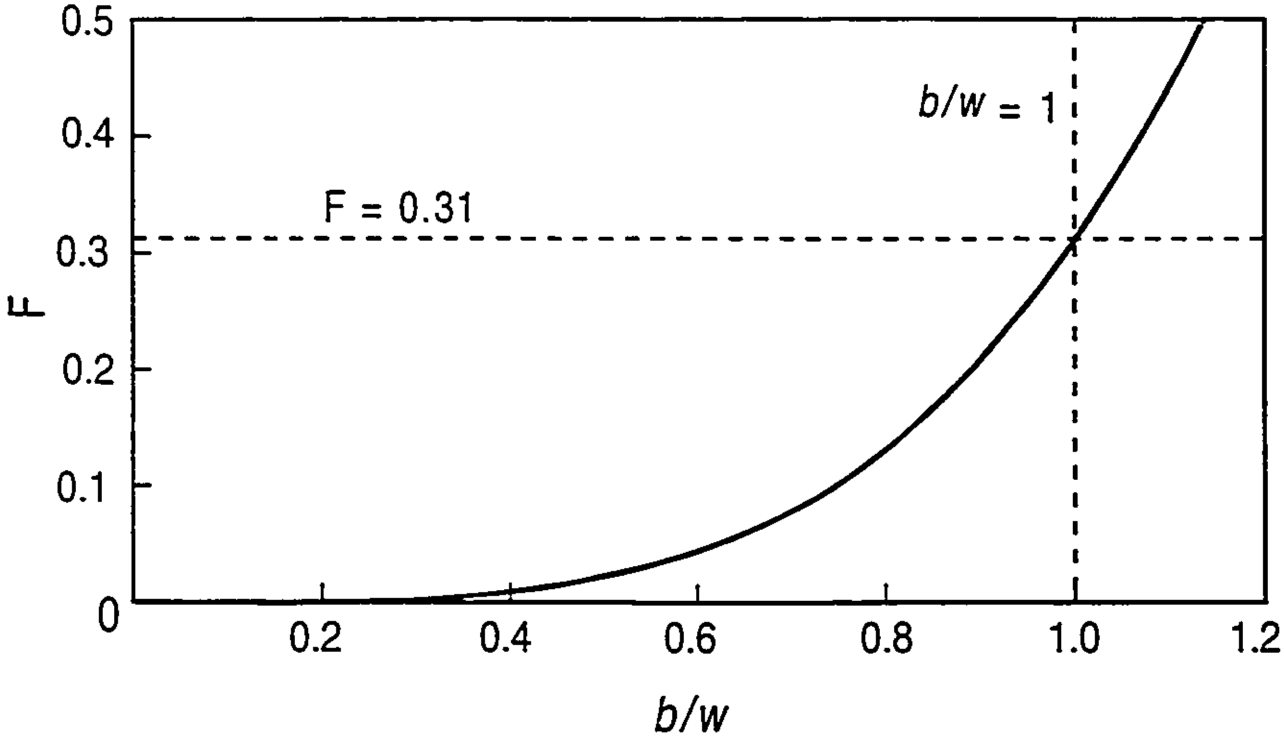

Fig. II.2. Comparison of the overlap integrals for the excited states and for the ground state.

Constant	Symbol	Definition
Overlap integral	Γ_t	$\Gamma_t = 1 - \exp(-2b^2/w^2)$
Effective dopant area	A_{eff}	$A_{eff} = \pi b^2$
Pump efficiency	η_p	$\eta_p = \tau_3/\tau_{32}$
N_1/N_2 (@P_s = 0)	β_{12}	$\beta_{12} = \tau_1/\tau_{21} + \tau_{32}\tau_1/\tau_2\tau_{31}$ (Four-level) $\beta_{12} = \tau_1/\tau_{21}$ (Four-level to level 2) $\beta_{12} = \tau_1/\tau_{21} + \tau_1/\tau_{24}$ (Pr^{3+})
N_1/N_e (@P_s = 0)	β_{1e}	$\beta_{1e} = \beta_{12}$ (Four-level)
N_2/N_e (@P_s = 0)	β_{2e}	$\beta_{2e} = (1 + \tau_{32}/\tau_2)^{-1}$ (Three-level) $\beta_{2e} = (1+\tau_{32}/\tau_2+\tau_1/\tau_{21}+\tau_1\tau_{32}/\tau_2\tau_{31})^{-1}$ (Four-level) $\beta_{2e} = (1 + \tau_1/\tau_{21})^{-1}$ (Four-level to level 2) $\beta_{2e} = (1+\tau_1/\tau_{24}+\tau_1/\tau_{21}+\tau_{45}/\tau_{24}+\tau_{51}/\tau_{24})^{-1}$ (Pr^{3+})
N_3/N_e (@P_s = 0)	β_{3e}	$\beta_{3e} = (\tau_{32}/\tau_2)\beta_{2e}$ (Three- and four-level)
Quantum efficiency	η_q	$\eta_q = \lambda_p/\lambda_s$
Maximum gain	$G_{max}(\lambda_p,\lambda_s)$	$G_{max}(\lambda_p,\lambda_s) = \exp\left[(\alpha_p/\delta - \alpha_s)L\right]$
Saturation power ratio	$\delta(\lambda_p,\lambda_s)$	$\delta(\lambda_p,\lambda_s) = P_s^{CS}(\lambda_s)/P_p^{IS}(\lambda_p)$
Effective mirror reflectivity	R	$R^2 = R_1R_2$
Effective cavity transmission	ε	$\varepsilon = \varepsilon_1\varepsilon_2$
Effective output transmission	T_{eff}	$T_{eff} = \left(1 - \varepsilon_2^2R_2\right) + \left(1 - \varepsilon_1^2R_1\right)\varepsilon_2^2R_2/(\varepsilon R)$ (Linear laser) $= 1 - \kappa\varepsilon$ (Ring laser)

Table II.2. Symbols and their definitions..

$$\frac{\partial P_{p,k}}{\partial z} = u_{p,k}\; P_{p,k} \left\{ \frac{1}{P_p^{IS}(\lambda_k)} \sum_{j=1}^{K_p} -u_{p,j} \frac{\partial P_{p,j}}{\partial z} + \frac{1}{P_p^{CS}(\lambda_k)} \sum_{j=1}^{K_s} -u_{s,j} \frac{\partial P_{s,j}}{\partial z} - \alpha_{p,k} \right\} \tag{15}$$

$$\frac{\partial P_{s,k}}{\partial z} = u_s^{k}\; P_{s,k} \left\{ \frac{1}{P_s^{IS}(\lambda_k)} \sum_{j=1}^{K_s} -u_{s,j} \frac{\partial P_{s,j}}{\partial z} + \frac{1}{P_s^{CS}(\lambda_k)} \sum_{j=1}^{K_p} -u_{s,j} \frac{\partial P_{p,j}}{\partial z} - \alpha_{s,k} \right\} \tag{16}$$

Solving (15) and (16) for the output powers, $P_{i,k}^{out}$ by integrating from $z = 0$ to $z = L$, yields:

$$P_{p,k}^{out} = P_{p,k}^{in} \exp\left\{ -\alpha_{p,k} L + \frac{P_p^{in} - P_p^{out}}{P_p^{IS}(\lambda_k)} + \frac{P_s^{in} - P_s^{out}}{P_p^{CS}(\lambda_k)} \right\} \tag{17}$$

$$P_{s,k}^{out} = P_{s,k}^{in} \exp\left\{ -\alpha_{s,k} L + \frac{P_s^{in} - P_s^{out}}{P_s^{IS}(\lambda_k)} + \frac{P_p^{in} - P_p^{out}}{P_s^{CS}(\lambda_k)} \right\} \tag{18}$$

where P_p^{in} (P_s^{in}) is the total power in all input pump (signal) beams and P_p^{out} (P_s^{out}) is the total power in all output pump (signal) beams. Intrinsic saturation powers P_i^{IS} and the cross saturation powers P_i^{CS} are defined in Table II.3.

This is the main result of the fiber amplifier theory. It yields an equation for the output power of each pump and signal beam, independent of propagation directions. The equations are coupled since the output power of any beam depends on the total absorbed signal and pump powers. The coupled equations can be solved by any standard root-finding technique. An advantage of this formalism is that output pump and signal powers are expressed in terms of directly measurable quantities. Knowledge of cross sections, fiber geometry, and decay times is not required.

P_i^{IS} and α_i can be found from one-beam transmission measurements at the pump (i=p) and signal (i=s) wavelengths, in which the transmission T_i is measured as a function of the input power P_i^{in} for a fiber of length L. The measurements are fit by a non-linear least-squares procedure (such as the Levenberg-Marquardt method) to the following transcendental equation:

Coefficient	Two-level, three-level pumped to level 2	Three-level	Four-level	Four-level pumped to metastable level
$P_p^{IS}(\lambda_l) =$	$\frac{A_{eff}}{\Gamma_p}.\frac{1}{\tau_2}.\frac{1}{\sigma^a_{p\lambda}+\sigma^e_{p\lambda}}$	$\frac{A_{eff}}{\Gamma_p}\frac{\beta_{2e}}{\eta_p\tau_2}\frac{1}{\sigma^a_{p\lambda}+\beta_{3e}\sigma^e_{p\lambda}}$	$\frac{A_{eff}}{\Gamma_p}\frac{\beta_{2e}}{\eta_p\tau_2}\frac{1}{\sigma^a_{p\lambda}+\beta_{3e}\sigma^e_{p\lambda}}$	$\frac{A_{eff}}{\Gamma_p}\frac{\beta_{2e}}{\tau_2}\frac{1}{\sigma^a_{p\lambda}+\beta_{2e}\sigma^e_{p\lambda}}$
$P_p^{CS}(\lambda_l) =$	$\frac{A_{eff}}{\Gamma_p}.\frac{1}{\tau_2}.\frac{1}{\sigma^a_{p\lambda}+\sigma^e_{p\lambda}}$	$\frac{A_{eff}}{\Gamma_p}\frac{1}{\tau_2}\frac{1}{\sigma^a_{p\lambda}}$	$\frac{A_{eff}}{\Gamma_p}\frac{1}{\tau_2}\frac{1}{\sigma^a_{p\lambda}\left(1-\frac{\tau_1}{\tau_{20}}\right)}$	$\frac{A_{eff}}{\Gamma_p}\frac{1}{\tau_2}\frac{1}{\sigma^a_{p\lambda}\left(\frac{1}{\beta_{2e}}-\beta_{12}-\frac{\tau_1}{\tau_{20}}\right)+\sigma^e_{p\lambda}}$
$P_s^{IS}(\lambda_l) =$	$\frac{A_{eff}}{\Gamma_s}\frac{1}{\tau_2}\frac{1}{\sigma^a_{s\lambda}+\sigma^e_{s\lambda}}$	$\frac{A_{eff}}{\Gamma_s}\frac{1}{\tau_2}\frac{1}{\sigma^a_{s\lambda}+\sigma^e_{s\lambda}}$	$\frac{A_{eff}}{\Gamma_s}\frac{1}{\tau_2}\frac{1}{\sigma^e_{s\lambda}+\sigma^{a*}_{s\lambda}\frac{\tau_1}{\tau_{20}}+\sigma^e_{s\lambda}}$	$\frac{A_{eff}}{\Gamma_s}\frac{1}{\tau_2}\frac{1}{\sigma^e_{s\lambda}+\sigma^{a*}_{s\lambda}\frac{\tau_1}{\tau_{20}}}$
$P_s^{CS}(\lambda_l) =$	$\frac{A_{eff}}{\Gamma_s}\frac{1}{\tau_2}\frac{1}{\sigma^a_{s\lambda}+\sigma^e_{s\lambda}}$	$\frac{A_{eff}}{\Gamma_s}\frac{\beta_{2e}}{\eta_p\tau_2}\frac{1}{\sigma^a_{s\lambda}+\beta_{2e}\sigma^e_{s\lambda}}$	$\frac{A_{eff}}{\Gamma_s}\frac{\beta_{2e}}{\eta_p\tau_2}\frac{1}{\beta_{2e}\sigma^e_{s\lambda}-\beta_{12}\sigma^{a*}_{s\lambda}}$	$\frac{A_{eff}}{\Gamma_s}\frac{\beta_{2e}}{\tau_2}\frac{1}{\beta_{2e}\sigma^e_{s\lambda}-\beta_{1e}\sigma^{a*}_{s\lambda}}$

Table II.3. Intrinsic saturation powers.

$$T_i = e^{-\alpha_i L} e^{(1-T_i)\frac{P_i^{in}}{P_i^{IS}}} \qquad (19)$$

with α_i and P_i^{IS} as fit parameters. The cross saturation coefficient P_p^{CS} (P_s^{CS}) is found from a two-beam transmission measurement in which the pump (signal) transmission is measured as a function of the input signal (pump) power. The measurements are fit to (17) with P_p^{CS} as a fitted parameter and to (18) with P_s^{CS} as a fitted parameter, using the P_i^{IS} from the one-beam measurements. Since a four-level ion has no ground state absorption at the signal wavelength (α_s=0), P_s^{IS} is found by measuring the signal transmission as a function of the input signal power with constant pump light present. The results are fit to (18) with P_s^{IS} as a fitted parameter. Also, if the fiber emission and absorption spectra are known, the parameters measured at one wavelength can be scaled to other wavelengths. If an ion has high pumping efficiency (η_p=1) and fast decay from the pump and terminal lasing levels (β_{2e} = 1, β_{3e} = 0, β_{12} = 0, τ_1 = 0) then $P_p^{CS} = P_p^{IS}$ and $P_s^{CS} = P_s^{IS}$, rendering the cross saturation measurements unnecessary. For example, Er^{3+} has η_p = 1 and β_{2e} = 1 for 980 nm pumping. In the transmission measurements the output power is first measured, and then the input power is determined by either tuning the light source out of the absorption band or by using a cut-back technique. Table II.3 and (14) relate rare earth ion cross sections and level lifetimes to absorption coefficients and saturation powers. This introduces a new technique for measuring unknown spectroscopic properties from fiber transmission measurements in cases where some properties are known [48].

II.3.3 Physical Meaning of Saturation Parameters

An inspection of the equations for output powers, (17) and (18), reveals the following: A large α_p, P_p^{IS}, and P_p^{CS} are favoured to maximize the absorbed pump power. The parameter characterizing the transfer of energy from the absorbed pump power to the signal is P_s^{CS}. Gain increases as this parameter decreases. Therefore, as expected, ions are favoured which have a large σ_s^e, η_p, and τ_2. For a two-level system the saturation coefficients all have the same form since all interactions are between the same two energy levels. Saturation coefficients have different forms for three- and four-level systems since different beams interact with different energy levels. However, $P_i^{IS} = P_i^{CS}$ for most ions, because lifetimes of the pump and lower lasing levels are short compared to the metastable level lifetime. All saturation powers have an inverse dependence on τ_2 since saturation occurs at lower powers for slower upper-level decay. For a two-level system, saturation occurs at lower powers for higher σ_i^a and σ_i^e because of the increased absorption and stimulated emission rates.

P_p^{IS} (P_s^{CS}) characterizes how signal (pump) absorption is saturated by pump light. In three- and four-level systems, pump light does not interact with the metastable level. Because of this, P_p^{IS} and P_s^{CS} have τ_2 weighted by η_p, which accounts for the number of pumped ions reaching the metastable level. The β_{2e} term in the numerator of P_p^{IS} and P_s^{CS} accounts for the relative population of the metastable level. In these saturation powers the emission cross sections are also weighted by β_{ie} where $i = 3$ for P_p^{IS} and $i = 2$ for P_s^{CS}. This accounts for the fact that in three- and four-level systems, unlike two-level systems, not all excited ions are available for stimulated emission. For P_s^{CS} in a four-level system the sign of σ_s^{a*} is negative and is weighted by β_{12} (or β_{1e} for systems pumped to the metastable level). When there is strong signal absorption from level 1 to level 2, fewer excited ions return to the ground state. As a result, fewer ions are available to interact with the pump light, thus diminishing the saturating effect of the pump light. Gain is prevented by saturation of the terminal laser level unless $\beta_{12} < \sigma_s^e/\sigma_s^{a*}$.

P_s^{IS} (P_p^{CS}) characterizes how signal (pump) absorption is saturated by signal light. P_s^{IS} is the same for two- and three-level systems since the signal light does not interact with the pump level. For a four-level system, absorption is from the lower lasing level so that σ_s^{a*} is weighted by τ_1/τ_{20}, which accounts for the weak signal absorption due to the (low) population of the lower lasing level. As this factor increases, the population of the lower lasing level increases and P_s^{IS} increases. Since a signal does not interact with the pump level, it indirectly saturates the pump absorption by depleting the ground state. Therefore, σ_p^e is not present in P_p^{CS}, unless the signal interacts with the pump level as in direct metastable level pumping. In P_p^{CS} for a four-level system σ_p^a is weighted by $1-\tau_1/\tau_{20}$ or $1/\beta_{2e}- \beta_{12}- \tau_1/\tau_{20}$. This accounts for the finite population of the lower lasing level. If τ_1/τ_{20} is large, then level 1 can be significantly populated. Since the ions do not return to the ground state, they are not available to absorb the pump light. Therefore, as the population of level 1 increases P_p^{CS} increases.

The saturation powers for a three-level system reduce to those of a two-level system as the energy gap between the pump and metastable levels approaches zero ($\eta_p \rightarrow 1$, $\beta_{3e} \rightarrow 1$, and $\beta_{2e} \rightarrow 1$). However, P_p^{CS} for a three-level system does not approach P_p^{IS} for a two-level system, since a signal beam in a three-level system by definition (Section IIIA) never interacts with the pump level. Reduction from a four-level system to a three-level system only occurs for the pump parameters P_p^{IS} and P_p^{CS}, which do not contain absorption from the lower lasing level.

II.3.4 *Useful Expressions*

In this section, some system independent parameters that are useful in modelling fiber amplifiers and lasers when only one pump beam and one signal beam are present are defined. For notational simplicity the k indices are omitted. Solving the differential equations for $P_p(z) >> P_s(z)$, yields the small signal gain coefficient

$$\gamma(z,\lambda_s) = \frac{1}{P_s}\frac{\partial P_s(z)}{\partial z} = \frac{P_p(z)\alpha_p P_p^{IS}}{P_s^{CS}\left(P_p^{IS} + P_p(z)\right)} - \alpha_s \tag{20}$$

As the pump power approaches infinity, the gain approaches the maximum fiber gain $G_{max} = \exp(\gamma_{max}L)$. G_{max} is given in Table II.2 in terms of α_p and α_s and the saturation power ratio δ, also defined in Table II.3. For a two-level system the expression for the maximum gain reduces to that given in [52].

For the two-level system approximation, the gain coefficient when multiple beams are present is given by

$$\gamma(z,\lambda_k) = \frac{1}{P_k^{CS}} \frac{\sum_{j=1}^{K_p+K_s} P_j\alpha_j}{1 + \sum_{j=1}^{K_p+K_s} \frac{P_j}{P_j^{IS}}} - \alpha_k \tag{21}$$

For the three- and four- level systems the multiple beam gain coefficient expressions are quite lengthy and are therefore not given here. When only one pump and one signal beam are present a single transcendental equation for the signal gain can be obtained. Expressions are first obtained from the signal equation, (18), for the absorbed and output pump powers. Substituting these into the pump equation, (17), yields

$$P_p^{in} - P_p^{in}\left(\frac{G}{G_{\max}}\right)^{S}\exp\left\{P_s^{in}(G-1)\left[\frac{P_s^{CS}}{P_s^{IS}P_p^{IS}} - \frac{1}{P_p^{CS}}\right]\right\} = P_s^{CS}\left[\alpha_s L + \ln(G)\right] + \frac{P_s^{CS}}{P_s^{IS}}P_s^{in}(G-1) \tag{22}$$

This equation is valid for any system and is reduced to the two-level system equation in Ref. [52] by setting $P_p^{CS} = P_p^{IS}$ and $P_s^{CS} = P_s^{IS}$.

The fiber length that maximizes the gain, L_{opt}, can be found by solving (17) and (18) while setting the output pump power to the threshold power P_p^{th}.

$$P_p^{th} = \frac{1}{\dfrac{\alpha_p}{\alpha_s P_s^{CS}} - \dfrac{1}{P_p^{IS}}} \tag{23}$$

This is the pump power at which the small signal gain coefficient at the fiber output equals zero, found by setting $\gamma(L_{opt},\lambda_s) = 0$ in (20). The amplifier length that maximizes the signal-to-noise ratio is less than the length that maximizes the gain, because of the extra noise generated in the low gain end of the fiber [53]. For a four-level system the gain increases with fiber length to a limit determined by the background loss and ASE.

II.3.5 Excited State Absorption

In this section an approximate solutions are given for fiber amplifiers with excited state absorption (ESA). ESA occurs when an ion in the metastable level is promoted to a higher energy level by absorbing either a pump or signal photon. An ion in the excited state returns to the metastable or ground level through phonon interactions and spontaneous emission so that ESA results in an effective loss. This occurs, for example, at the 514, 655, and 810 nm Er^{3+} pump wavelengths and at the 1320 nm Nd^{3+} signal wavelength. The energy level diagram for a three-level ion with ESA is shown in Fig. II.3. The inclusion of ESA leads to differential equations that can only be solved numerically [54]. However, approximate closed form solutions can be obtained for certain cases.

Pump and signal ESA for two- three-, and four-level systems are considered. In all cases it is assumed that (i) decay from the ESA level is to the metastable level only ($1/\tau_{e0} = 0$) and that (ii) decay from the ESA level is rapid so that the upper state is negligibly populated. The latter assumption is valid for moderate power levels only, i.e., $\tau_{ESA} << \tau_2 P_i^{IS}/P_i^{ESA}$ where

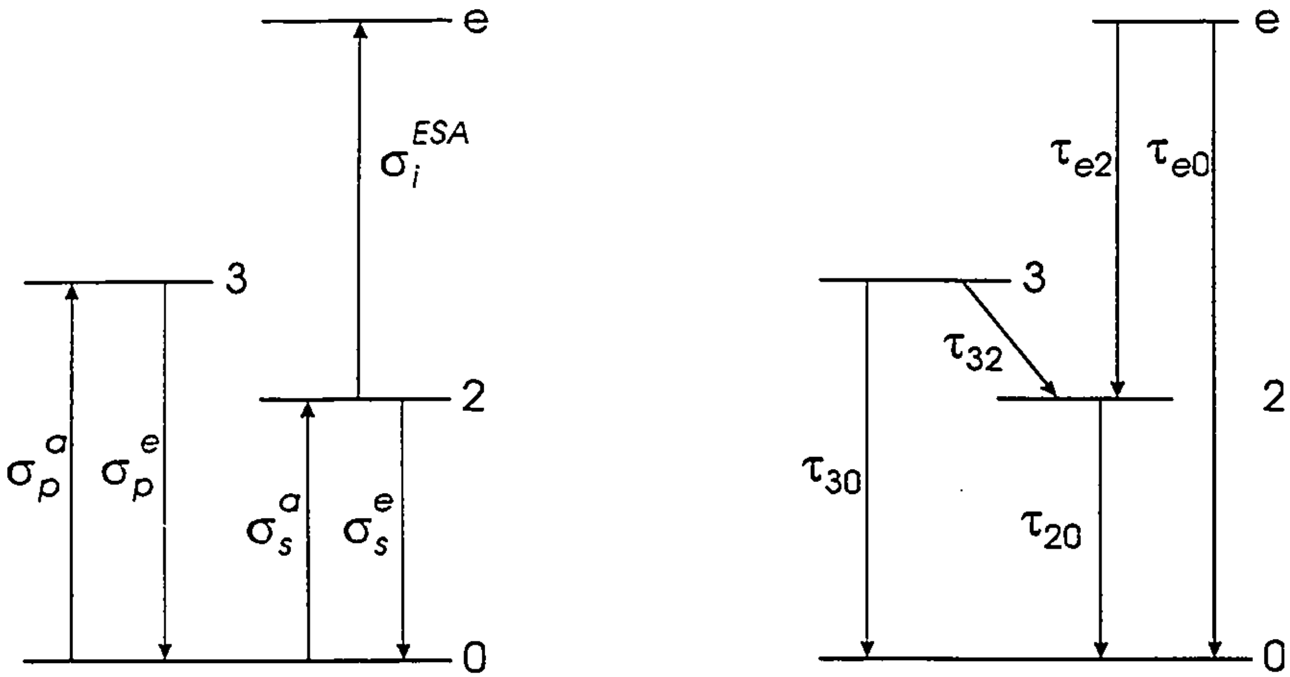

Fig. II.3 Energy level diagram for a three-level system with excited state absorption.

$P_i^{ESA} = A_{eff}/(\eta_p\Gamma_p\sigma_i^{ESA})$ and σ_i^{ESA} is the pump (i=p) or signal (i=s) ESA cross section.

With these assumptions the original differential equations, (1) to (6), are modified by adding a term equal to $-N_2\sigma_i^{ESA}$ within the parentheses of the right-hand side of (5) for pump ESA, or (6) for signal ESA [54]. Solving the differential equations, (1)-(6), using the procedure outlined in Section III.C, for pump ESA yields

$$P_p^{out} = P_p^{in}\left[\frac{P_p^{in} + \xi_p^{IS}P_p^{IS}}{P_p^{out} + \xi_p^{IS}P_p^{IS}}\right]^{\xi_p^{IS}-1} \exp\left\{-\alpha_p L + \frac{P_s^{in} - P_s^{out}}{P_{p,ESA}^{CS}(P_p)}\right\} \tag{24}$$

$$P_s^{out} = P_s^{in}\left[\frac{P_p^{in} + \xi_s^{CS}P_s^{CS}}{P_p^{out} + \xi_s^{CS}P_s^{CS}}\right]^{\xi_s^{CS}} \exp\left\{-\alpha_s L + \frac{P_s^{in} - P_s^{out}}{P_{s,ESA}^{IS}(P_p)}\right\} \tag{25}$$

where $\xi_p^{IS} = P_p^{ESA}/P_p^{IS}$, $\xi_s^{CS} = P_p^{ESA}/P_s^{CS}$, and the pump-power-dependent signal saturation powers are given by:

$$P_{p,ESA}^{CS}(P_p) = \frac{P_p^{CS}\left(\xi_p^{IS} P_p^{IS} + P_p\right)}{\xi_p^{IS} P_p^{IS} - P_p^{CS}/\eta_p + P_p\left(1 - P_p^{CS}/P_p^{IS}\eta_p\right)} \tag{26}$$

$$P_{s,ESA}^{IS}(P_p) = \frac{P_s^{IS}\left(\xi_p^{IS} P_p^{IS} + P_p\right)}{\xi_p^{IS} P_p^{IS} + P_p\left(1 - P_s^{IS}/P_s^{CS}\eta_p\right)} \tag{27}$$

As expected, when the ESA cross section approaches zero ($\xi \rightarrow \infty$), (24) and (25) agree with (17) and (18) and $P_{p,ESA}{}^{CS}$ and $P_{s,ESA}{}^{IS}$ approach $P_p{}^{CS}$ and $P_s{}^{IS}$, respectively.

Since these parameters depend on the pump power, a closed form solution does not exist unless the $P_s{}^{in}$ - $P_s{}^{out}$ terms can be neglected. This occurs, for example, during pump transmission measurements. Then (24) reduces to the expression derived by Digonnet [37]. If the $P_s{}^{in}$ - $P_s{}^{out}$ terms are significant, an approximate solution exists for weak ESA ($\xi_p{}^{IS}P_p{}^{IS} >> P_p$), where $P_{p,ESA}^{CS}$ and $P_{s,ESA}^{IS}$ can be approximated by their values for $\sigma_p{}^{ESA} = 0$. For example, consider an EDFA pumped at 815 nm, the optimum pump wavelength within the 800 nm band for silica fiber [55]. A fiber with NA = 0.2, core diameter $2a = 3$ μm, $2b = 1.5$ μm, and $\sigma_p{}^{ESA} = .03$ pm^2 has $\xi_p{}^{IS}P_p{}^{IS} = 4$ mW. Since typical input pump power at this wavelength is about 50 mW, pumping at 810 nm is usually in the strong ESA regime. Therefore, (24) and (25) are only useful in this regime for calculating the small signal gain and finding the optimum pump wavelength.

Efficient 800 nm pumping of Er^{3+} depends strongly on the pump wavelength. The ideal pump wavelength for a particular fiber occurs where $\sigma_p{}^a$ - $\sigma_p{}^{ESA}$ has a maximum. The expression for the pump transmission in the absence of signal light, (24), gives a simple method for finding the maximum of $\sigma_p{}^a$ - $\sigma_p{}^{ESA}$ and the ratio $\xi_p{}^{IS}$ by pump transmission measurements. At low input pump power the transmission is equal to $T_{min} = \exp(-\alpha_p L)$ and at high input pump power the transmission is equal to $T_{max} = \exp(-\alpha_p L/\xi_p{}^{IS})$. The ideal pump wavelength can be found by finding the wavelength for which the change in pump transmission, $\Delta T = T_{max}/T_{min}$, is maximized. This figure shows that as the relative strength of the ESA increases ($\xi_p{}^{IS} \rightarrow 0$), the maximum transmission decreases. Figure II.4 shows how the pump transmission depends on the ratio of aborption and ESA cross sections. $\xi_p{}^{IS}$ can also be measured since $\xi_p{}^{IS} = \ln(T_{min})/\ln(T_{max})$. Thus, the optimum pump wavelength can be found with only one tunable laser. This technique is simpler and requires less equipment than pump/probe measurements that require two light sources at the pump wavelength [56].

Equations (24)-(27) describe the solution in the presence of pump ESA. The solution for signal ESA is given by

$$P_s^{out} = P_s^{in}\left[\frac{P_s^{in} + \xi_s^{IS}P_s^{IS}}{P_s^{out} + \xi_s^{IS}P_s^{IS}}\right]^{\xi^{n}-1} \exp\left\{-\alpha_s L + \frac{P_p^{in} - P_p^{out}}{P_{s,ESA}^{CS}(P_s)}\right\} \tag{28}$$

$$P_p^{out} = P_p^{in}\left[\frac{P_s^{in} + \xi_p^{CS}P_s^{CS}}{P_s^{out} + \xi_p^{CS}P_s^{CS}}\right]^{\xi^{\prime}} \exp\left\{-\alpha_p L + \frac{P_p^{in} - P_p^{out}}{P_{p,ESA}^{IS}(P_s)}\right\} \tag{29}$$

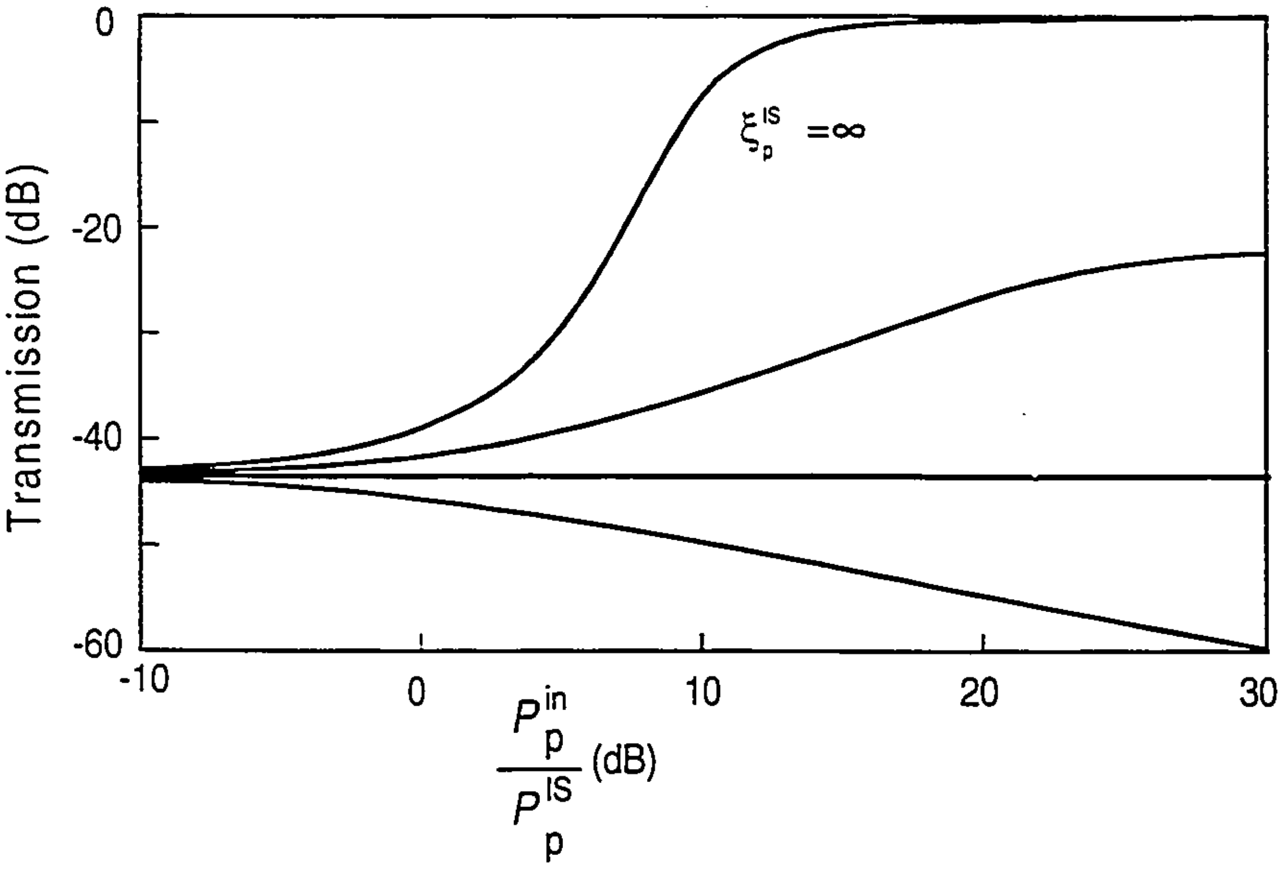

Fig. II.4. Effect of excited state absorption on pump transmission measurements.

where $\xi_s^{IS} = P_s^{ESA}/P_s^{IS}$, $\xi_s^{CS} = P_s^{ESA}/P_s^{CS}$, and the power dependent pump saturation powers are given by

$$P^{CS}_{s,ESA}(P_s) = \frac{P_s^{CS}\left(\xi_s^{IS}P_s^{IS} + P_s\right)}{\xi_s^{IS}P_s^{IS} - P_s^{CS} + P_s\left(1 - \eta_p P_s^{CS}/P_s^{IS}\right)} \tag{30}$$

$$P^{IS}_{p,ESA}(P_s) = \frac{P_p^{IS}\left(\xi_s^{IS}P_s^{IS} + P_s\right)}{\xi_s^{IS}P_s^{IS} + P_s\left(1 - \eta_p P_p^{IS}/P_p^{CS}\right)} \tag{31}$$

II.3.6. Distributed Loss

In this section corrections to the doped fiber transmission measurements are given for fibers experiencing significant background loss. Background loss in a fiber amplifier or laser is usually negligibly small compared to absorption coefficients and discrete losses. The excess loss may be significant however for lightly-doped fibers, for losses at the signal wavelength of a four-level ion, for wavelengths far from absorption maxima, and for wavelengths beyond the low-loss region of the host glass. For example, in the 2 µm signal wavelength region a Tm^{3+}-doped silica fiber can have background loss as high as 70 dB/km. If the pump and signal beams have loss per unit length equal to q_p and q_s, respectively, then the differential equations are adjusted by adding $-q_pP_p$ to the right-hand side of (5) and $-q_sP_s$ to the right-hand side of (6). These coupled differential equations do not have a closed form expression. A solution does exist, however, when only one beam is present, which is the case during transmission measurements. Then the output power is found by solving

$$P_i^{out} = P_i^{in} e^{-(\alpha_i + q_i)L} \left(\frac{P_i^{in} + (1 + \alpha_i/q_i)P_i^{IS}}{P_i^{out} + (1 + \alpha_i/q_i)P_i^{IS}} \right)^{\alpha_i/q_i} \tag{32}$$

This solution approaches that given by (17) and (18) as the losses approach zero ($q_i \rightarrow 0$). By fitting (32) to transmission curves, background loss can be found. If background loss is significant, then device modelling must be done numerically [57].

II.4. Fiber Laser Theory

II.4.1. General Procedure

Ring and linear lasers are now modelled in terms of the attenuation coefficients and saturation powers. Simple analytical expressions, which can be differentiated to optimize the laser design, are derived for the slopes and thresholds of fiber lasers. The fiber amplifer gain equations (17) and (18) have the same form for the various ionic systems so that the laser model is system independent. Typical linear and ring fiber lasers are shown in Fig. II.5. A linear fiber laser with one single-pass pump beam is discussed, although the model can be extended to more general cases. The linear laser is assumed to have two counterpropagating signal beams at the laser wavelength and the ring laser is assumed to contain an optical isolator so that it has one unidirectional signal beam at the signal wavelength. The output power of linear lasers will be derived first and then the results for ring lasers will be listed. It can be quite difficult to measure fiber-to-mirror coupling losses, so experimental agreement for ring lasers is usually better than for linear lasers.

The output power of the fiber laser is found by applying the expressions for the output signal power (18) and absorbed pump power (17) through one cavity round trip (including losses at intracavity elements and at the mirrors and/or output couplers) and setting the net round trip gain equal to unity. Eliminating the absorbed pump power from the coupled equations (17) and (18) allows derivation of a single equation for the output signal power in terms of the input pump power.

For the linear laser shown in Fig. II.5a, the left-hand mirror has a reflectivity R_1 and the right-hand mirror has a reflectivity R_2 at the lasing wavelength. Both mirrors are transparent at the pump wavelength so that the pump has only one pass through the fiber. Results are given in terms of P_p^{in}, the pump light input to the doped fiber. Discrete loss elements with single-pass transmissions of ε_1 and ε_2 are located between the doped fiber ends and the mirrors. These losses account for intracavity components such as tuning elements and the fiber-to-mirror coupling loss. At any point in the fiber there is pump light propagating to the right and a laser light standing wave that is a superposition of right and left propagating laser light. The output laser power is given by

$$P_{Las} = \left(1 - R_2\right)\varepsilon_2 P_R^{out} \qquad (32)$$

where P_R^{out} is the power at the fiber lasing wavelength out from the right end of the doped fiber. Taking the signal wavelength to be the lasing wavelength, (18) is applied through one round trip of

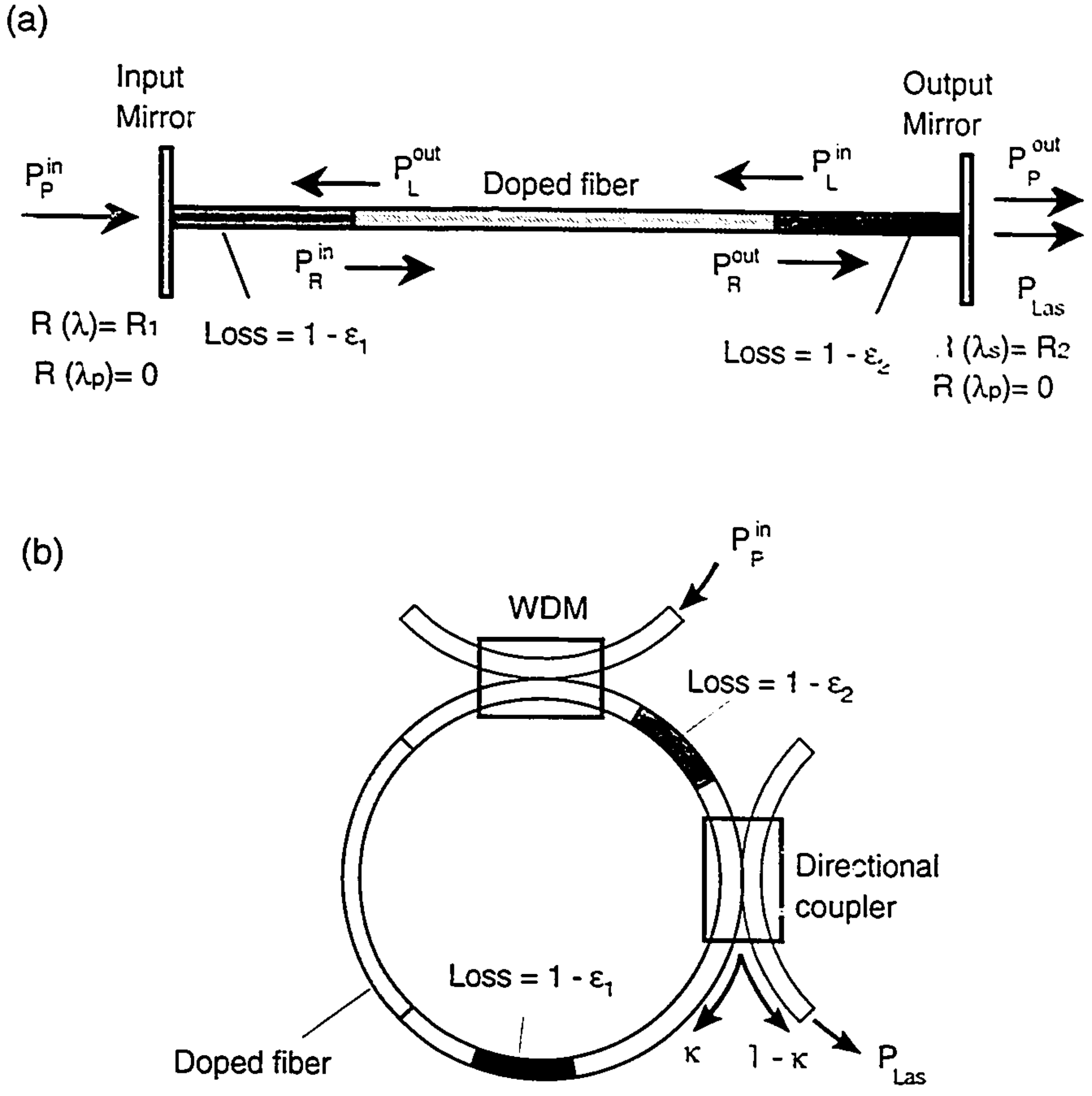

Fig. II.5. Fiber laser configurations for (a) linear laser and (b) ring laser the laser cavity, asssuming that power at the lasing wavelength is conserved. This gives

$$P_R^{out} = \varepsilon^2 R^2 P_R^{out} \exp\left\{ -2\alpha_s L - \frac{2P_p^{abs}}{P_s^{CS}} - \frac{2P_s^{abs}}{P_s^{IS}} \right\} \tag{33}$$

where $R^2 = R_1 R_2$, $\varepsilon = \varepsilon_1 \varepsilon_2$, P_p^{abs} is the pump power absorbed in its single pass through the fiber, and P_s^{abs} is the power absorbed at the lasing wavelength in the fiber. P_s^{abs} is negative since the fiber is generating power at the lasing wavelength. Referring to Fig. II.5a, the signal power absorbed in the fiber is given by

$$\begin{aligned} P_s^{abs} &= \left(\varepsilon_2^2 R_2 - 1\right) P_R^{out} - \left(\varepsilon_1^2 R_1 - 1\right) P_L^{out} \\ &= \left[\left(\varepsilon_2^2 R_2 - 1\right) - \left(\varepsilon_1^2 R_1 - 1\right) \varepsilon_2^2 R_2 \exp\left\{ -\alpha_s L - \frac{P_s^{abs}}{P_s^{IS}} - \frac{P_p^{abs}}{P_s^{CS}} \right\} \right] P_R^{out} \end{aligned} \tag{34}$$

From (18), for the single pass of the pump light one gets an expression for the absorbed pump power:

$$P_p^{abs} = P_p^{in} \left[1 - \exp\left\{ -\alpha_p L - \frac{P_p^{abs}}{P_p^{IS}} - \frac{P_s^{abs}}{P_p^{CS}} \right\} \right] \tag{35}$$

Taking the logarithm of (33) gives another expression for the absorbed pump power

$$P_p^{abs} = P_s^{CS} \left\{ \alpha_s L - \frac{P_s^{abs}}{P_s^{IS}} - \ln(\varepsilon R) \right\} \tag{36}$$

Substituting this expression for P_p^{abs} into (34) yields

$$P_s^{abs} = -T_{eff} P_R^{out} \tag{37}$$

where T_{eff} is the effective output transmission given in Table II.2. P_s^{abs} is negative since light is being generated at the laser wavelength. Substituting (36) and (37) into (35) results in a transcendental equation for P_R^{out} in terms of P_p^{in}:

$$P_s^{CS}\left[\alpha_s L - \ln(\varepsilon R) - \frac{T_{eff} P_R^{out}}{P_s^{IS}}\right] = P_p^{in}\left\{1 - (G_{max}\varepsilon R)^{-\delta}\exp\left[P_R^{out} T_{eff}\left(\frac{\delta}{P_s^{IS}} - \frac{1}{P_p^{CS}}\right)\right]\right\} \qquad (38)$$

This nonlinear equation is linearized by recognizing that, except for very high powers P_R^{out}, the argument of the exponential is approximately zero for three- and four-level lasers (see the following discussion). For two-level lasers the exponential argument always equals zero.

Simplifying (38) with this approximation and using (32) yields a linear equation for the fiber laser output power in watts.

$$P_{Las} = \eta\left(P_p^{in} - P_p^{th}\right) \qquad (39)$$

which defines the slope efficiency η and pump power threshold P_p^{th} given in Table II.4. The expressions in Table II.4 for the ring laser shown in Fig. II.5b are similarly derived by assuming that the laser power is conserved through one cavity round trip.The fiber laser linear output equation (39) is derived by assuming that the argument of the exponential in (38) is small so that it can be set to zero. This is a valid assumption for moderate power levels since for $P_s^{IS} \approx P_s^{CS}$ and $P_p^{IS} \approx P_p^{CS}$ the exponential argument is approximately zero. However, the argument can be significant for large values of P_R^{out}. In that case, the exponential term gives a correction for the finite lifetime of the pump level which saturates the laser output at high pump powers. This effect is predicted by a numerical solution of the nonlinear equation (38). This effect is not predicted by the two-level model, which assumes infinitely rapid decay from the pump level. The power at which the laser begins to saturate increases as the three- and four-level systems approach the two-level system, i.e., as $\tau_{32} \to 0$ and $\tau_{10} \to 0$. As an example, consider a 125 ppm ring EDFL pumped at 980 nm with b = 1.15 μm, NA = 0.3 m, ε = 0.2, and κ = 0.57 (see Fig. 2 of Ref. [43]). Figure II.6 shows, as a function of pump power, the output power calculated using the linear approximation (39), and calculated using the nonlinear equation (38). As shown in the figure, saturation is smaller for the longer fiber. It is also reduced for a larger core diameter or for a higher dopant concentration. Since slope saturation increases as the pump level lifetime increases, it can also be reduced by pumping directly to the metastable level. For a properly designed laser, this saturation is not observed since pump level saturation is only significant for fiber lengths much shorter than the optimum length. Therefore, the linear solution, (39), can be taken as exact for all practical cases.

Threshold, P_p^{th} and slope, η	Linear laser	Ring laser
$\eta =$	$\frac{\eta_q \varepsilon_2 (1 - R_2)}{T_{eff}} \frac{P_s^{IS}}{P_s^{CS}} \left[1 - (G_{max} \varepsilon R)^{-\delta} \right]$	$\frac{\eta_q \varepsilon_2 (1 - \kappa)}{T_{eff}} \frac{P_s^{IS}}{P_s^{CS}} \left[1 - (G_{max} \varepsilon \kappa)^{-\delta} \right]$
$P_p^{th} =$	$\frac{h\nu_p P_s^{CS} (\alpha_s L - \ln(\varepsilon R))}{1 - (G_{max} \varepsilon R)^{-\delta}}$	$\frac{h\nu_p P_s^{CS} \left[\alpha_s L - \ln(\varepsilon \kappa) \right]}{1 - (G_{max} \kappa \varepsilon)^{-\delta}}$

Table II.4. Fiber laser slope efficiencies and threshold powers. Laser output power is given by $P_{Las} = \eta(P_p^{in} - P_p^{th})$.

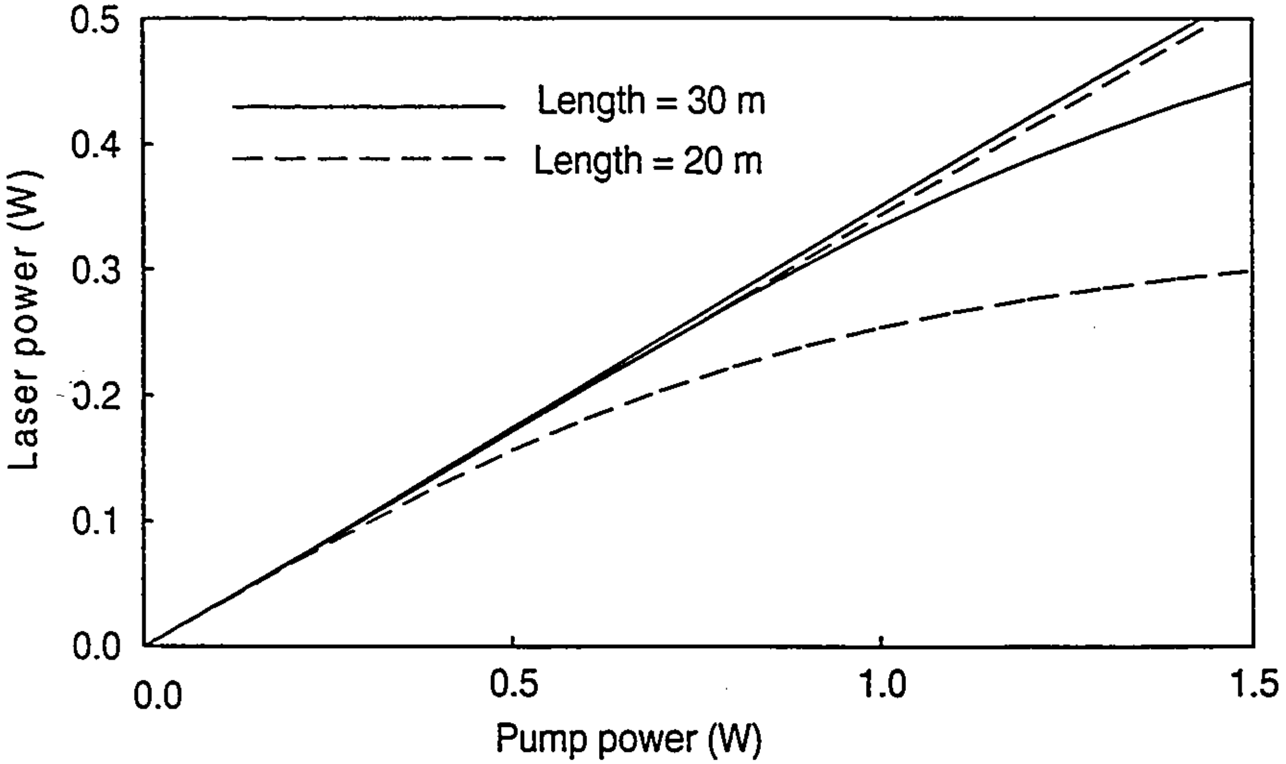

Fig. II.6. Linear and exact solution to laser output power for a ring EDFL. The exact solution saturates at high power.

II.4.2 Solutions

Table II.4 lists expressions for the slopes and thresholds of a linear and ring. In the expressions for slope the two loss terms are distinct which means that fiber laser performance depends on the placement of the loss element with respect to the output coupler. The fiber laser expressions presented in Table II.4 are system independent since they are functions of only the measured attenuation coefficients and saturation powers.

For laser design optimization the expressions from Table II.4 can be differentiated to find the optimum fiber length and output coupling coefficient for a given fiber and input pump power. If the wavelength dependence of α_s, and P_s^{IS} are known, then the lasing wavelength can also be predicted. For any fiber laser the fiber must be longer than the length at which the maximum round trip gain equals the round trip losses, i.e., where $G_{max}= 1/\varepsilon\kappa$ for a ring laser. The minimum length L_{min} is found by setting the slope expressions in Table II.4 equal to zero. For a ring laser the minimum length is given by

$$L_{min} = \frac{-\ln(\varepsilon\kappa)}{\frac{\alpha_p}{\delta} - \alpha_s} \tag{40}$$

The expression is the same for a linear laser except that κ is replaced by *R*. Since the maximum gain increases with length, the slope increases as the length increases, approaching the quantum efficiency for a lossless cavity. As the length increases, the threshold of a three-level fiber laser also increases. Therefore, a three-level fiber laser has an optimum length (for a given wavelength) L_{opt} that maximizes the laser output power. It is obtained by differentiating the expression for the laser output power with respect to *L* and putting the result equal to zero. For a ring laser it is given by

$$L_{opt} = \frac{1}{\alpha_p - \delta\alpha_s} \ln\left[\frac{P_p^{in}(\alpha_p - \delta\alpha_s)}{P_s^{CS}\alpha_s(\varepsilon\kappa)^{\delta}}\right] \tag{41}$$

Again, the expression is the same for a linear laser except that κ is replaced by *R*. A four-level laser is optimized with the fiber length at which most of the pump power is absorbed. Beyond that length, background loss can diminish the laser performance. For a given fiber length, a transcendental equation can be obtained for the optimum output coupler reflectivity. This question was discussed in Ref. [58] for a two-level system and will not be addressed here.

Some insight into the variation in lasing wavelength with fiber length can be gained from the expressions for threshold power [38]. Lasing occurs at the wavelength at which the threshold is minimum. If $G_{max} >> 1$, then the expressions for the pump threshold in Table II.4 depend mainly on the numerator, which involves a tradeoff between the P_s^{CS} and $[\alpha_s L - \ln(\varepsilon\kappa)]$ terms. At short fiber lengths, the P_s^{CS} term dominates so that lasing occurs where P_s^{CS} is a minimum, i.e., close to the gain peak. As the fiber length increases the $\alpha_s L$ term grows, driving the wavelength to regions where α_s is smaller, i.e., at longer wavelengths. At longer lengths there is a region of low population inversion at the output end of the fiber that reabsorbs signal light, preferentially at shorter wavelengths. Thus, longer three-level fiber lasers without tuning elements tend to favour lasing at longer wavelengths. For example, EDFLs tend to lase at 1.56 μm where the absorption is low, not at 1.53 μm where the emission is strongest. Similarly, lasing occurs at longer wavelengths when the cavity losses are high [59]. Cavity losses can therefore be minimized by minimizing the lasing wavelength. For four-level fiber lasers, α_s is zero, so the lasing wavelength does not vary as much with fiber length. A four-level laser will tend to lase near the gain peak, independent of the fiber length, since this is where P_s^{CS} is minimum and G_{max} is maximum.

II.5 Comparison with Existing Models

The results of this work will now be compared to the literature. In 1988 Digonnet and Gaeta [51] published an analysis of four-level fiber amplifiers and lasers, neglecting saturation of the pump absorption. In 1990 this analysis was extended to the three-level system [37] and the effects of pump saturation and pump ESA were also included. Their analysis assumes unity pump quantum efficiency ($\eta_p = 1$) and instantaneous decay from the pump level to the metastable level ($\beta_{3e} = 0$) and from the terminal lasing level to the ground level ($\beta_{12} = 0$ and $\tau_1 = 0$). Equation (17) is the same as their expression for the single-pass small-signal gain except that they neglect the $P_s^{in} - P_s^{out}$ term. They also derived expressions for the slope and threshold. Their expressions for the threshold and slope of a linear laser with $R_1 = 1$, and a small round trip loss are the same as those in Table II.4 if $\varepsilon_1 = 1$, $\varepsilon^2 R_2 \approx 1$, $G_{max}^{-\delta} = 0$, and their round trip loss parameter is set equal to $1 - \varepsilon_2^2 R_2$.

Saleh et al. [42] derived analytic equations for the gain of a two-level system that Pfeiffer and Bulow [52] used to derive expressions for the maximum gain, and the gain as a function of the input powers. The results of this work are the same for a two-level system. In a subsequent paper Pfeiffer and Bulow [43] gave expressions for the threshold and slope of a two-level ring laser with intracavity loss. The two-level laser model in Table II.4 agrees with their results.

Nielsen et al. [40] gave a two-level graphical method, requiring knowledge of the cross sections, for finding the slope, threshold, and wavelength of a linear EDFL with no intracavity losses. Table II.4 agrees with their results when $R_l = 1$, and $\varepsilon_1 = \varepsilon_2 = 1$. Mignon and Desurvire [39] gave an analytical two-level model for a linear EDFL that results in two coupled equations which must be solved numerically. With some approximations, they derive an expression for the slope of a laser with $R_l = 1$ and no losses ($\varepsilon_1 = \varepsilon_2 = 1$) that agrees with Table II.4. Chen et al. [38] derived the threshold pump power, but not the slope, of a linear EDFL. The threshold pump power given in Table II.4 agrees with their threshold after considerable rearrangement.

Urquhart [41] presented an analytical model for a Pr^{3+}-doped fiber amplifier (PDFA) which includes the intermediate levels. Rearranging his transcendental gain equation ((8) in [41]) and identifying terms results in (22) except that he sets all overlap integrals to unity ($\Gamma_i = 1$). Therefore, results here written in terms of the saturation powers agree with his PDFA model.

II.6 Experiment

The theory was compared to experimental results for an Er^{3+}-doped-fiber amplifier, an Er^{3+}-doped-fiber ring laser, and a Tm^{3+}-doped-fiber linear laser. The two-level approximation of the three-level model was used in deriving the theoretical curves, i.e., it was assumed that $P_p^{CS} = P_p^{IS}$ and $P_s^{CS} = P_s^{IS}$. The parameters α_k and P_k^{IS} were determined by transmission measurements at the pump and signal wavelengths. Two different tunable Ti:Sapphire lasers were used for the pump transmission measurements, one centred at 790 nm for the Tm^{3+} ion absorption band, and one centred at 980 nm for the Er^{3+} ion absorption band. Up to 100 mW of the pump power was coupled into the fibers by a long focal length lens (f=30 cm) followed by a short focal length lens (f=5 mm) lens. The Er^{3+}-doped fiber has a cutoff wavelength of 925 nm, and an erbium concentration of about 340 ppm. Transmission experiments at the signal wavelengths were done with the Tm^{3+}-doped fiber laser described below and the Q-switched Er^{3+}-doped fiber laser described in Section IV.2 operating in CW mode. The Tm^{3+}-doped fiber has a core diameter of 5 μm, a cutoff wavelength of 1.32 μm, and a thulium concentration of 250 ppm.

The Levenberg-Marquardt nonlinear optimization procedure was used to fit the theoretical transmission curve (19) to experimental points of the fiber transmission at pump and signal wavelengths. Fig. II.7 shows fits for three different pieces of Tm^{3+}-doped fiber at the 792 nm pump wavelength. Small differences in α_p and P_p^{IS} can be explained by the observed inhomogeneity in the fiber outside diamter along its length, which implies local variation in N_r, b, and Γ. The measured parameters for both fibers are summarized in Table II.5.

The gain of an EDFA as a function of 975 nm pump power was measured for 1542 and 1525 nm signals, -10 and -20 dBm input signal powers, and 10, 7 and 4 m long Er^{3+}-doped fibers. The EDFA was pumped by a 975 nm laser diode which delivered up to 16 mW into the erbium fiber. In fitting the model to the experiment the pump parameters were adjusted to account for the increase in wavelength of the pump laser diode from 967 nm at low power to 975 nm at maximum power. Table II.6 lists the maximum gain obtained for each fiber with 16 mW of pump power. The measured gain and theoretical curves from (17) and (18) are shown in Fig. II.8 for the 1542 nm signal gain in a 10 m fiber. Similar agreement between the theory and experiment were obtained for the other signal wavelengths and fiber lengths.

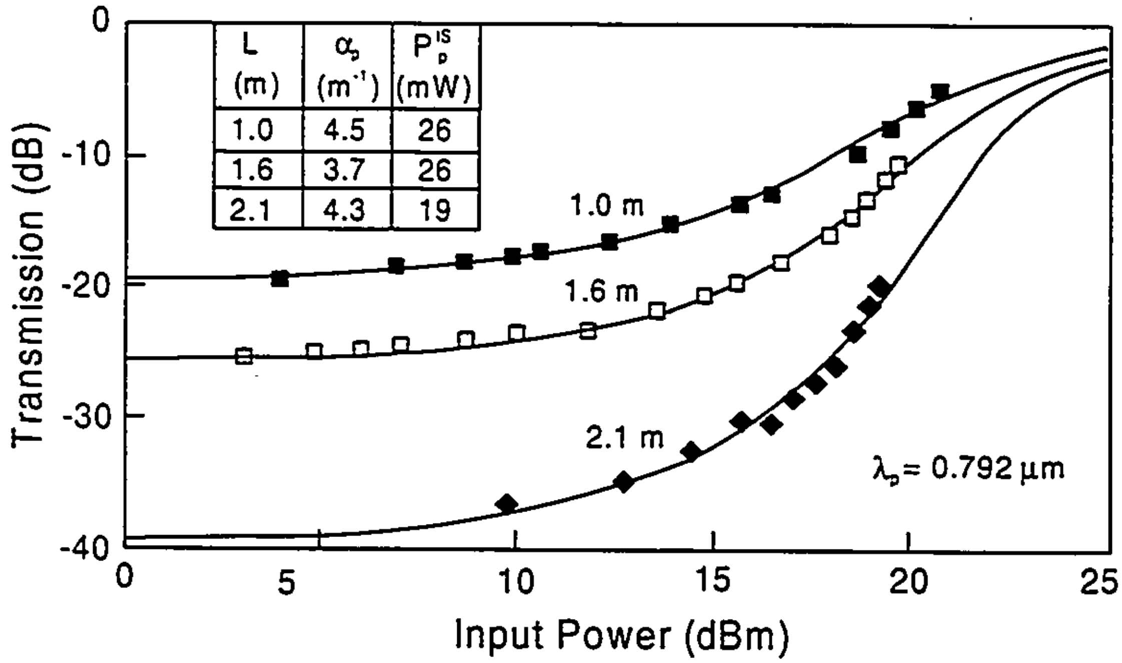

Fig. II.7. Transmission measurements with fitted curves for Tm^{3+}-doped fiber.

Unidirectional ring lasers, as in Fig. II.5b, were made with the three pieces of Er^{3+}-doped fiber and a variable directional coupler. The measured output powers and theoretical curves from (39) are shown in Fig. II.9 for the 10 m and 7 m fibers with different coupling ratios κ. As expected from the discussion in Section II.4.2, the laser wavelength indicated in Fig. II.9 increased with κ. The theoretical curves are not perfectly linear because of the variation in pump wavelength with power. For all Er^{3+}-doped fiber devices reasonable agreement between theory and experiment was obtained.

Erbium		
λ (nm)	α (m^{-1})	$h\nu P^{IS}$ (mW)
967	1.50	1.50
970	1.29	1.29
975	0.85	0.85
980	0.73	0.73
1525	1.32	0.16
1532	1.33	0.18
1543	0.72	0.22
1555	0.57	0.30
1557.8	0.50	0.32
1558.6	0.47	0.31
1560	0.45	0.32
1561	0.40	0.36
Thulium		
λ (nm)	α (m^{-1})	$h\nu P^{IS}$ (mW)
792	4.3	23
1920	0.1	20

Table II.5. Measured attenuation coefficients and saturation powers of erbium- and thulium-doped fibers.

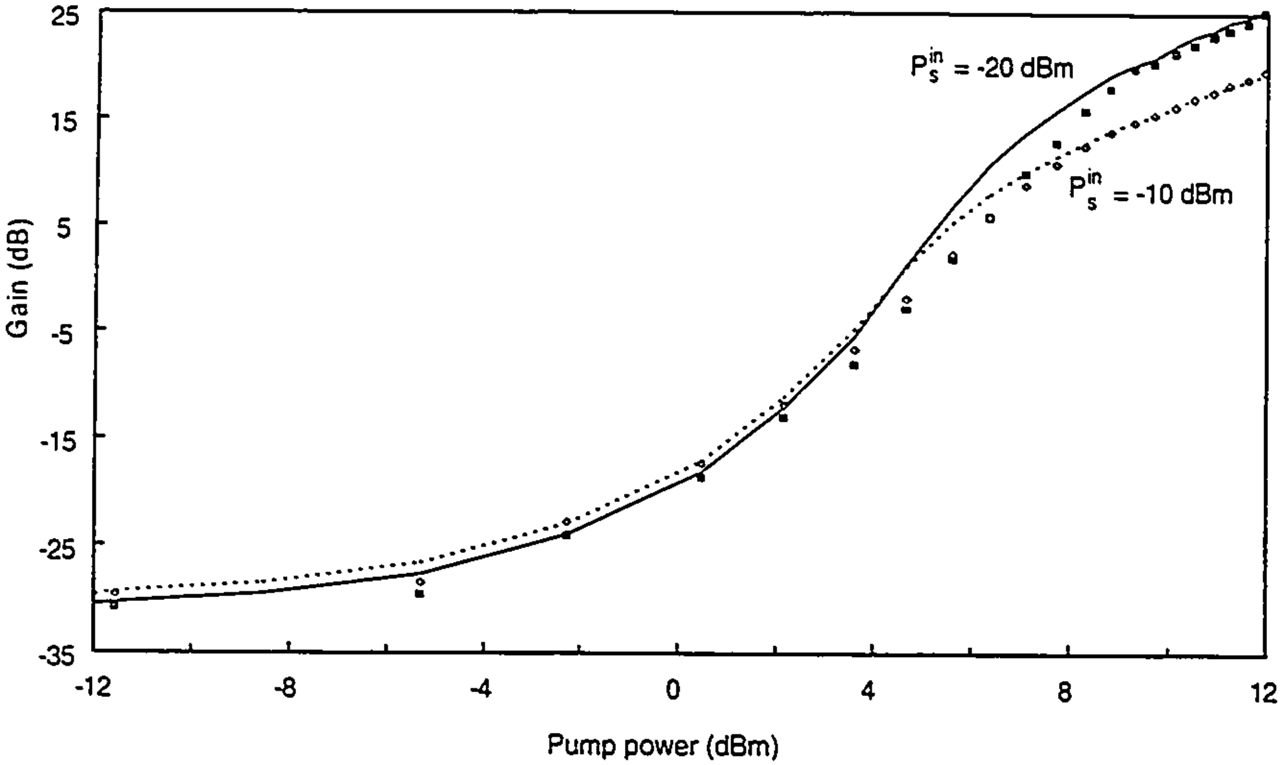

Fig. II.8. Measured and theoretical gain at 1542 nm of a 10 m EDFA.

Small discrepancies were probably caused by inaccuracy in measuring the pump coupling loss, imperfect calibration of the power meters, and the broad spectral distribution of the pump.

A linear Tm^{3+}-doped-fiber laser (Fig. II.5a) was also modeled with the measured saturation powers and absorption coefficients. The Ti:sapphire laser pumping beam at 792 nm was launched into the thulium fiber through a dielectric mirror with a 4 mm focal-length aspheric lens. The input mirror and various output couplers were butted directly to the fiber. The input mirror had reflectivity >99.5% from 1700-2100 nm and transmission > 90% at 792 nm, and the output couplers had transmission of 5%, 13%, 26%, and 72%. For a 2.1 m fiber and 26% transmission output coupler the threshold was 36 mW and the slope was 30% (corresponding to 75% quantum efficiency). A higher slope of 35% (over 85% quantum efficiency) was measured for a shorter 1.6 m fiber and 72% transmission output coupler. The observed threshold, however, increased to 70 mW. The lasing wavelength ranged from 1.92 to 1.96 μm, depending on the fiber length and the output coupler transmission. From Section II.4.2. this behaviour is expected since the wavelength of a fiber laser based on a three-level system depends strongly on the fiber length and cavity losses.

The determined saturation powers and absorption coefficients were used to model the Tm^{3+}-fiber laser characteristics for different fiber lengths (1.0, 1.6 and 2.1 m) and different transmissions of the output coupler (5%, 13%, 26%, and 72%). In all cases the calculated slope and threshold agreed within 20% of the measured values. Differences between the measurements and theory probably resulted from the large uncertainty in measuring the fiber-to-mirror coupling losses. The ring laser was easier to model since the losses could be directly measured.

For the Tm^{3+}-doped fiber, cross sections at the pump and signal wavelengths, as well as the average concentration, were derived from the expressions for the absorption coefficients and three-level saturation powers assuming that $\tau_{32} = \tau_3$ and $\beta_{3e}\sigma_p^e < \sigma_p^a$. Transmission measurements are thus useful to determine the total ion concentration when cross sections, which vary with fiber composition, are unknown [48].

Fiber length (m)	Signal wavelength (nm)	Input power (dBm)	Gain (dB)
4.2	1525	-20	13
4.2	1525	-10	11
4.2	1542	-20	12
4.2	1542	-10	11
7	1525	-20	22
7	1525	-10	17
7	1542	-20	20
7	1542	-10	16
10	1525	-20	25
10	1525	-10	19
10	1542	-20	23
10	1542	-10	17

Table II.6. Measured EDFA gain for 16 mW of pump power at 975 nm.

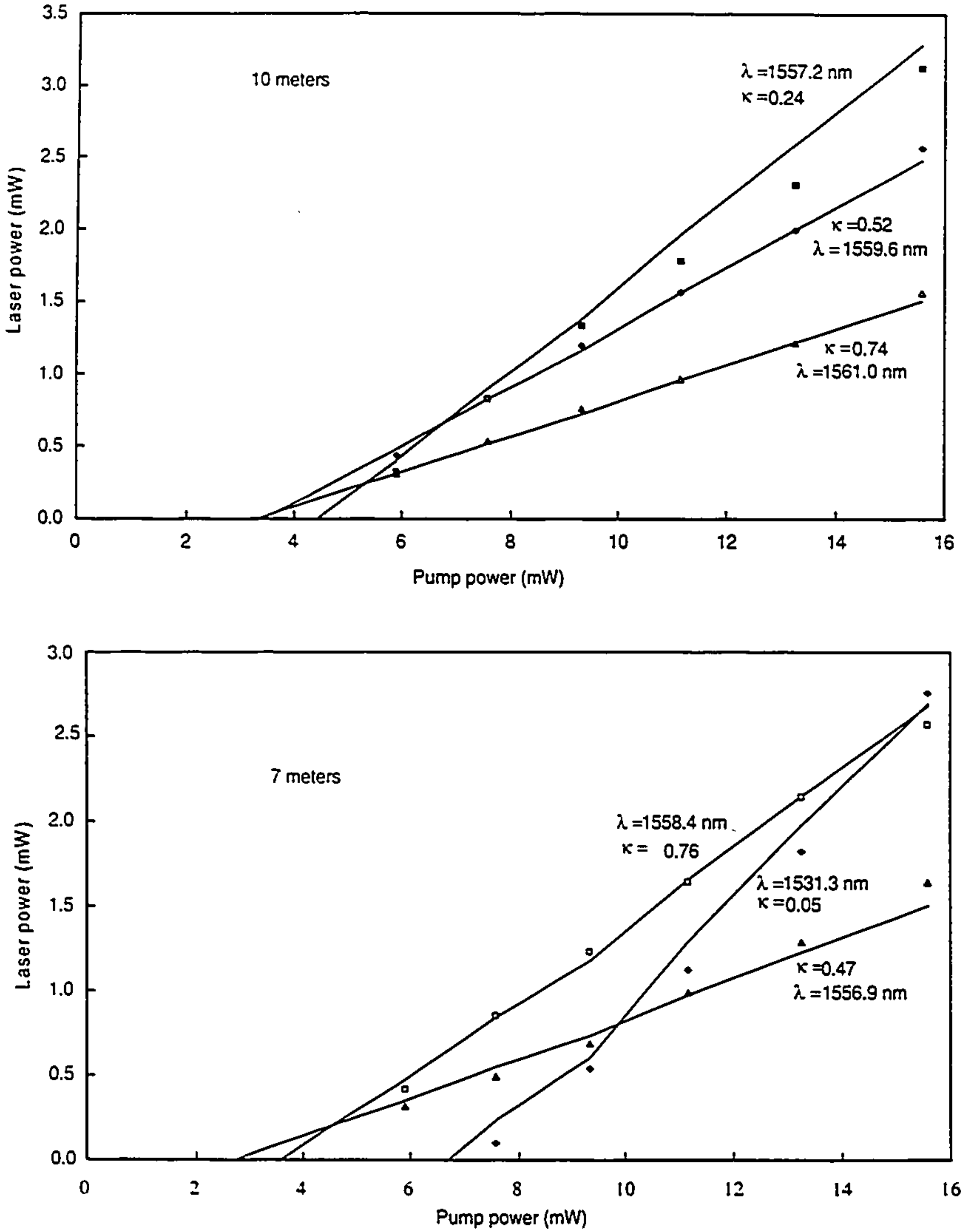

Fig. II.9. Measured and theoretical output power of Er^{3+}-doped-fiber ring lasers.

II.7 Conclusions

This analytical fiber amplifier and laser model is applicable to two-, three-, and four-level ions such as Er^{3+}, Nd^{3+}, Yb^{3+}, Tm^{3+}, and Pr^{3+}. New results include formulas for the gain and optimum length of fiber amplifiers and the slope, threshold, and minimum and optimum lengths of ring and linear fiber lasers. Fiber amplifier gain is expressed in terms of attenuation coefficients, intrinsic saturation powers, and cross saturation powers at the pump and signal wavelengths. These parameters can be directly found from one- and two-beam fiber transmission measurements without requiring knowledge of fiber dimensions, ionic cross sections, and decay times. The previous two-level model [42], [43] is a special case of this theory in which a three-level ion is pumped directly to the metastable level. In that case the intrinsic and cross saturation powers are equal. In the presented three- and four-level system theory, the introduced cross saturation power coefficient is not equal to the intrinsic saturation power coefficient, since pump and signal beams interact with different ionic energy levels. The fiber length maximizing the amplifier gain is found by solving the resultant amplifier equations while constraining the output pump power to be equal to the threshold pump power.

Approximate solutions for all systems with ESA at either the pump or signal wavelengths are given for fiber amplifiers. The solutions assume rapid decay from the ESA level and are valid for pump (signal) ESA when signal (pump) power is low or when the ESA cross section is small. A novel technique, requiring only one tunable light source, is described for finding the best pump wavelength when pump ESA is present.

System-independent formulas based on the attenuation coefficients and saturation powers are also given for the slope and threshold of ring and linear fiber lasers, with intracavity losses. This result simplifies fiber laser design by predicting the optimum values of variables such as fiber length and output coupling ratio. The theory also predicts how pump-level saturation leads to saturation of three- and four-level fiber lasers with shorter than optimum fiber lengths. This result is particularly important in relation to the recently introduced high power pump diodes. The amplifier and laser model compares well with previously published results. It has been verified experimentally for an EDFA, EDFL, and a Tm^{3+}-doped fiber laser.

Chapter III

Modelling EDFA Amplified Spontaneous Emission

III.1 Introduction

In the previous chapter amplified spontaneous emission (ASE) was neglected in the solution of the rate equations. As discussed this is valid for fiber lasers above threshold and for fiber amplifiers if the gain is less than 20 dB or the input signal power is greater than -20 dBm. However, an EDFA used as a preamplifier typically has greater than 20 dB gain and less than -20 dBm input signal power. In this application the EDFA significantly increases the receiver sensitivity by increasing the signal level to render the receiver thermal noise insignificant [60], [61]. The improvement in receiver sensitivity is less than the amplifier gain due to ASE noise [61]. In this chapter the amplifier model is refined to include the effects of ASE. The EDFA is modeled with the rate equations for the population levels and pump, signal, and noise powers using a two-level approximation. Numerically integrating the equations over the ASE bandwidth and the fiber length gives the signal gain and ASE output power.

This chapter is organized as follows. The absorption and emission cross sections of erbium, which govern the ASE spectrum, are described in Section 2. Modeling the generation of ASE is then described in Section 3. The ASE model is used to describe the fiber amplifier noise figure and signal-to-noise ratio (SNR) in Section 4. Experimental results are presented in Section 5 and conclusions are given in Section 6.

III.2 Absorption and Emission Cross Sections of Erbium

The ASE spectrum can be described in terms of effective absorption and emission cross sections defined in Chapter II. A detailed energy level diagram for Er^{3+} in silica is shown in Fig. III.1. Energy levels are identified by the spectroscopic nomenclature $^{2S+1}L_J$ where L is the azimuthal quantum number proportional to the ion orbital angular momentum, S is the resultant electron spin vector, and J is the inner quantum number proportional to the ion total angular momentum [62]. In rare-earth-doped glass the surrounding field causes a Stark splitting of the J manifolds into a maximum of

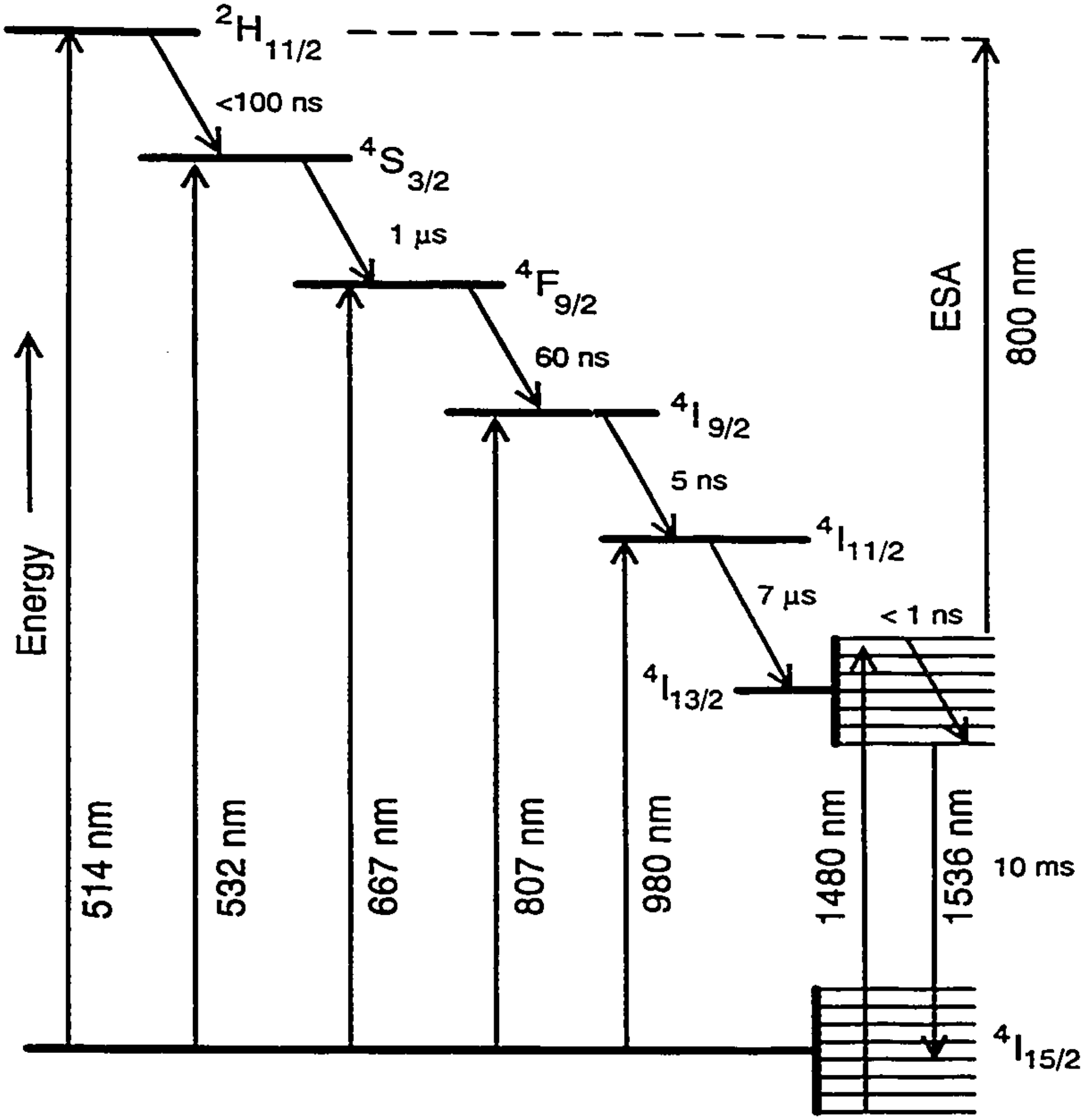

Fig. III.1. Detailed energy levels of Er^{3+} in glass.

$J+1/2$ levels as shown for the two bottom levels in Fig. III.1. Neighbouring ions experience different field distributions in the amorphous glass which produces inhomogeneous broadening of the energy levels. However, phonon coupling causes homogeneous broadening which dominates at room temperature [63], [64]. Thus, the emission and absorption resonances are quite broad and differ from one glass host to another. Broadened energy levels are advantageous since they are insensitive to small changes in the pump and signal wavelengths. Stark splitting also allows 1480 nm pumping of Er^{3+} directly from the bottom of the ground level to the top of the metastable level.

The cross sections depend on the energy values of all the components of the upper and lower levels, the inhomogeneous and homogeneous linewidths, and the relative strengths of the possible transitions. Because of the number of components in each level the cross sections can only be measured experimentally. For example, the lasing transition involves an upper level with seven components and a lower level with eight components and thus fifty-six possible transitions. Traditional Einstein analysis, which uses a two-level approximation, yields the Fuchtbauer-Ladenburg relationship for the cross sections [65]:

$$\sigma_i(\nu) = \frac{(\lambda/n)^2 g_i(\nu)}{8\pi\tau} \tag{43}$$

where n is the refractive index, τ is the spontaneous lifetime, and the lineshape function, $g(\nu)$, is the normalized value of the absorption or emission spectrum at frequency, ν. For the two level model, the absorption and emission cross sections must be equal. For EDFA's this is not the case, as illustrated by the spectra for the $^4I_{15/2}$ - $^4I_{13/2}$ transition in Fig. III.2. From Boltzmann theory, the relative population of two levels separated by energy ΔE, at temperature T is given by [65]:

$$\frac{N_2}{N_1} = \exp\left(-\frac{\Delta E}{kT}\right) \tag{44}$$

where k is Boltzmann's constant. Thus the lower components of the J-manifolds are more heavily populated. Therefore, as shown in Fig. III.1, absorption is stronger from the bottom of the $^4I_{15/2}$ manifold and emission is stronger from the bottom of the $^4I_{13/2}$ manifold. This explains why the absorption spectrum is shifted to higher energies (shorter wavelengths) as shown in Fig. III.2

An alternative to Einstein's analysis is McCumber's theory which uses the concept of a temperature dependent excitation energy to give the ratio of the two cross sections at any frequency

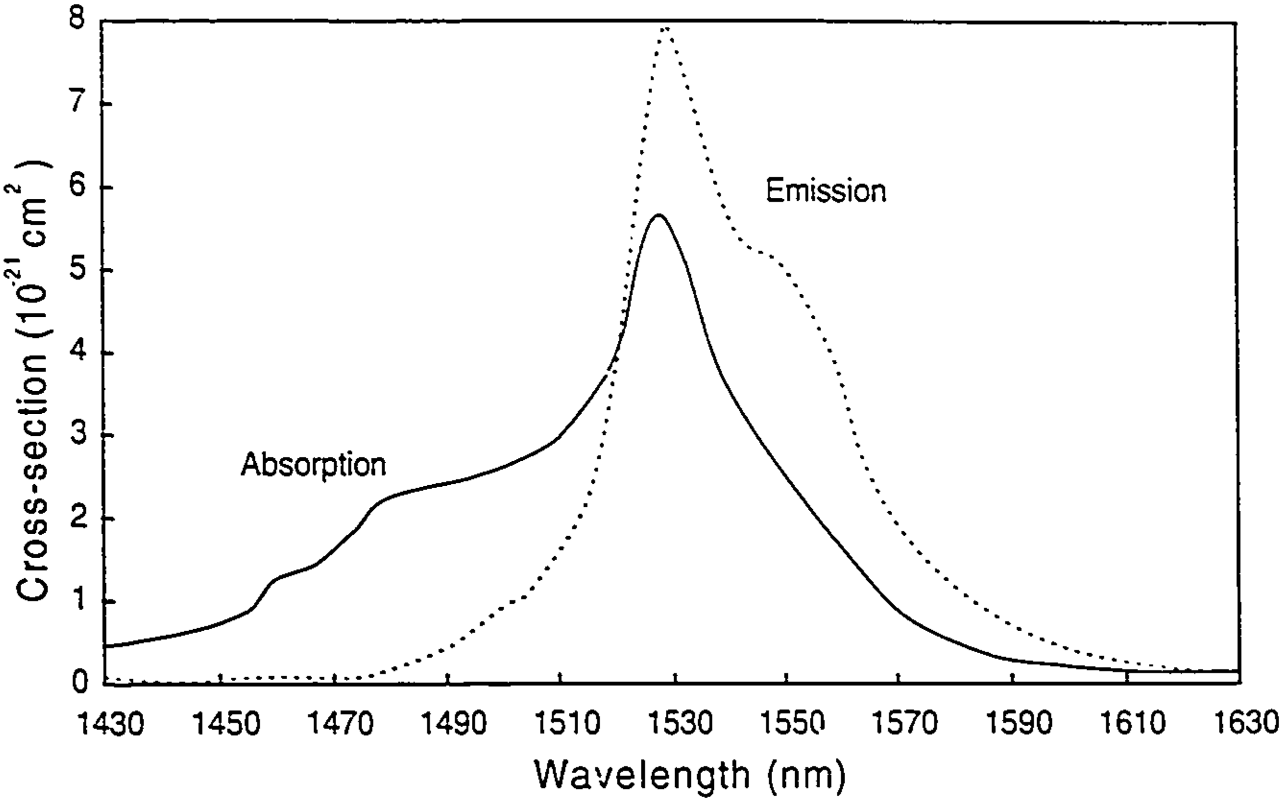

Fig III.2. Absorption and emission spectra of the Er^{3+} $^4I_{15/2}$-$^4I_{13/2}$ *transition in silica fiber.*

[66],[67]. With some assumptions about the energy levels this method can predict, with good accuracy, the emission cross section from the absorption cross section and the radiative lifetime, but it can not predict a priori either cross section.

Recall from the previous chapter that the absorption of pump radiation produces a population inversion ($\Delta N = N_2 - N_1 > 0$) which decreases in the direction of pump propagation. The signal and spontaneous emission are then amplified by stimulated emission from the population inversion according to:

$$\frac{dP(\nu,z)}{dz} = \gamma(\nu,z)P(\nu,z) \tag{45}$$

where

$$\gamma(\nu,z) = \left(N_2(z)\sigma_e(\nu) - N_1(z)\sigma_a(\nu)\right)\Gamma \tag{46}$$

Thus, amplification occurs when $\gamma(\nu,z)>0$ and absorption occurs when $\gamma(\nu,z)<0$.

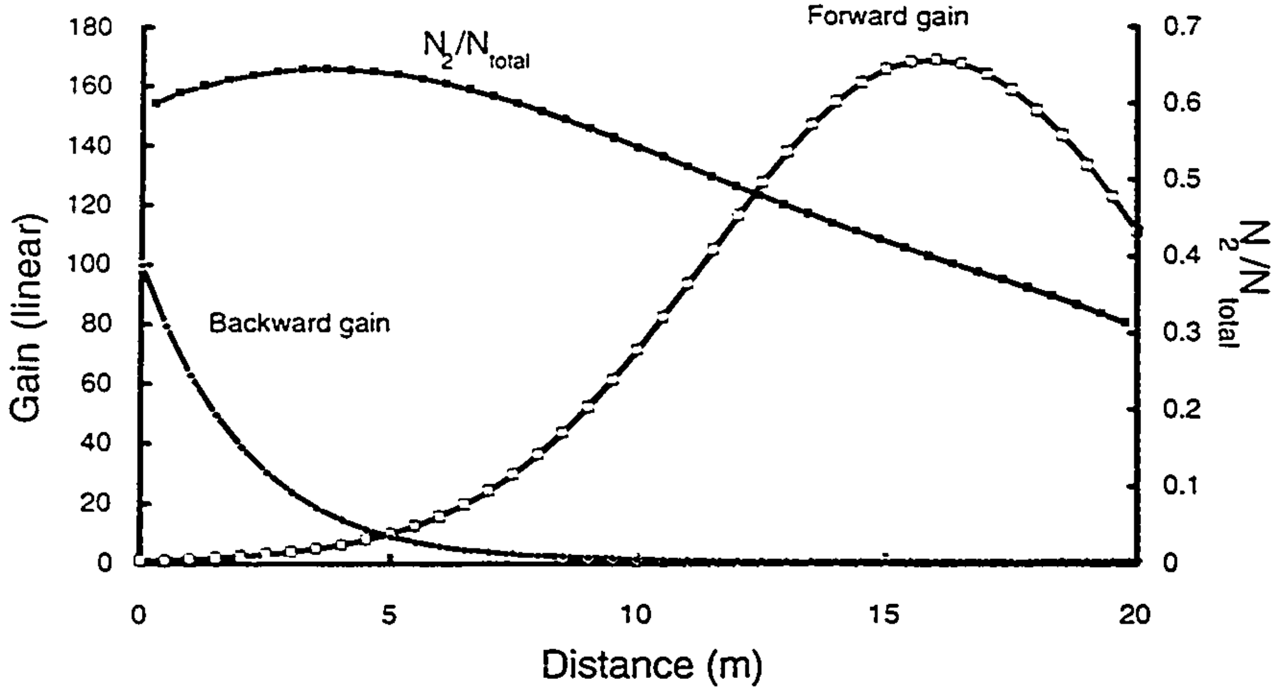

Fig. III.3. Population inversion and gain vs length of an EDFA.

The number of ions in the metastable level as a fraction of the total number of ions, N_t, and the gain in the forward and reverse directions with respect to the pump are shown for a typical fiber amplifier in Fig. III.3. For this example the fiber has a 3.2 µm core radius, 0.32 numerical aperture, $2.2\text{X}10^{18}$ cm^{-3} Er^{3+} ion density (100 ppm), signal and pump wavelengths of 1536 nm and 980 nm, and 20 mW of pump power. In the forward direction the gain first increases exponentially along the fiber and then levels off as the population inversion decreases. The gain reaches a maximum when $N_2\sigma_e = N_1\sigma_a$ ($\gamma = 0$) and thereafter decreases due to reabsorption of the signal. In the reverse direction, the signal is first absorbed until $\gamma = 0$ and then it increases along the fiber. To maximize the gain, the fiber length should be chosen so that $\gamma = 0$ at the end opposite the pump. In the example of Fig. III.3 the optimum length is 15.6 meters.

III.3 Amplified Spontaneous Emission

A pumped Er^{3+}-doped fiber continuously releases some of its stored energy in the form of amplified spontaneous emission. A uniformly-doped core section of pumped fiber, shown in Fig. III.4, with length dz, area $A = \pi r^2$ and N_2 ions/volume in the metastable level spontaneously

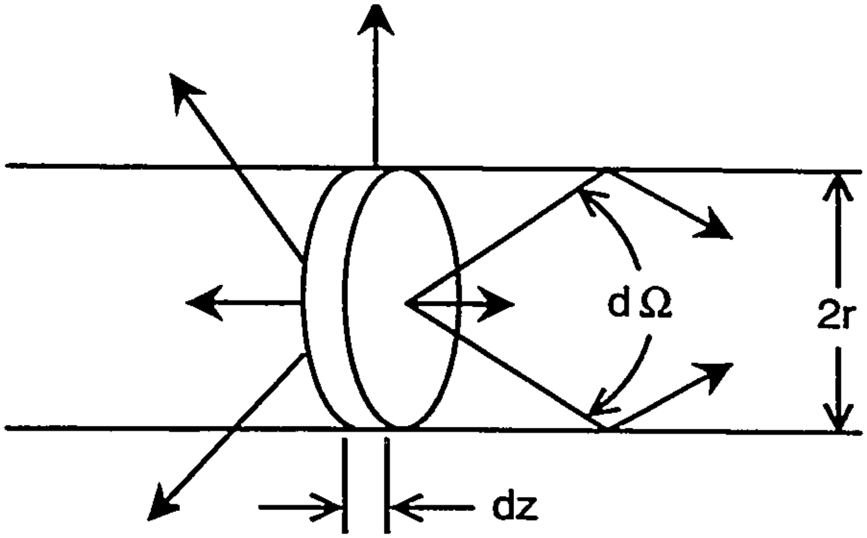

Fig. III.4. Isotropic spontaneous emission in pumped erbium doped fiber.

emits $N_2 g_e(\nu)\Delta\nu A dz/\tau$ photons per second within the bandwidth $\Delta\nu$, centered at ν. As shown, spontaneous emission occurs isotropically so only a fraction $d\Omega/4\pi$ of the photons are guided by the fiber, with numerical aperture NA, in either direction where the acceptance solid angle is given by:

$$d\Omega = \pi(NA)^2 \tag{47}$$

Using the gaussian beam approximation:

$$NA \approx \frac{\lambda}{n\pi r} \tag{48}$$

and (43) gives the guided spontaneous emission power added by the section per unit frequency:

$$\frac{dS_{SE}(\nu,z)}{dz}d\nu = 2N_2(z)\sigma_e(\nu)h\nu d\nu \tag{49}$$

$S_{SE}(\upsilon,z)$ is the spectral density of the spontaneous emission noise at frequency υ and position z. From (46),

$$\sigma_e(\nu) = \frac{\gamma(\nu)}{N_2 - N_1\varepsilon(\nu)} \tag{50}$$

where $\varepsilon(\nu) = \sigma_a(\nu)/\sigma_e(\nu)$. This gives

$$\frac{dS_{SE}(\nu,z)}{dz} = 2n_{sp}(\nu,z)\gamma(\nu)h\nu d\nu \tag{51}$$

The spontaneous emission factor, n_{sp}, is defined as:

$$n_{sp}(\nu,z) = \frac{N_2(z)}{N_2(z) - N_1(z)\varepsilon(\nu)} \tag{52}$$

The signal light and the ASE power from the other fiber sections propagates through the fiber section so the total power at frequency ν leaving the section is given by

$$dP_t(\nu,z+dz) = \gamma(\nu,z)\left[\, P_s(\nu,z) + S_{ASE}(\nu,z)d\nu + 2n_{sp}(\nu,z)h\nu d\nu \,\right] dz \tag{53}$$

The first term on the right of (53) gives the signal amplification, the second term gives the amplification of the spontaneous emission entering the fiber section and the third term gives the spontaneous radiation generated within the section. This differential equation is solved with the integrating factor $\exp\left[-\int_0^z \gamma(\nu,z')dz'\right]$ to give the total output power from a fiber length of L within a frequency band $d\upsilon$ centred at frequency ν :

$$\begin{aligned} P_t(\nu,L) &= G(\nu,L)h\nu\int_0^L \frac{N_2(z)\sigma_e(\nu)}{G(\nu,z)}dz + P_s(\nu,0)\,G(\nu,L) \\ &= S_{ASE}(\nu,L)d\nu + P_s(\nu,L) \end{aligned} \tag{54}$$

where the gain is given by

$$G(\nu,z) = \exp\left[\int_0^z \gamma(\nu,z')dz'\right] \tag{55}$$

By integrating over frequency one gets the total ASE output power:

$$P_{ASE}(L) = \int_0^\infty G(\nu,L)h\nu\int_0^L \frac{N_2(z)\sigma_e(\nu)}{G(\nu,z)}dz\, d\nu \tag{56}$$

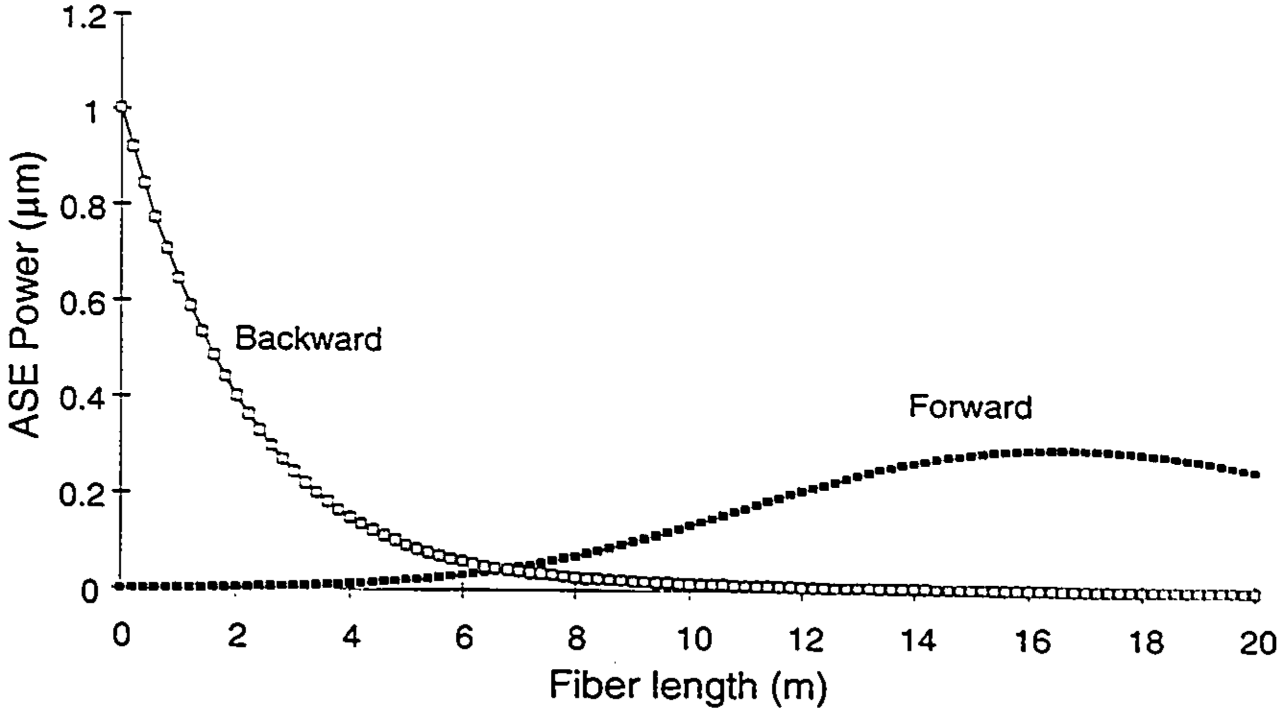

Fig. III.5. ASE in an erbium doped fiber vs length.

For the same example fiber as in Fig. III.3 the ASE powers in the forward and reverse directions are shown in Fig. III.5. As shown in this figure, forward pumping produces less ASE noise at the amplifier output. This result can be understood by examining the effect of reversing the order of integration in (54). Most of the reverse spontaneous emission is amplified in the fiber section near the pump input which has the largest population inversion and hence greatest amplification. Most of the forward spontaneous emission is not amplified in this section of the fiber and thus has a lower net amplification.

If the population inversion is constant along the fiber,

$$S_{ASE}(\nu,L) = 2n_{sp}(\nu,L)\big(G(\nu,L) - 1\big)h\nu \tag{57}$$

Thus, it is useful to define an integrated spontaneous emission factor [68], given by

$$\bar{n}_{sp}(\nu,L) = \frac{S_{ASE}(\nu,L)}{2\big[G(\nu,L) - 1\big]h\nu} \tag{58}$$

The dependence of n_{sp} on gain can be illustrated by its behaviour for the case of uniform population inversion. In this case

$$n_{sp}(\nu,L) = \frac{1}{1 + \varepsilon(\nu)} \left[\frac{G_{\max}^{dB}(\nu,L)}{G^{dB}(\nu,L)} + \varepsilon(\nu) \right] \tag{59}$$

where $G_{max}(\nu,L) = \exp(\Gamma N_t \sigma_s^e(\nu) L)$ is the maximum possible small signal gain and $\varepsilon(\nu) = \sigma_s^e(\nu)/\sigma_s^a(\nu)$. As the gain increases to its maximum value, nsp decreases from infinity to unity.

As indicated in (57), the spontaneous emission factor can be thought of as a proportionality factor betweeen the noise power and signal power. Therefore, the signal-to-noise ratio (SNR) is maximized when the gain is maximized. In physical terms, the energy stored by the pump in the doped fiber is released as either signal or noise, so that increasing the output signal power by increasing the input signal power results in less ASE noise being generated. Also, there is a minimum input signal power required to prevent the output signal power from being lower than the output ASE noise power. Spontaneous emission power and bandwidth also depend on the pump power. This is demonstrated in the experimental section, Section III.5. ASE is important because it can deplete the amplifier gain, especially for weak input signals. It also produces noise at the optical receiver. This is the subject of the next section.

III.4 Fiber Amplifier Signal-to-Noise Ratio

III.4.1 Derivation of Noise Terms

The EDFA signal-to-noise ratio (SNR) and the detection error of an EDFA preamplifier are now discussed. There are several methods of calculating the amplifier noise figure which yield similar results but vary in derivational accuracy. The output of the amplifier can be treated as a superposition of the signal and white Gaussian noise [61]. This method does not account for the ASE spectral shape and only includes shot noise as an afterthought. The master equation approximation calculates the noise figure for a two level system without considering the length dependence of n_{sp} [69]. The present approach, taken from quantum optics, examines the photon number statistics [70]. This method accounts for shot noise, the ASE spectral dependence, and can calculate the length dependence of the SNR. The detection error probability is found by calculating P(n), the probability of n photons arriving at the detector within the bit period, T.

For coherent light such as that from a laser far above threshold the average photon flux $P_s/h\nu$

is constant but the actual photon emission times are random. Assuming that photon emissions are independent, the photon emission is a Poisson process with the probability that n photons are emitted in time T given by [70]:

$$P(n) = \frac{\bar{n}_s^{\,n} e^{-\bar{n}_s}}{n!} \tag{60}$$

where $\bar{n}_s = PT/h\nu$ is the average number of photons in time T in the incident, coherent signal beam. The first two moments of this distirbution are $\langle n \rangle = \bar{n}_s$ and $\sigma_n^2 = \bar{n}_s$.

In contrast to coherent light, thermal or chaotic light such as that from the ASE noise from an EDFA does not emit photons at a constant average rate. In this case Mandel's Formula for conditional Poisson counting:

$$P(n) = \left\langle \frac{e^{-\mu}\mu^n}{n!} \right\rangle = \int_0^{\infty} \frac{e^{-\mu}\mu^n}{n!} P\{\mu\}\, d\mu \tag{61}$$

must be used to calculate the probability distribution. Here, the fluctuations in the mean photon number μ are described by the probability density funciton $P(\mu)$. An amplifier without an input signal emits ASE which can be resolved into two orthogonal phase components. The mean photon number distribution of the wideband ASE noise can therefore be approximated as the sum of two independent, squared, zero-mean, gaussian random variables with equal variances. The sum has an exponential or central χ_2^2 distribution [71]:

$$P(\mu) = \frac{1}{\langle \mu_{ASE} \rangle} \exp\left[-\frac{\mu}{\langle \mu_{ASE} \rangle} \right] \tag{62}$$

where μ_{ASE} is the mean number of ASE photons in time T. When substituted into (61), this gives

$$P(n) = \frac{\langle \mu_{ASE} \rangle^n}{\left(1 + \langle \mu_{ASE} \rangle\right)^{n+1}} \tag{63}$$

which is a geometric or Bose-Einstein distribution. Its first two moments are $\langle n \rangle = \langle \mu_{ASE} \rangle$ and $\sigma_n^2 = \langle \mu_{ASE} \rangle + \langle \mu_{ASE} \rangle^2$. This variance is greater than that of coherent light, indicating that it has a greater range of fluctuations of the photon number. For a fiber amplifier, the ASE noise is emitted in two orthogonal polarizations. The two components are independent random variables so that the net variance is $\sigma_n^2 = 2<\mu_{ASE}> + 2<\mu_{ASE}>^2$ where $<\mu_{ASE}>$ is the mean number of ASE photons in one polarization.

The output noise of an amplifier with an input signal is now examined. The amplified signal and ASE from an EDFA can be treated as a polarized superposition of thermal and coherent light. In this case the intensity is a sum of two independent, squared, non-zero mean, gaussian random variables with equal variances, with mean photon number distribution [71]:

$$P(\mu) = \frac{1}{\langle\mu_{ASE}\rangle}\exp\left(-\frac{\mu + \bar{n}_s}{\langle\mu_{ASE}\rangle}\right)I_0\left[\frac{2\sqrt{\bar{n}_s\mu}}{\langle\mu_{ASE}\rangle}\right] \tag{64}$$

where I_0 is the modified Bessel function. This is a Rician square or non-central χ_2^2 distribution. Its first two moments are $<\mu> = <\mu_{ASE}> + \bar{n}_s$ and $\sigma_\mu^2 = <\mu_{ASE}>^2 + 2\bar{n}_s<\mu_{ASE}>$. Substituting this into (61) gives

$$P(n) = \frac{\langle\mu_{ASE}\rangle}{\left(1 + \langle\mu_{ASE}\rangle\right)^{n+1}}\exp\left(-\frac{\bar{n}_s}{1 + \langle\mu_{ASE}\rangle}\right)L_n\left(-\frac{\bar{n}_s/\langle\mu_{ASE}\rangle}{1 + \langle\mu_{ASE}\rangle}\right) \tag{65}$$

which has moments $<n> = \bar{n} + <\mu_{ASE}>$ and $\sigma_n^2 = \bar{n}_s + <\mu_{ASE}> + <\mu_{ASE}>^2 + 2\bar{n}_s<\mu_{ASE}>$. The unpolarized ASE noise is equally divided between two independent polarization components, parallel and orthogonal to the signal. The component orthogonal to the signal does not interfere with the signal and thus has the variance of the geometric distribution. The net variance is thus given by

$$\begin{aligned} \sigma_n^2 &= \bar{n}_s + 2\langle\mu_{ASE}\rangle + 2\langle\mu_{ASE}\rangle^2 + 2\bar{n}_s\langle\mu_{ASE}\rangle \\ &= \sigma_{sig-sh}^2 + \sigma_{sp-sh}^2 + \sigma_{sp-sp}^2 + \sigma_{sig-sp}^2 \end{aligned} \tag{66}$$

where $<\mu_{ASE}>$ is the mean number of noise photons in one polarization. The four terms in (66) from left to right are attributed to signal shot noise, ASE shot noise, spontaneous-spontaneous beat noise and signal-spontaneous beat noise. From the previous section $<\mu_{ASE}>$ is calculated by integrating the ASE noise spectral density over the amplifier bandwidth. We assume that the ASE is equally divided between the two polarization so that the noise terms are given by

$$\begin{aligned}
\sigma^2_{sig-sh} &= \frac{TP_s^{in}G_{net}}{h\nu_s} \\
\sigma^2_{sp-sh} &= 2T\eta_o\int\frac{S_{ASE}(\nu)}{2h\nu}d\nu = 2T\eta_o\hat{n}_{sp}(\hat{G}-1)\Delta\nu_{ASE} \\
\sigma^2_{sp-sp} &= 2T\eta_o^2\int\left[\frac{S_{ASE}(\nu)}{2h\nu}\right]^2 d\nu = 2T\eta_o^2\hat{n}_{sp}^2(\hat{G}-1)^2\Delta\nu_{sp-sp} \\
\sigma^2_{sig-sp} &= \frac{2T\eta_o P_s^{in}G_{net}}{h\nu_s}\int\frac{S_{ASE}(\nu)\delta(\nu-\nu_s)}{2h\nu_s}d\nu = 2T\eta_o\bar{n}_{sp}(\nu_s)(G(\nu_s)-1)\frac{P_s^{in}G_{net}}{h\nu_s}
\end{aligned} \tag{67}$$

In these equations the net gain at the signal wavelength, G_{net}, is $\eta_i\eta_o G$ where η_i and η_o are the amplifier input and output coupling efficiencies, P_s^{in} is the signal input power, $\hat{n}_{sp}$ is the integrated spontaneous emission factor at the peak of the ASE spectral distribution, $\hat{G}$ is the gain at the peak of the ASE spectral distribution, the ASE bandwidth is given by

$$\Delta\nu_{ASE} = \frac{\int_0^\infty S_{ASE}(\nu)d\nu}{\hat{S}_{ASE}} \tag{68}$$

where $\hat{S}_{ASE}$ is the peak value of $S_{ASE}(\nu)$, and the spontaneous-spontaneous beat noise bandwidth is given by [68]:

$$\Delta\nu_{sp-sp} = \int\frac{S_{ASE}^2\,d\nu}{\hat{S}_{ASE}^2} \tag{69}$$

III.4.2 Amplifier Noise Figure

The EDFA noise figure is defined as the ratio of the input SNR to the output SNR:

$$NF = \frac{\text{Input SNR}}{\text{Output SNR}} = \frac{\sigma^2_{out}}{\sigma^2_{in}G^2_{net}} \tag{70}$$

where σ_{in}^2 and σ_{out}^2 are the net input and output variances [72]. The input light at the amplifier, assumed coherent, has a SNR given by:

$$\text{Input SNR} = \frac{\langle n \rangle}{\sigma_n^2} = \frac{P_s^{in} T}{h\nu} \tag{71}$$

From (66)-(71) the amplifier noise figure is thus given by:

$$\begin{aligned} NF &= \frac{1}{G_{net}} + \frac{1}{P_s^{in}\eta_i G^2}\int S_{ASE}(\nu)d\nu + \frac{1}{2P_s^{in}\eta_i^2 G^2}\int\frac{S_{ASE}^2(\nu)}{h\nu}d\nu + \frac{S_{ASE}(\nu_s)}{\eta_i G h\nu} \\ &= \frac{1}{G_{net}} + \frac{2n_{sp}' h\nu\Delta\nu_{ASE}}{\eta_i G_{net} P_s} + \frac{2\left(n_{sp}'\right)^2}{\eta_i}\Delta\nu_{sp-sp}\frac{h\nu}{\eta_i P_s} + \frac{2\bar{n}_{sp}(\nu_s)}{\eta_i}\left[\frac{G-1}{G}\right] \end{aligned} \tag{72}$$

where

$$n_{sp}' = \hat{n}_{sp}\left[\frac{\hat{G} - 1}{G(\nu_s)}\right] \tag{73}$$

For the sample fiber of Figs. III.3 and III.5, the relative values of the four noise terms are shown in Fig. III.6 for an optical bandwidth of 5 nm.

Signal-spontaneous beat noise is typically dominant with a high input power and spontaneous-spontaneous beat noise is dominant with a low input power. The spontaneous-spontaneous beat noise and spontaneous shot noise are proportional to the optical bandwidth. Hence, these noises may be reduced by inserting an optical notch filter after the optical amplifier as shown in Fig. I.2. Typically, an interference film and/or fiber Fabry-Perot filter is used [60]. The minimum possible bandwidth of the optical filter is determined from the laser linewidth, data rate, and transmission format, as well as the long term stability of the laser wavelength. Signal-spontaneous beat noise is the dominant noise when the output signal power is greater than the output ASE power which occurs when the received number of photons per bit is greater than the ratio of the optical bandwidth to the bit rate.

In the signal-spontaneous beat noise limited regime, with high gain and negligible coupling losses, the noise figure of the optical preamplifier approaches a theoretical limit of [72]:

$$NF_{opt} = \frac{\sigma_{sig-sp}^2}{\sigma_{sig-sh}^2(in)\; G^2} = 2n_{sp}' \tag{74}$$

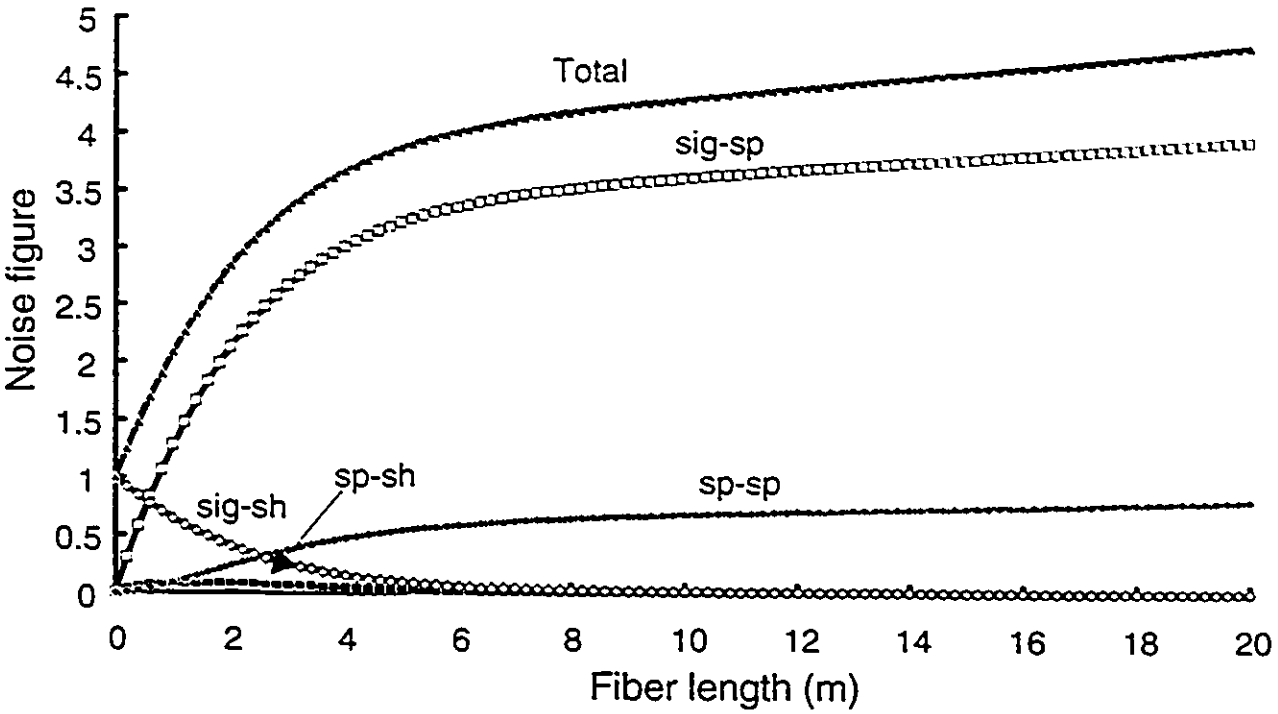

Fig. III.6. Relative values of EDFA noise terms.

Since $n_{sp} \geq 1$, an EDFA has a minimum noise figure of 3 dB. This is derived by assuming that the input signal is shot noise limited and the output noise is signal-spontaneous beat noise limited. The noise figure is directly proportional to the amplifier input coupling efficiency which is typically greater than -1 dB for an EDFA, but less than -3 dB for a semiconductor optical amplifier.

The purpose of an optical preamplifier is to raise the signal level above the detector circuit noise. The circuit noise is included in the calculations by adding the detector noise term $(\sigma_c/\eta_q e)^2 T$ to the variance where σ_c^2 is the detector noise density, e is the electron charge and η_q is the detector quantum efficiency. Fig. III.7 shows, for the amplifier in Figs. III. 3, III.5, and III.6, the evolution of the inverse noise figure (proportional to the output SNR), calculated by neglecting the detector circuit noise and by including a typical detector noise density of 10^{-22} A^2/Hz [73]. When detector noise is not considered, the amplifier function is not obvious since it reduces the SNR. However, when the circuit noise is considered, one sees that amplifier increases the SNR at the receiver by about 20 dB.

A comparison of Figs. III.7 and III.3 shows that the fiber length that maximizes the amplifier SNR, 9.6 meters, is shorter than the length that optimizes the gain, 15.4 meters. At the end of an

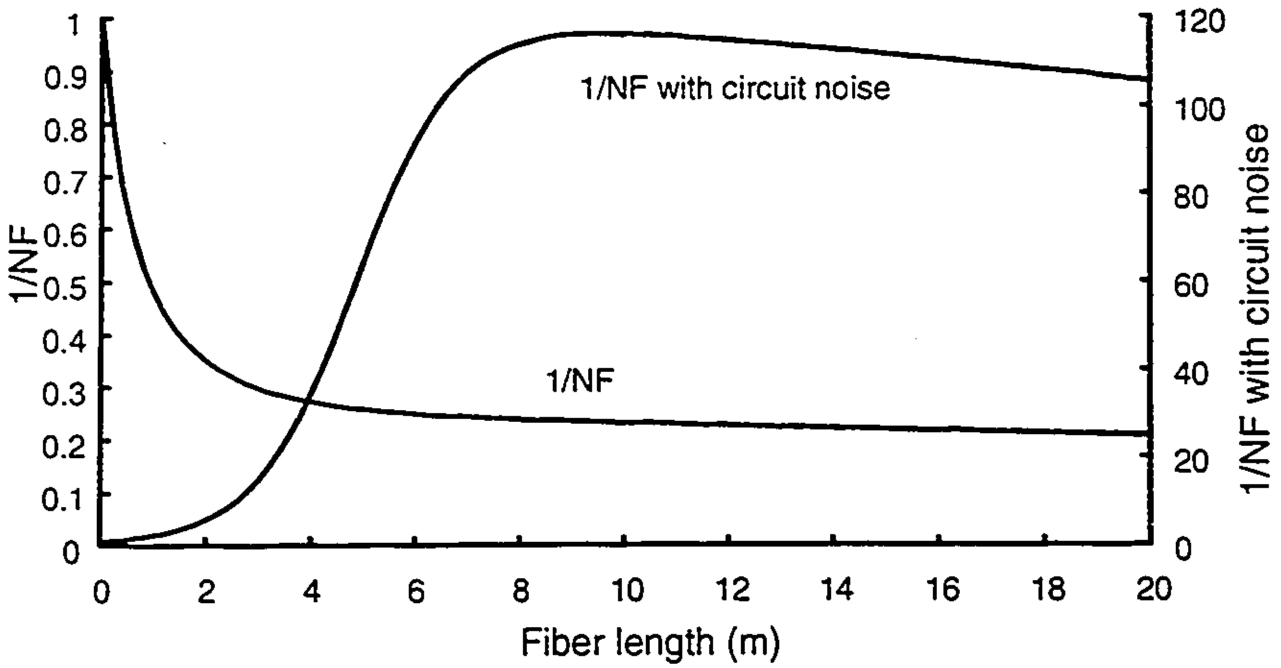

Fig. III.7. Inverse EDFA noise figure including detector noise.

EDFA that maximizes the gain, the differential gain is zero while noise is still being added so the length that maximizes the SNR is always shorter than the length that maximizes the gain. However, Fig. III.7 indicates that the noise degradation is not severe since the noise figure is almost constant for lengths greater than 8 m. Taking the derivative of the SNR with fiber length gives a formula for the length that maximizes SNR. If the signal-spontaneous beat noise is assumed dominant then the optimum length satisfies:

$$n_{sp}(\nu_s,L)P_s(L) = \left(\frac{\sigma_c}{\eta_q e}\right)^2 h\nu \qquad (75)$$

This is the first expression that gives an analytical approximation for the fiber length optimizing the SNR at the receiver. It can be used with the two-level EDFA model in Chapter II to find the optimum length as follows. First, the powers along the amplifier $P_p(z)$ and $P_s(z)$ can be found from (17) and (18). These are substituted into (21) to obtain $\gamma(z,\nu_s)$. This is substituted into [53]:

$$N_2(L) = \frac{P_s^{IS}\tau}{A_{eff}}\left[\gamma(\nu_s,L) + \alpha_s\right] \qquad (76)$$

to get $N_2(z)$, which is then substituted into (52) to give $n_{sp}(\nu_s,z)$. Then the point along the fiber is found where $n_{sp}(\nu_s,z)P_s(z)$ equals the right-hand side of (75). If the effect of spontaneous-spontaneous beat noise is included in the derivation of optimum length, an expression results for the optimum length that must be solved numerically. For our example, (75) estimates the optimum amplifier length at 9.3 meters which is very close to 9.6 meters, the value found by the exact solution.

To calculate the bit error probability at the receiver, the error probability when a "1" is received is calculated differently than when a "0" is received since when no signal is present, signal shot noise and signal-spontaneous beat noise are not present. Typically the ASE power is assumed equal for the two cases even though it depends on the signal power. Neglecting the detector noise yields

$$P(e|\text{OFF sent}) = \sum_{n=\phi+1}^{\infty} \frac{\langle\mu_{ASE}\rangle^n}{\left(1+\langle\mu_{ASE}\rangle\right)^{n+1}} = \left(\frac{\langle\mu_{ASE}\rangle}{1+\langle\mu_{ASE}\rangle}\right)^{\phi+1} \tag{77}$$

and

$$P(e|\text{ON sent}) = \sum_{n=0}^{\phi} \frac{\langle\mu_{ASE}\rangle}{\left(1+\mu_{ASE}\right)^{n+1}} \exp\left(-\frac{\bar{n}_s}{1+\langle\mu_{ASE}\rangle}\right) L_n\left(-\frac{\bar{n}_s/\langle\mu_{ASE}\rangle}{1+\langle\mu_{ASE}\rangle}\right) \tag{78}$$

where ϕ is the decision threshold. These expressions may be generalized by including the detector noise [71] and simplified with a Gaussian approximation [74]. Note that, since the ASE power level depends on the input signal power, $<\mu_{ASE}>$ depends on the signal level. Optical preamplifier receiver error probabilities have been studied by various researchers and will not be discussed further [61], [69], [71], [74].

III.5 Experiments

The top of Fig. III.8 shows the ASE spectrum of the 7 meter EDFA described in Section II.6 for different pump powers. The ASE and spontaneous-spontaneous bandwidths, calculated from Eqs. (59) and (69) respectively, are shown in the bottom of Fig. III.8. As mentioned above, the noise bandwidth decreases as the gain increases. The top of Fig. III.9 shows the EDFA output spectra with a -20 dBm input signal at 1542 nm. The input signal reduces the output ASE noise, as more amplifier energy is transferred to the signal. The bottom of Fig. III.9 shows how an optical bandpass filter after the amplifier changes the spectrum. A tunable dielectric bandpass filter with a 3 dB

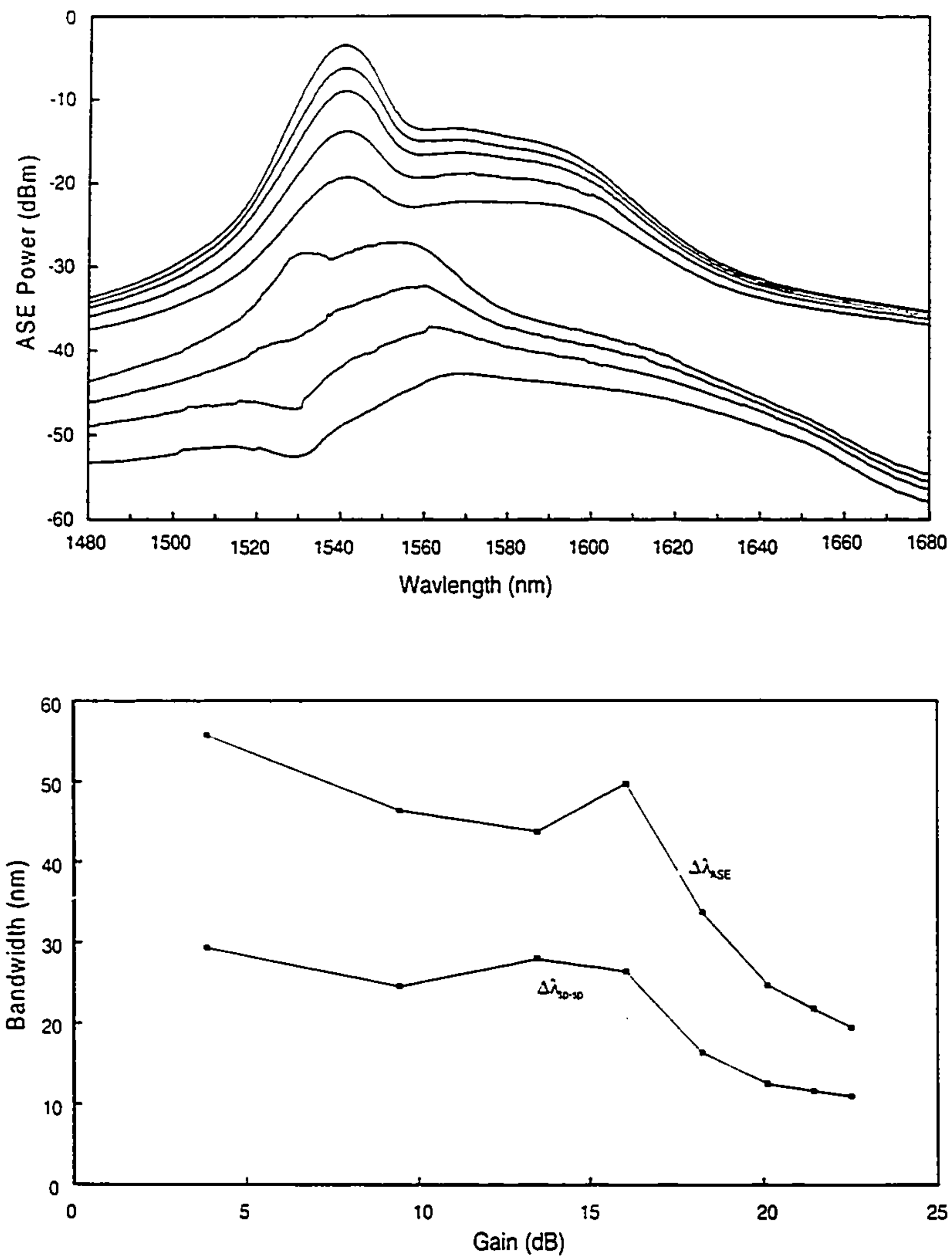

Fig. III.8. For a 7 m EDFA. Top: Measured ASE spectra for 980 nm pump power of 2,3,4,6,8,11,13, and 16 mW (increasing from the bottom); Bottom: Bandwidths for 16 mW pump power.

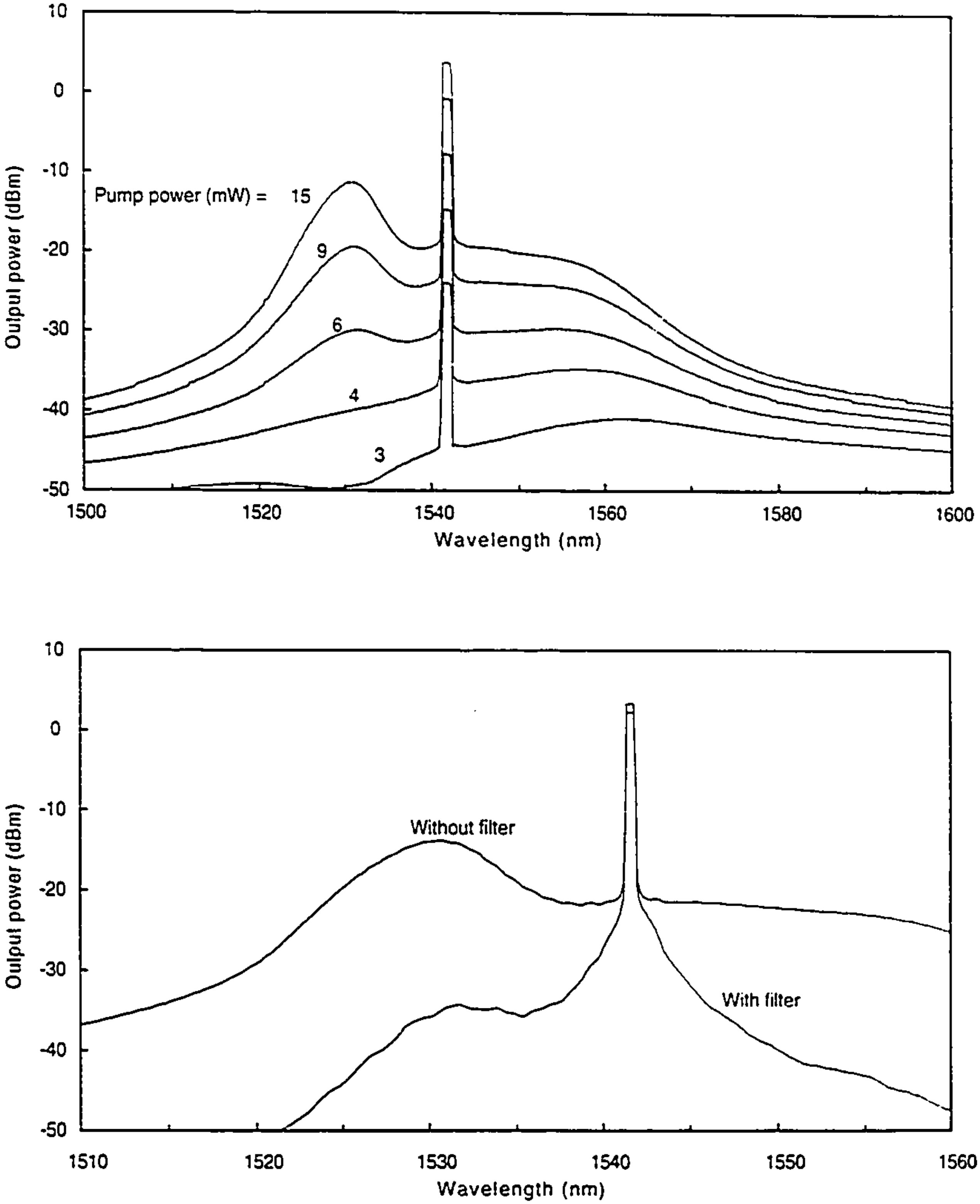

Fig. III.9 EDFA spectra with input signal, (top) as a function of pumping power and (bottom) after optical filtering.

bandwidth of about 2 nm was inserted after the amplifier and tuned to the signal wavelength. The output power is decreased by about 1 dB by the filter insertion loss, and the ASE level is decreased by about 25 dB. This shows how optical filtering can reduce the ASE noise at the receiver.

III.6 Summary

In this chapter, expressions are given for the ASE power of an EDFA, its bandwidth, and the spontaneous emission factor. As the gain increases, n_{sp} decreases to unity, the ASE bandwidth decreases, and the noise figure approaches 3 dB. Because of ASE, the EDFA preamplifier fiber length that optimizes the receiver SNR is significantly shorter than the length that optimizes the amplifier gain. However, since the SNR is insensitive to the fiber length, the gain maximizing length has a SNR only slightly lower than the optimum. Optical filtering can greatly reduce the ASE power, resulting in signal-spontaneous beat noise limited detection. In this limit, a simple expression is given for the optimum fiber length. The receiver error probability depends on the signal power, receiver noise, ASE noise power and bandwidth, and bit rate.

Chapter IV

EDFA Transient Response and Remote Gain Switching

IV.1 Introduction

In this chapter time-dependence is incorporated in the EDFA model to study the effect of rapidly saturating the amplifier gain with high-power optical pulses within the amplifier bandwidth. Preliminary experiments in our laboratory demonstrated that high-power nanosecond optical pulses can deplete the EDFA gain by over 20 dB within the nanosecond pulse duration. This result is contrary to intuitive expectations in that the amplifier response is not limited by its millisecond upper-level decay time. The study of this phenomenom is useful for two reasons. First, it improves our understanding of EDFA gain dynamics. This is important for WDM applications where variations in a strong signal can cause fluctuations in weaker signals. The gain depletion also has potential application as an all-optical switch.

All-optical EDFA switching eliminates lossy, bandwidth-limited optical/electronic conversion while incorporating the switching and gain functions in a single element. Another advantage is that switching can be controlled remotely at great distances since the switching is initiated by 1.55 µm optical pulses. Nanosecond EDFA switching has many potential applications such as filtering WDM signals, multiplexing and demultiplexing TDM signals, packet switching, network routing, and network testing. Both SOA and EDFA based switches can have an extremely high dynamic range since strong gain in a pumped amplifier becomes strong absorption in an unpumped amplifier. One advantage of the SOA over the EDFA is its fast switching. By modulating the SOA bias current, nanosecond gain switching has been demonstrated [75].

It was previously thought that similar fast switching of EDFA's was impossible due to the millisecond spontaneous decay time of the Er^{3+} ion metastable level. Therefore, suggested uses of the EDFA as an all-optical switching element have been limited to applications requiring slow or 'static' switching such as a 1.55 µm filter for multiplexed 1.3/1.55 µm signals. This technique uses pump power modulation to provide switching. In this case the ON switching time from absorption to amplification is limited by the pump rise time, pump power, and the non-radiative decay time of the ion from the pump level to the metastable level. For pump wavelengths other than 1480 nm, the non-radiative phonon decay from the pump level to the metastable level is limited by the $^4I_{11/2}$-$^4I_{13/2}$ transition which is about 7 μs (Fig. III.1) [76]. Short, intense pump pulses are most readily available from the second harmonic of a Q-switched Nd:YAG laser (532 nm). Thus the present possible pump ON-switching time is ≈ 7 μs, with a physical limit of less than 1 ns for 1.48 μm pumping. When the pump laser is turned off, the ions in the metastable energy level decay to the ground state by spontaneous emission with a time constant of ≈ 10 ms. Fast OFF switching thus requires an alternative to pump switching.

It has been suggested that OFF switching could be achieved by saturating the amplifier with light within the gain bandwidth using optical feedback [77]. Zirngibl demonstrated 26 dB small signal gain compression in an EDFA with an optical feedback loop operating at the saturating wavelength. Applying the saturating signal initialized lasing in the fiber amplifier through the optical feedback loop with a build-up time of 10-50 ms. Measurements of the multichannel small-signal gain saturation showed characteristic saturation and recovery times of 0.1-1 ms [78]. Recent experiments in our laboratory showed that a single pass through the amplifier by a short pulse within the amplifier gain bandwidth can rapidly saturate the amplifier, causing over 20 dB gain suppression with a 30 ns switching time [79]. A rapid increase in the rate of stimulated emission near (but not at) the signal wavelength reduces the population inversion sufficiently to cause high-speed gain compression in the amplifier. This is essentially an extreme case of cross-talk in which the energy supplied by the switching pulse depletes the pumped or stored energy of the amplifier orders of magnitude more quickly than those mechanisms suggested to date. It was found that increasing the pulse power increased the gain compression and decreasing the pulse duration decreased the switching time. Since the switching mechanism is stimulated emission, it is limited only by the rise time of the saturating pulse and not by the long spontaneous emission lifetime.

To date, saturating pulse switching has not been accurately modelled theoretically. An analytical solution of transient gain saturation exists [81], but it only gives the change in population inversion at the fiber input end. In this chapter the first model that simulates fast EDFA switching with pump and signal pulses is presented. After comparing theoretical and experimental results, the dependence of saturation OFF switching on factors such as pump and signal power; fiber length; and pulse energy and duration is studied. Switching is then described in terms of the effect of the saturating pulse on the energy stored in the erbium fiber. The conditions for optimum switching and the required minimum switching pulse energy are then determined. Fast ON switching using pump pulses is also investigated. The theory predicts that with a short, high-energy pump pulse, fast ON switching is possible, with switching times limited only by the pump level lifetime.

The practicality of remotely switching is then experimentally and theoretically investigated. Remote all-optical switching of signals from a mode-locked erbium-doped fiber laser is then demonstrated over fibers up to 50 km long.

IV.2 Initial Experiments

In the experiments a 25.5 m long EDFA was pumped with ≈40 mW at 980 nm using a Ti:Sapphire laser [81]. The gain was 30 dB using a 5 μW input signal from a 1540 nm DFB laser diode, modulated at 180 MHz. Saturating pulses were generated by a 350 Hz Q-switched erbium-doped fiber laser with peak pulse power ≈ 1 W and pulse duration of 10-150 ns [34]. The measured gain compression vs pulse energy is shown in Fig. IV.1 for 40 and 150 ns pulses. Observed switching times were slightly less than the pulse FWHM. After switching, the gain recovered to its

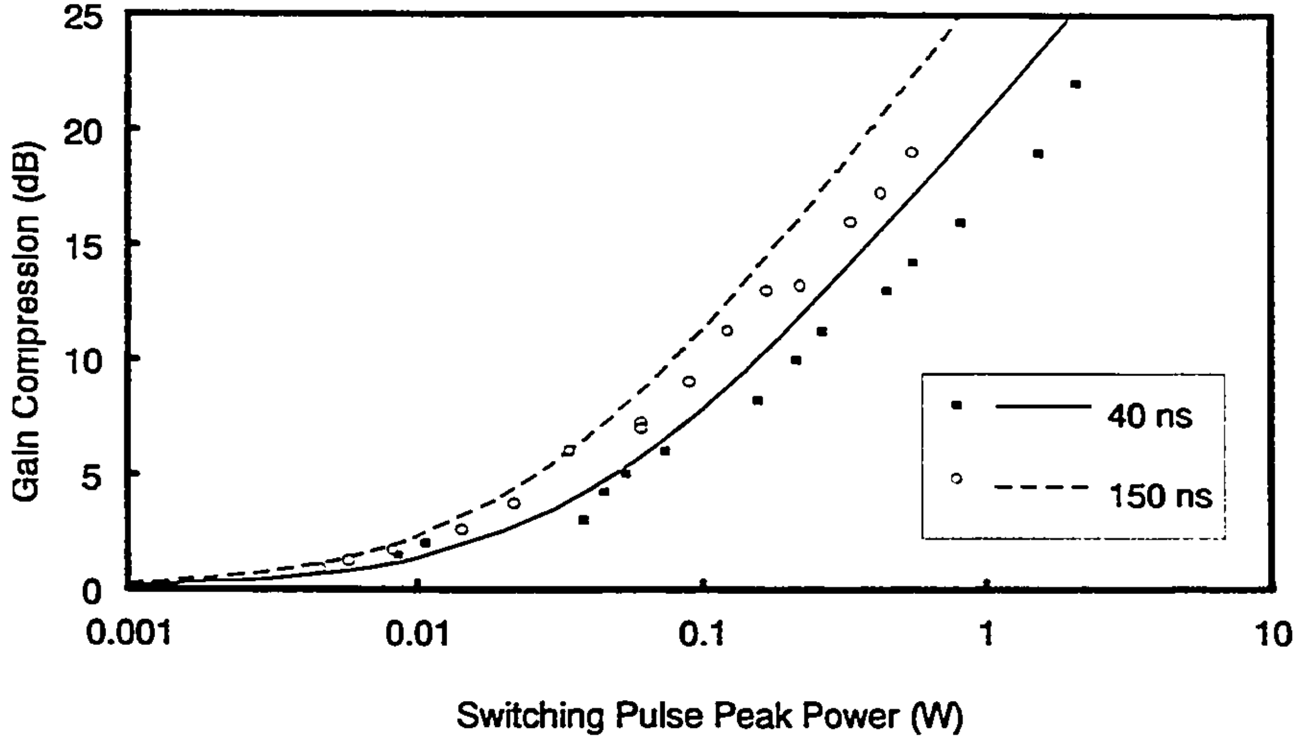

Fig. IV.1. Experimental and theoretical gain compression for 5 μW input signal at 1540 nm.

original value in 3 ms with 30 mW pumping, and in 1 ms with 45 mW pumping.

IV.3 Transient Theory Applied to EDFA Switching

EDFA dynamic behaviour is modeled with four differential equations describing the pump, signal, and pulse evolution along the fiber and population inversion change with time, assuming a two-level system [78] (see Section II.3.1). The equations are integrated by the fourth order Runge-Kutta method using alternating spatial and temporal steps. Initial CW conditions are derived using a full spectral model to account for the amplified spontaneous emission (ASE) in both directions [63]. The model uses experimentally determined absorption coefficients and intrinsic saturation powers at the three input wavelengths and published absorption and emission cross-sections for the ASE calculations [47]. The theory predicts 33 dB CW gain for a 5 μW signal at the DFB wavelength (1540 nm). All simulations are done for 30 mW pump power at the doped fiber input. Measured gain was lower (30 dB for a 40 mW pump) due to coupling losses and fiber imperfections, indicated by variations in measured absorption coefficients for different fiber sections.

Time dependence of signal and pulse power at the output is determined by integrating the

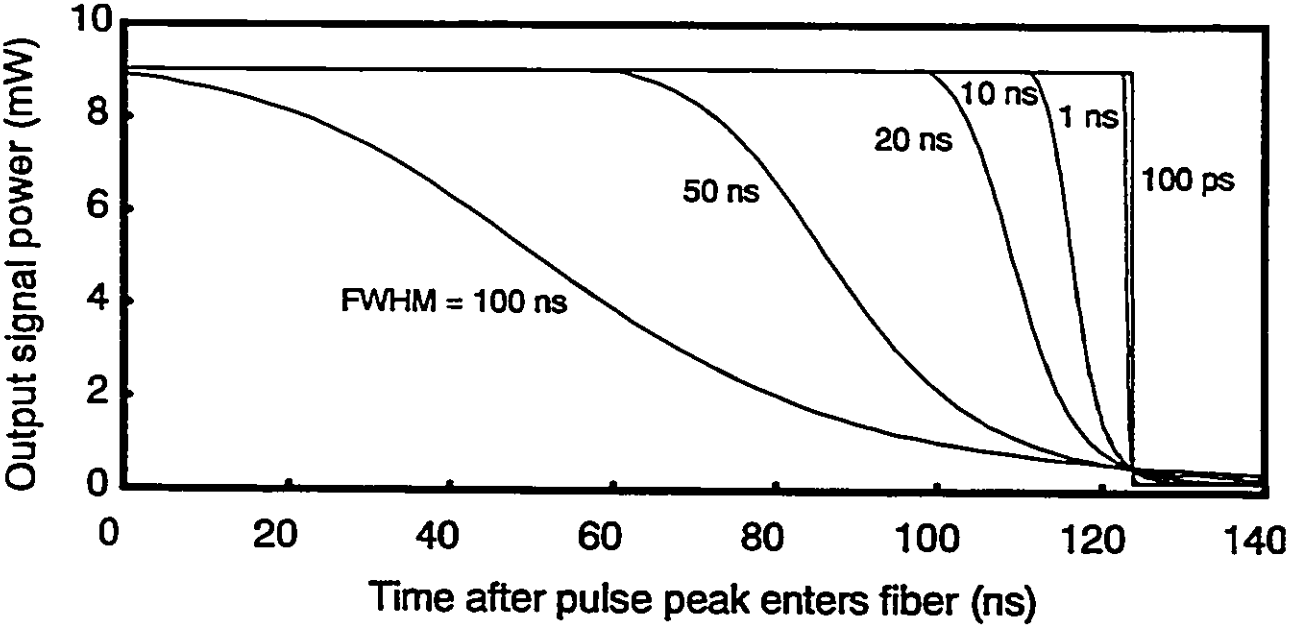

Fig. IV.2. Theoretical output signal vs time for different 20 μJ pulse durations. Pump power is 30 mW, signal power is 5 μW, gain is 33 dB, and gain compression is 16 dB.

equations, neglecting ASE during switching. Fig. IV.1 shows predicted and measured gain compression for 40 ns and 150 ns gaussian pulses. Slight differences with experiment can be due to fiber defects and approximate estimates of: fiber parameters, coupling losses, and cross-sections. The change in output signal with time is shown in Fig. IV.2 for 20 nJ pulses with duration of 100 ps to 100 ns. The time coordinate begins when the pulse peak enters the fiber. (Transit time through the 25.5 m fiber is 124 ns.) In all cases the 10%-90% switching time is approximately equal to the pulse duration, as observed experimentally. Since the gain compression (16 dB) does not vary with pulse duration the gain compression for the same initial conditions is determined by the input pulse energy, regardless of pulse duration or peak power. This dependence of switching time on pulse duration, pump power, and signal power is shown in Fig. IV.3. This figure shows that 10%-90% switching time is about equal to the pulse FWHM, regardless of pulse energy, or pump and signal power. The total time from when the pulse enters the amplifier to 90% gain compression is about equal to the transit time of the pulse in the fiber. The switch latency can be reduced by using a shorter, highly

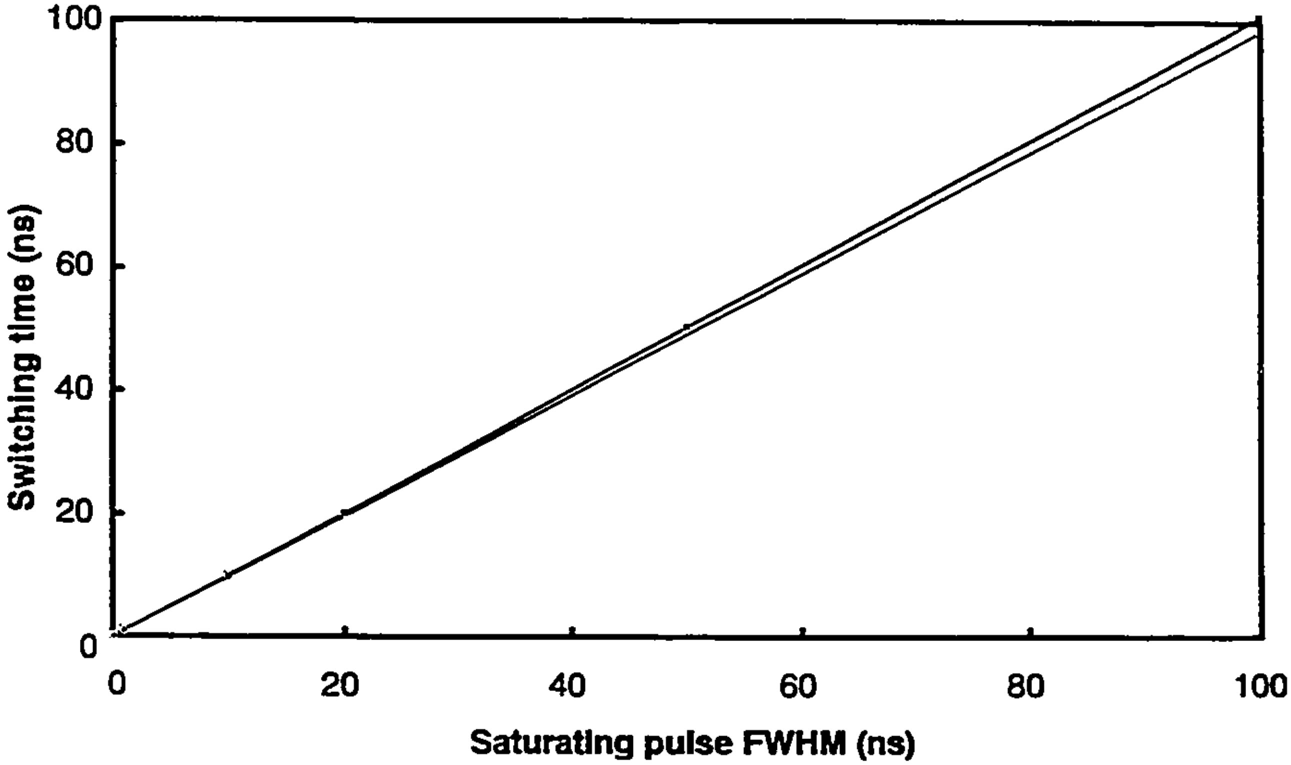

Fig. IV.3. Dependence of 10%-90% switching times on pulse width. Pump and signal powers are: 30 mw/5μW, 45 mW/5μW, and 30 mW/1μW.

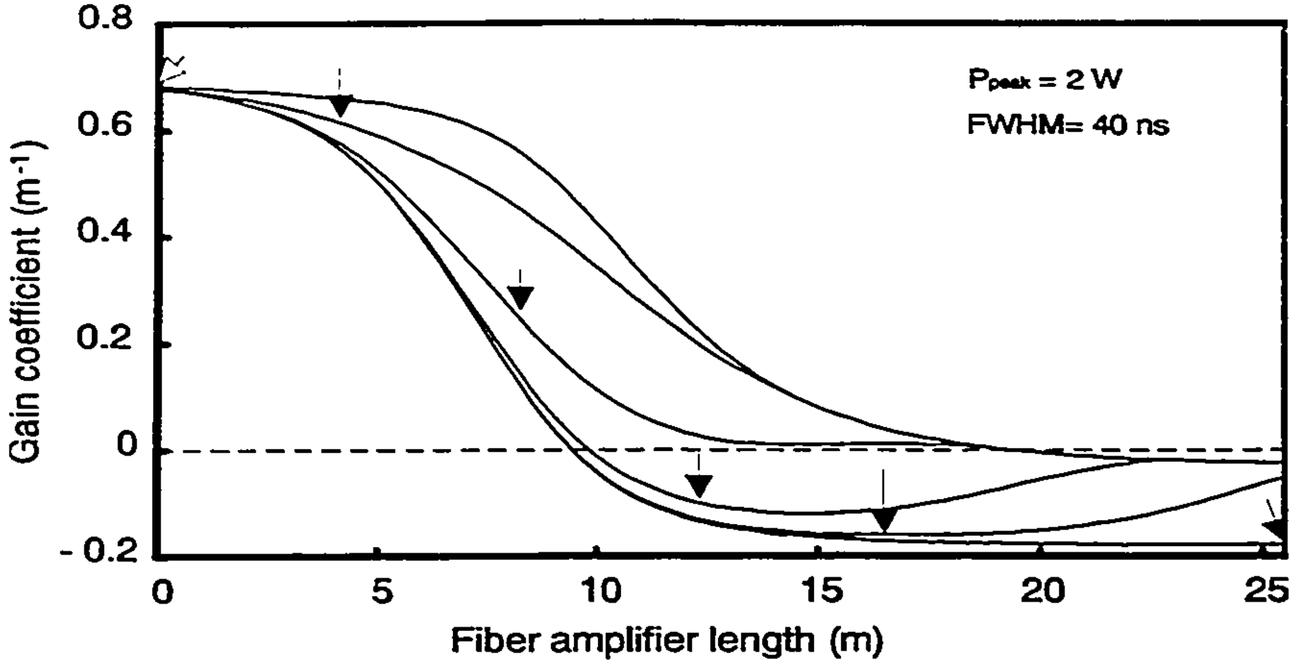

Fig. IV.4. Gain coefficient along the 25.5 m erbium fiber during switching. Arrows indicate the position of the pulse peak in time for each curve.

doped erbium fiber. Figures IV.2 and IV.3 indicate that sub-nanosecond EDFA gain compression is possible, with a delay equal to the propagation time in the doped fiber.

In order to improve our physical understanding of the amplifier switching and recovery dynamics, we simulated the change in the gain coefficient and the stored energy. The signal gain coefficient along the fiber is shown in Fig. IV.4 for different times after a 2 W/40 ns pulse enters the fiber. Arrows indicate the different pulse peak position for each curve. At the output end, the gain coefficient is constant along the fiber, indicating that the pulse is saturated. Population inversion depletion and gain coefficient reduction is much higher near the fiber output end than near the input end because of the large amplification of the pulse.

Gain compression occurs because the pulse extracts energy stored in the doped fiber. The energy stored in the EDFA vs time after the pulse peak enters the fiber is shown in Fig. IV.5 for two switching pulse powers. Stored energy is defined here as the total number of ions in the metastable level multiplied by the signal photon energy. The right y-axis indicates how the gain depends on stored energy. Transparency at the signal wavelength requires 78.5 μJ stored energy, large because of the three-level nature of erbium ions. In both cases the energy extracted equals the output pulse

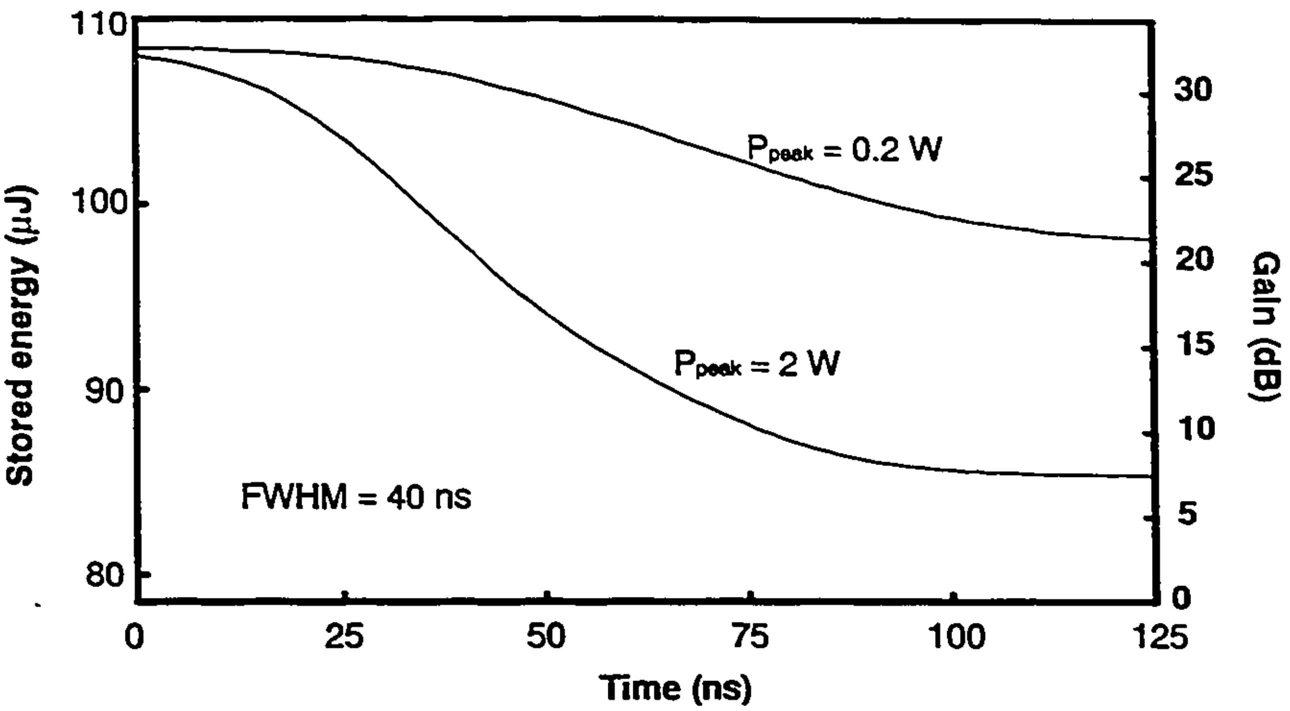

Fig. IV.5. Energy stored in the fiber during switching. Pump power is 30 mW, signal power is 5 μW, gain is 33 dB, and gain compression is 11 dB and 25 dB for 0.2 W and 2 W pulses, respectively.

energy which is 10.5 μJ for a 0.2 W input pulse and 23.5 μJ for a 2 W input pulse. This is explained by the fact that the energy of the system is conserved and the amount of energy delivered or extracted by the pump and signal beams during switching (40 ns) is negligible (few nJ). As shown in Fig. IV.6, the output pulse shape is skewed towards the front since the pulse front experiences a larger gain and the pulse rear is absorbed as it approaches the output end. The output pulse peak appears after 100 ns even though the fiber transit time is 125 ns.

Due to the fixed wavelength of the DFB laser at 1540 nm, switching was far from optimized. We now discuss how the required switching pulse energy can be minimized by adjusting the amplifier length and signal and pulse wavelengths. By varying the fiber length we found that maximum gain compression occurs at the length which maximizes the switching pulse gain. For this length the pulse small-signal gain coefficient is zero at the fiber output end. Figure IV.7 shows the theoretical amplifier small signal gain, gain saturation, and pulse amplification vs the fiber length for a 1 W/40 ns saturating pulse. The depression in the gain compression curve at short fiber lengths indicates that amplification of the pulse at the beginning of the fiber enhances the gain compression.

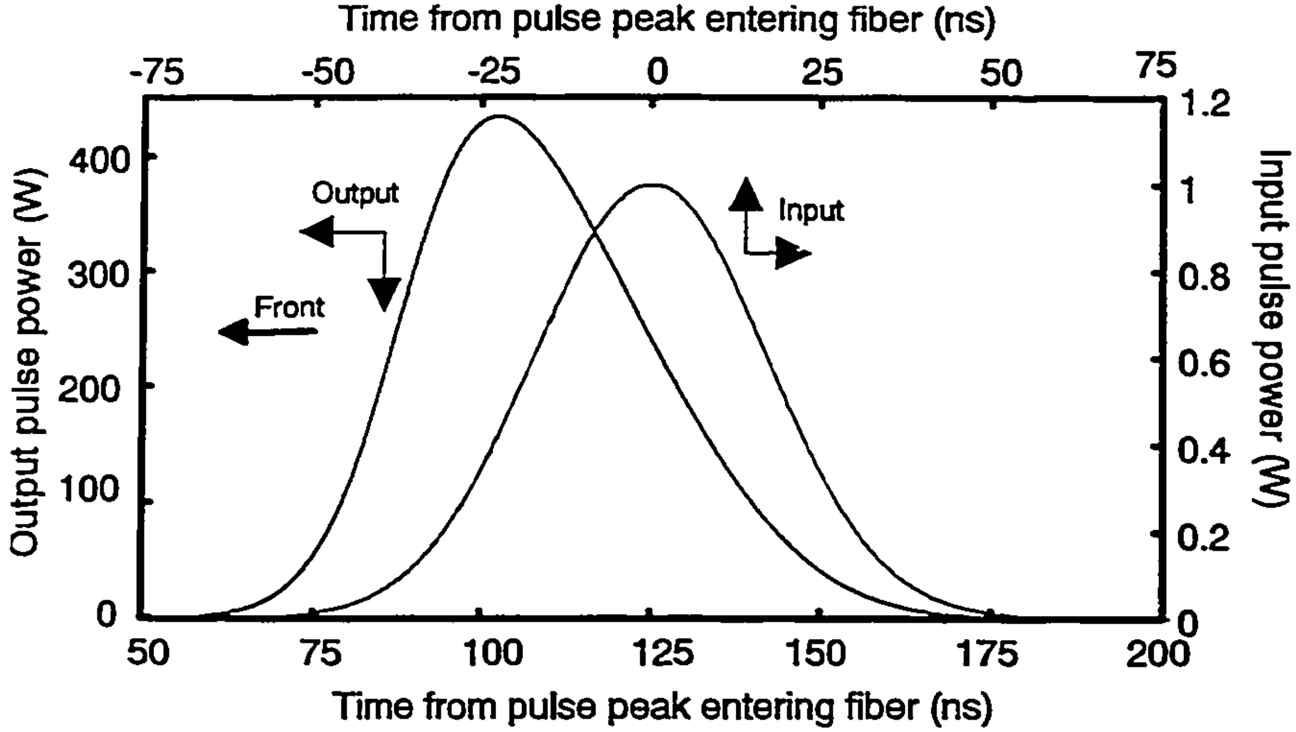

Fig. IV.6. Input and output pulse shapes for a 1 W/40 ns saturating pulse. Pump power is 30 mW, signal power is 5 μW, gain is 33 dB, and gain compression is 20 dB.

This is also indicated by the fact that gain compression is maximized at the point where the pulse gain is maximum.

We found that gain compression also depends strongly on the signal and pulse wavelengths. Switching is optimised when the pulse wavelength is at the small-signal gain spectrum peak which is 1530 nm for our fiber. Switching is most efficient for signal wavelengths below 1530 nm. Although in this spectral region the absorption cross-section is greater than the emission cross-section, the signal is amplified with sufficient population inversion. Very strong signal absorption occurs when the population inversion falls below the transparency level because of the larger absorption cross-section. Gain compression vs pulse energy is shown in Fig. IV.8 for a 1520 nm signal and a 1530 nm pulse for different pump and signal powers. As indicated, gain compression generally increases as pump power increases and input signal power decreases (remaining above ASE noise level). The optimum length is found by an iterative procedure for each initial condition. For each initial state, curves were derived using 100, 10, 1, and 0.1 ns pulses. These curves overlapped, indicating that gain switching for given initial conditions depends on pulse energy only. Fig. IV.8

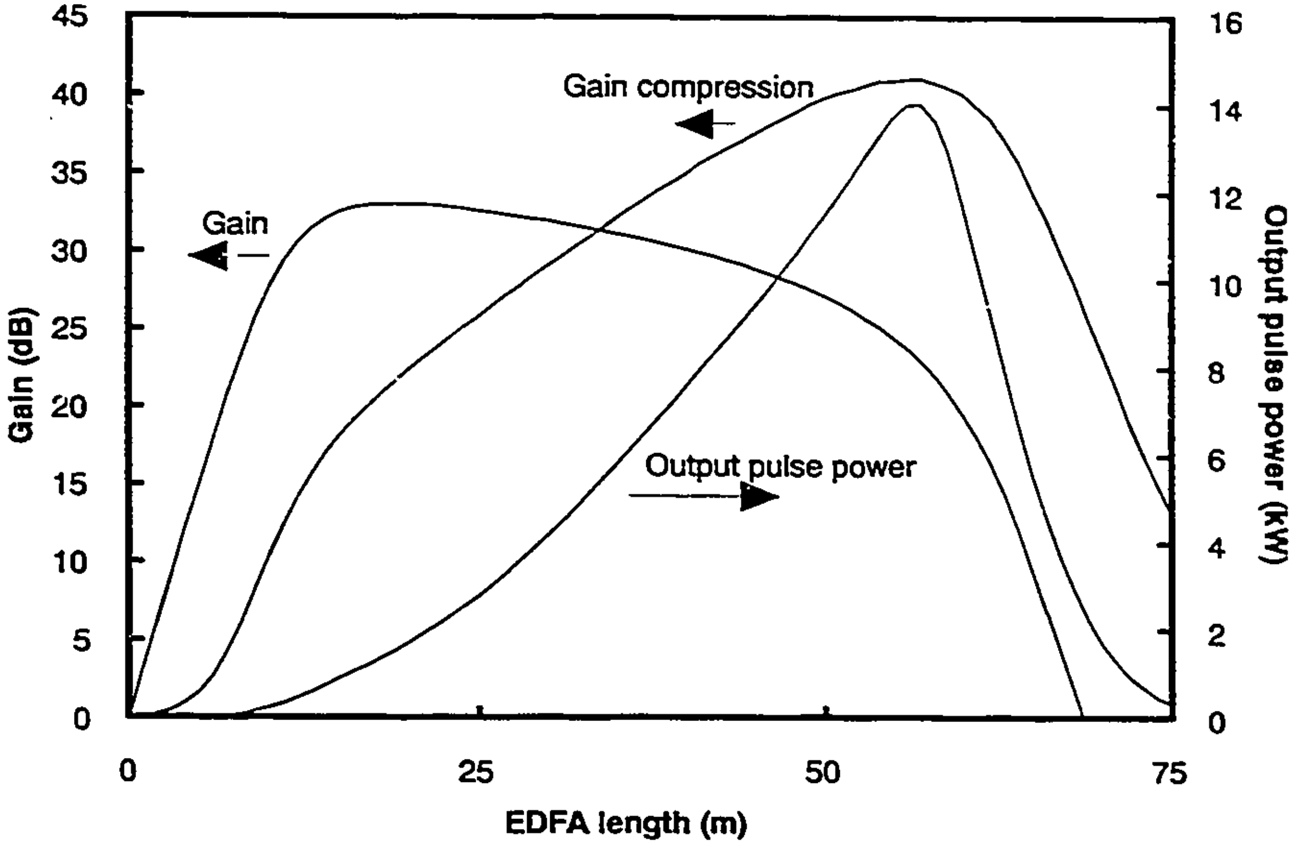

Fig. IV.7. Gain compression and pulse amplification vs EDFA fiber length. Pump power is 30 mW, signal power is 5 μW, gain is 33 dB, pulse duration is 40 ns, and pulse peak power is 1 W.

indicates that 10 dB gain compression is possible with pulse energies as low as 10 fJ. Since ASE is neglected during switching, the actual minimum required energy should be higher. For signal wavelength greater than 1530 nm, the optimum signal wavelengths are 1565-1575 nm, just beyond the gain peak at 1550 nm. In this spectral region there is a smaller difference between absorption and emission cross-sections (Fig. III.2) than at 1550 nm which favours gain compression. The model predicts the gain of a 5 μW, 1565 nm signal pumped by 45 mW can be compressed by 10 dB with a 10 pJ, 1530 nm pulse.

Combining the saturating pulse and signal in the erbium fiber with a directional coupler causes both beams to lose power. For efficient switching, the coupling ratio for the saturating pulse should be high. However, a high coupling ratio for the saturating pulse results in large input signal power loss. If the amplifier is operated in the saturated regime, which is the case for optimized switching (Fig. IV.7), this does not reduce the output signal power but it does increase the amplifier noise

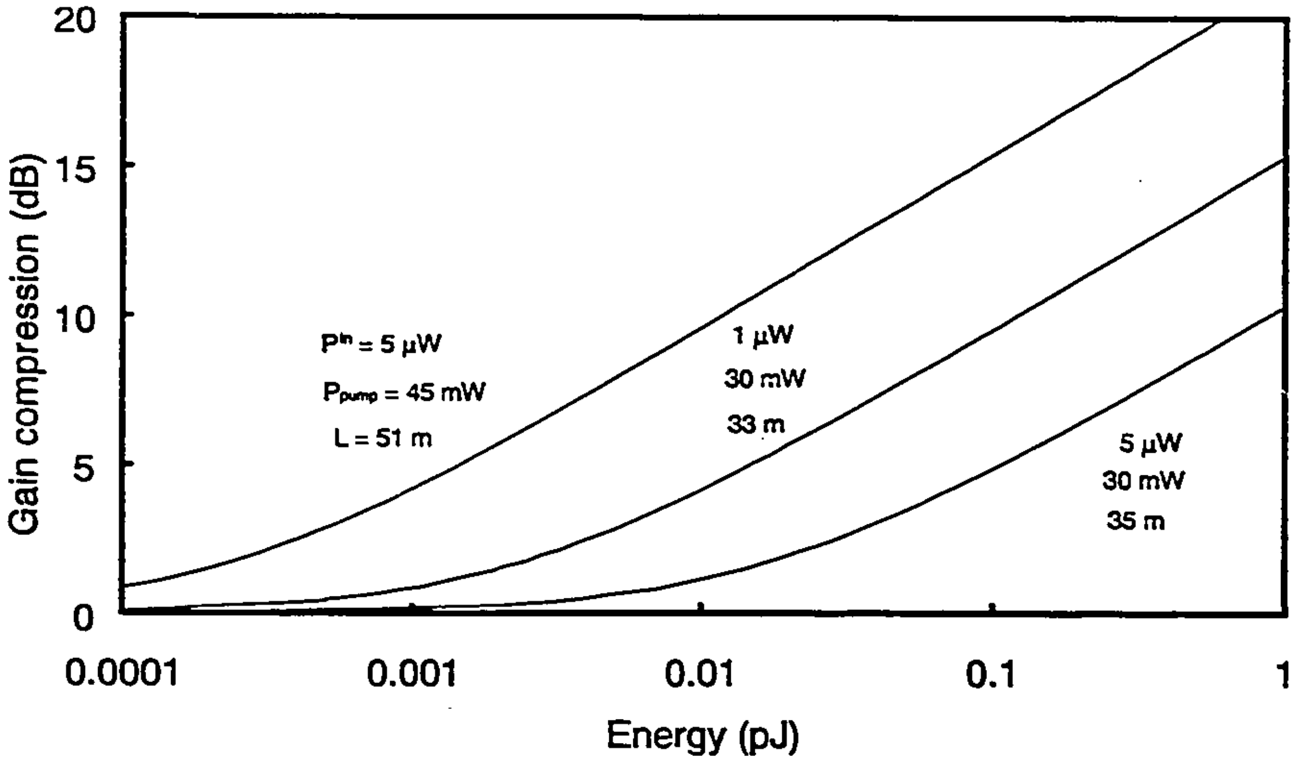

Fig. IV.8. Optimized switching vs pulse energy for a 1520 nm signal and 1530 nm switching pulses for different input powers and optimized fiber lengths.

figure. This trade off between efficient use of the switching pulse and signal input coupling loss must be considered when this type of switching is implemented. Also, the saturating pulse laser must generate pulses with energy greater than the required pulse energy by an amount equal to the switching pulse coupling loss.

The experiment and theory demonstrate that nanosecond gain compression in an EDFA can be achieved with a short saturating pulse. From this result, the obvious question is whether fast ON switching can be done with short pump pulses. We now investigate the possibility of gain recovery acceleration after gain compression. Fig. IV.9 shows theoretical gain recovery after saturation by a 1 W/40 ns switching pulse. The recovery resembles the experimental results presented in [81]. The output signal returns to its 10 mW initial value, with a small overshoot, after 2.5 ms of 30 mW pumping. The model predicts that gain recovery can be accelerated by applying a Gaussian pump pulse on top of the CW pump. The results are presented in Fig. IV.9 for different pump pulse widths. In each case the pump pulse enters the fiber one pump pulse FWHM after the switching pulse exits. The pump pulse energy is set at 32 μJ to have the same number of photons as the 20 μJ output

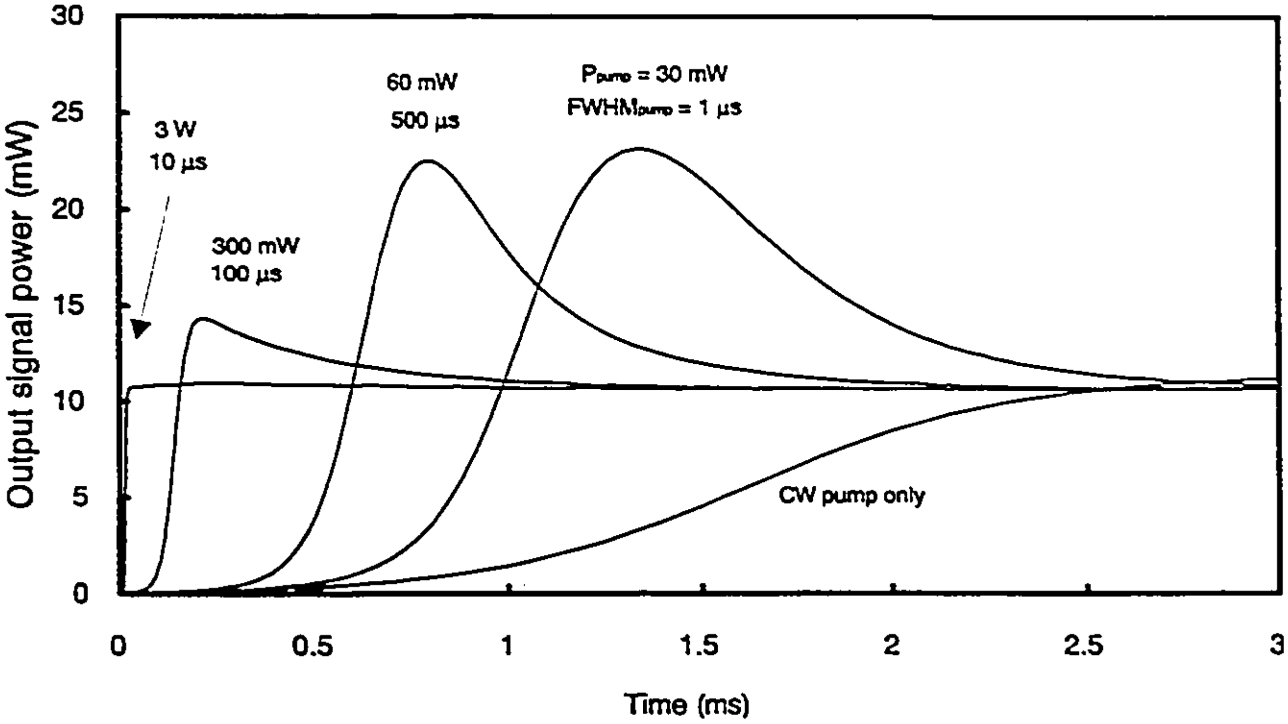

Fig. IV.9. Gain recovery for 30 µJ pump pulses. CW pump power is 30 mW, signal power is 5 µW, gain is 33 dB, and gain compression is 20 dB from a 1 W/ 40 ns pulse.

switching pulse. In our calculations, because of the underlying CW pump the total energy delivered to the fiber during the pump pulse increases with pulse width, thus causing a larger overshoot. Overshoot can be eliminated by adjusting the pump pulse so that the total number of pump photons delivered equals the extracted number of photons during switching. For a 3 W pump pulse the model predicts a 10 µs recovery time, approaching the physical limit set by the 7 µs pump level lifetime. Nanosecond gain recovery should be possible with a 1480 nm pump pulse since this pump level, being within the same electronic state, has a lifetime much less than one nanosecond. To simplify the calculations the pump, signal, saturating pulse, and pump pulse were all copropagating. Gain recovery would be faster and more efficient if the pump pulse entered from the opposite end of the fiber where the excited state depletion is greatest (Fig. IV.4). However, as discussed in the next section the damage threshold of various optical components gives a practical limit for the peak optical powers.

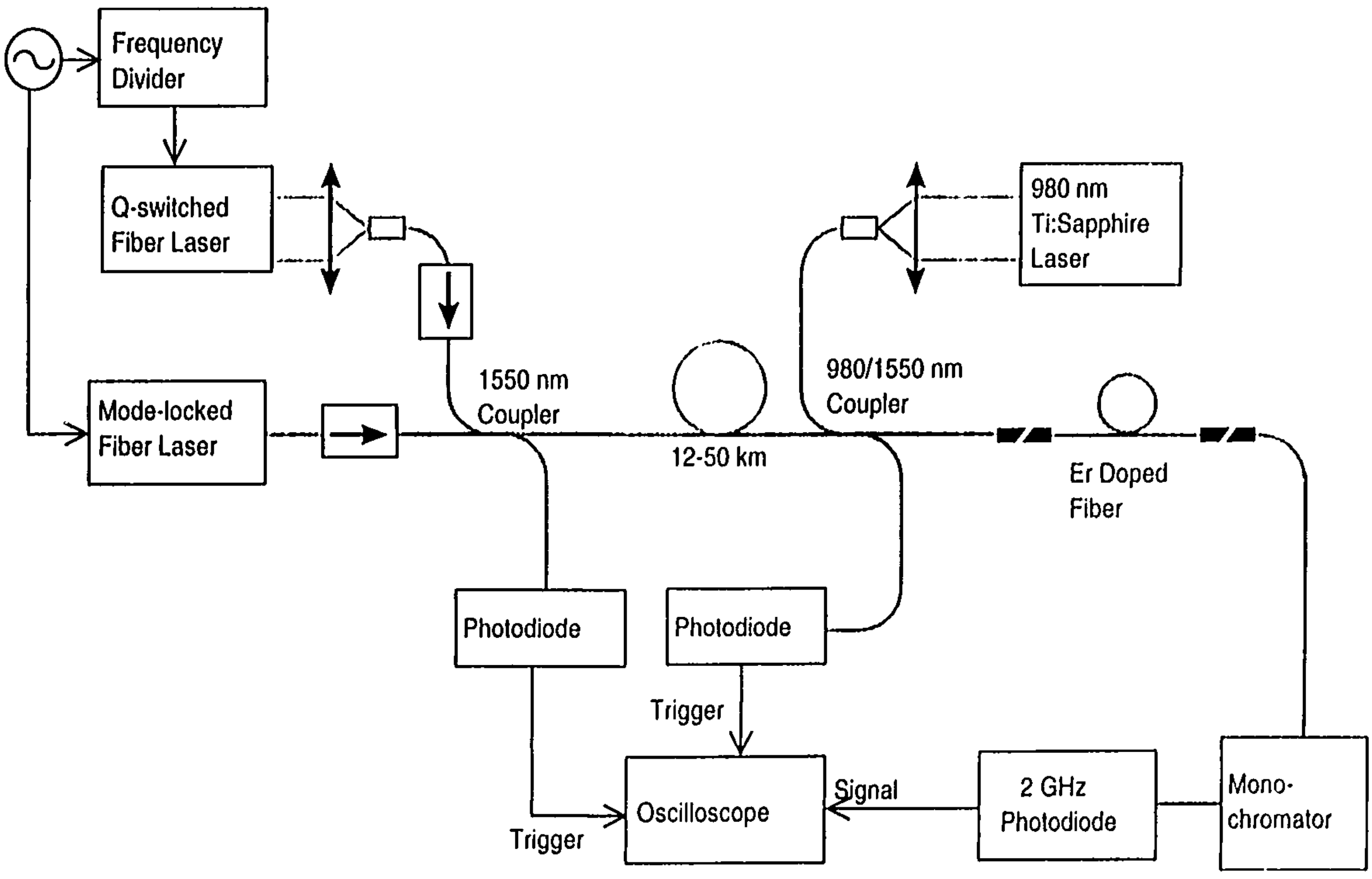

Fig. IV.10. Experimental configuration for remote EDFA switching.

IV.4 Remote EDFA Switching Experiments

Following the initial EDFA switching experiments and theoretical modelling, measurements were conducted on remote all-optical nanosecond EDFA switching [82]. The experimental configuration is shown in Fig. IV.10. The EDFA and tunable Q-switched erbium fiber laser were described in Section IV.2. An actively mode-locked erbium doped fiber ring laser was used as the signal. The signal laser and Q-switched laser were synchronized by being driven by the same signal generator. Optical isolators were used to prevent fiber amplifier ASE from affecting the fiber lasers. After the EDFA the signal was filtered from the Q-switched pulse by a Czerny-Turner spectrometer and then detected by an optical spectrum analyzer or a photodiode and oscilloscope.

The mode-locked fiber laser is shown in Fig. IV.11. It used 7 m of the erbium fiber used in

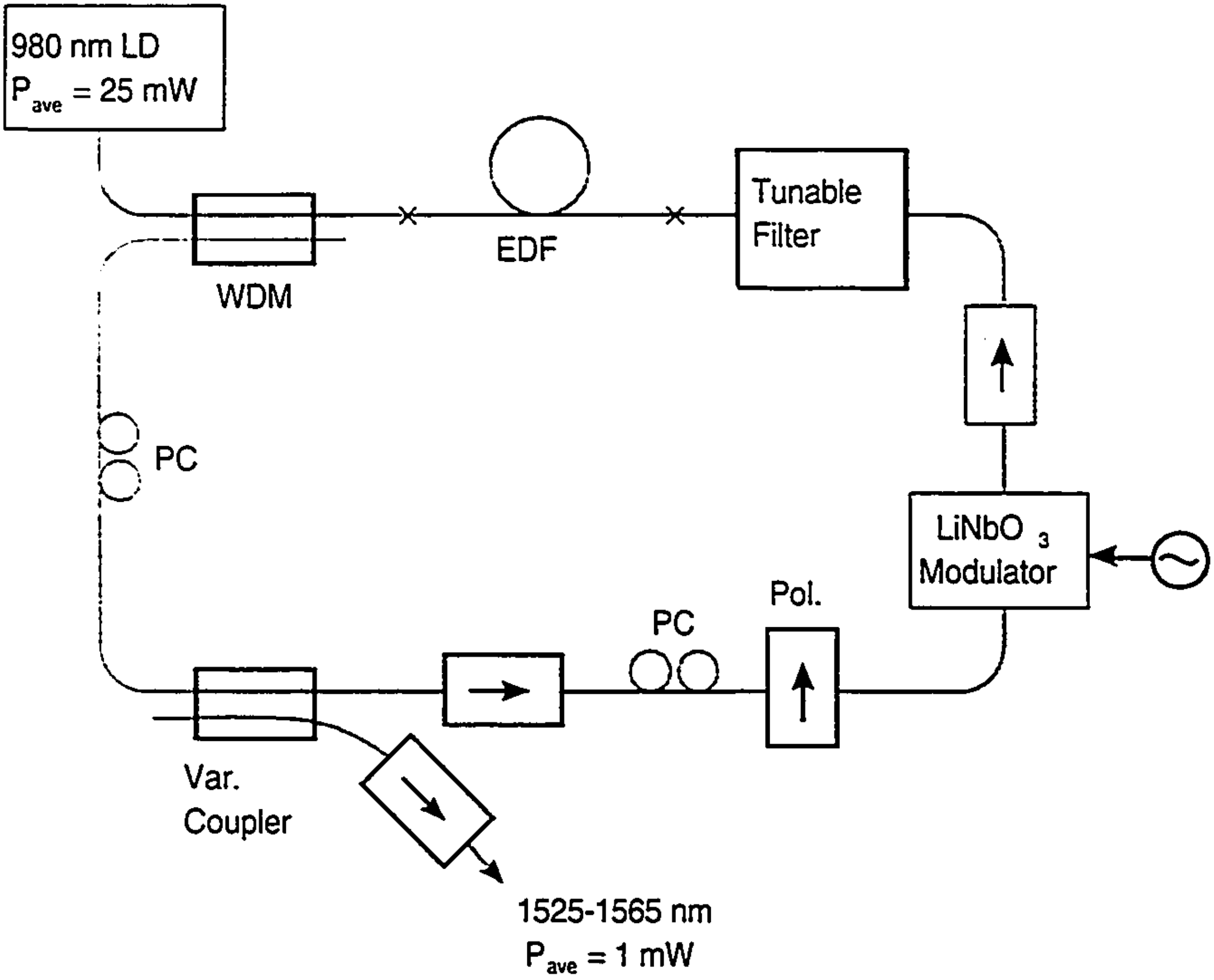

Fig. IV.11. Experimental configuration of mode-locked erbium fiber ring laser.

the EDFA. It was tuned from 1525 to 1565 nm with a rotating thin film dielectric filter and actively mode-locked with an 8 GHz lithium niobate intensity modulator. Since the modulator acts on the TE mode, it was preceded by a fiber polarizer and a fiber loop polarization controller. Optical isolators were used to enforce unidirectional lasing and to attenuate backreflections from the filter and intensity modulator. The variable fiber coupler was adjusted at each wavelength to maximize the output power. The laser produced a mode-locked pulse train with about 0.5 ns pulse widths, repetition rates of 8-250 MHz, and an average power of about 1 mW.

The high-energy Q-switched pulses caused some optical damage, especially on the connectors. For the two types of connectors used, FC/PC and APC, the APC connectors were more susceptible to damage. It is believed that the damage was caused by the Q-switched pulses heating dust on the connector ends. To avoid this problem, the connectors were replaced by fused fiber splices where the pulses were most powerful.

During the switching experiments the input switching pulse power was held slightly below the stimulated Raman scattering threshold described in the next chapter. A measurement of the

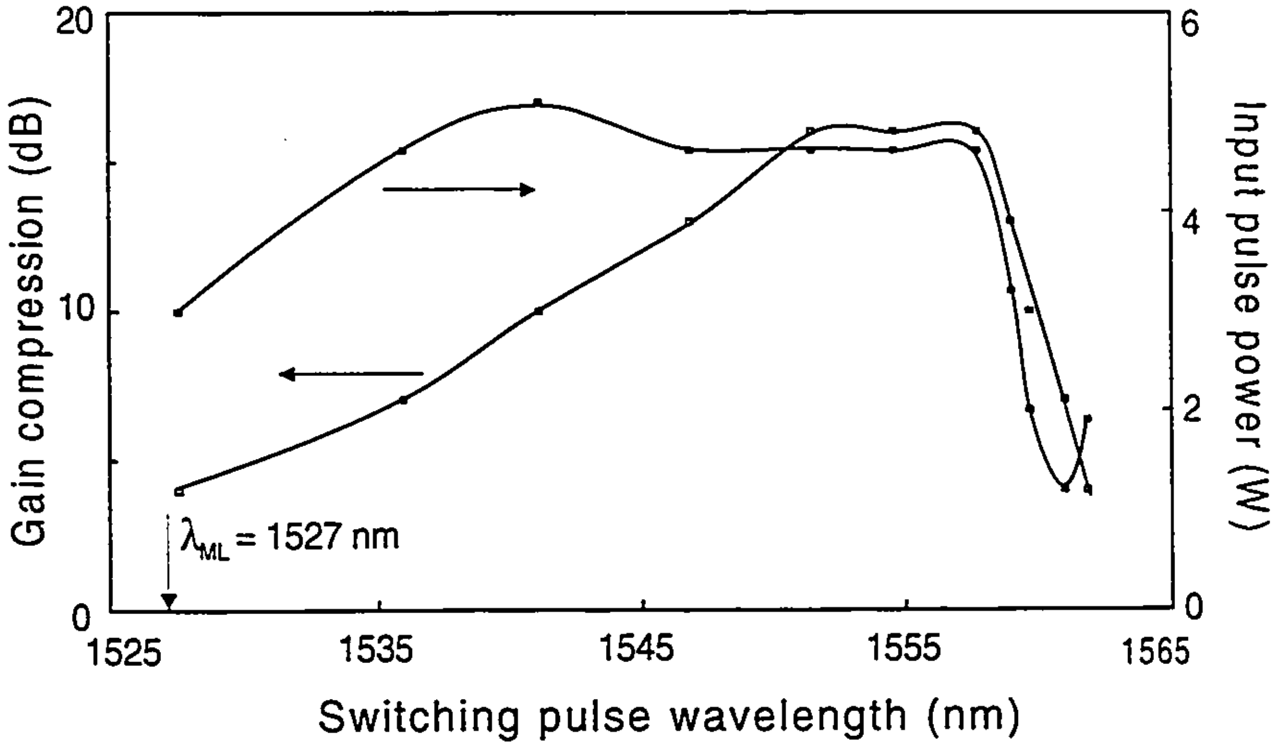

Fig. IV.12. Gain compression after 25 km vs switching pulse wavelength.

dependence of the switching on the signal and pulse wavelengths showed good agreement with theory. The gain compression was measured as the two lasers were scanned over their tuning ranges. As predicted, shorter signal wavelengths improved the gain compression. Therefore, the signal laser was set at 1527 nm, its shortest wavelength. The dependence on the switching wavelength is shown in Fig. IV.12. Gain compression was optimized when the Q-switched laser was operated within the second EDFA gain peak centred around 1555 nm. The 15 dB gain compression for 0.3 W switching pulses is an improvement of about 7 dB over the previous experimental results where the signal laser was not tunable [81].

Remote switching of the mode-locked pulse train is shown in Fig. IV.13 for 21 ns, 4.6 W (0.27 W at output) switching pulses transmitted over 25 km of fiber. The gain compression was 16 dB for 1554 nm switching pulses (top of Fig. IV.13) and 12 dB for 1539 nm switching pulses (bottom of Fig. IV.13). There was some leakage of the Q-switched pulse through the optical filter in the bottom graph where the switching wavelength was closer to the signal wavelength. The measured gain compression, optimized for the lasers used, is shown as a function of distance in Fig. IV.14. This figure shows that greater than 10 dB gain compression is obtainable for distances up to 30 km.

IV.5 Conclusions

This is the first work demonstrating the feasibility of nanosecond all-optical EDFA switching. Because of the three level nature of erbium ions, typical 30 dB gain for a pumped fiber can become over 100 dB attenuation for the same piece of unpumped fiber. The minimum required OFF switching energy is relatively very low for an all optical switch and is comparable to the lowest semiconductor electronic switching energies (see Chapter 21 of [70]). This is expected since the weak switching pulse is amplified at the beginning of its propagation through the amplifier and acquires energy from the erbium ions. The strong absorption in the depopulated region near the fiber end can easily exceed the amplification in the undepleted first part of the amplifier resulting in a high dynamic range of gain switching. Efficient gain compression, which scales with pulse energy, is therefore practical with pulses from a diode-pumped Q-switched fiber laser. Switching time is limited by the saturating pulse duration and can approach the fundamental limit of the metastable level Stark component relaxation times (<1 ps). These results illustrate that the EDFA gain dynamics operate on a much smaller time scale than previously thought.

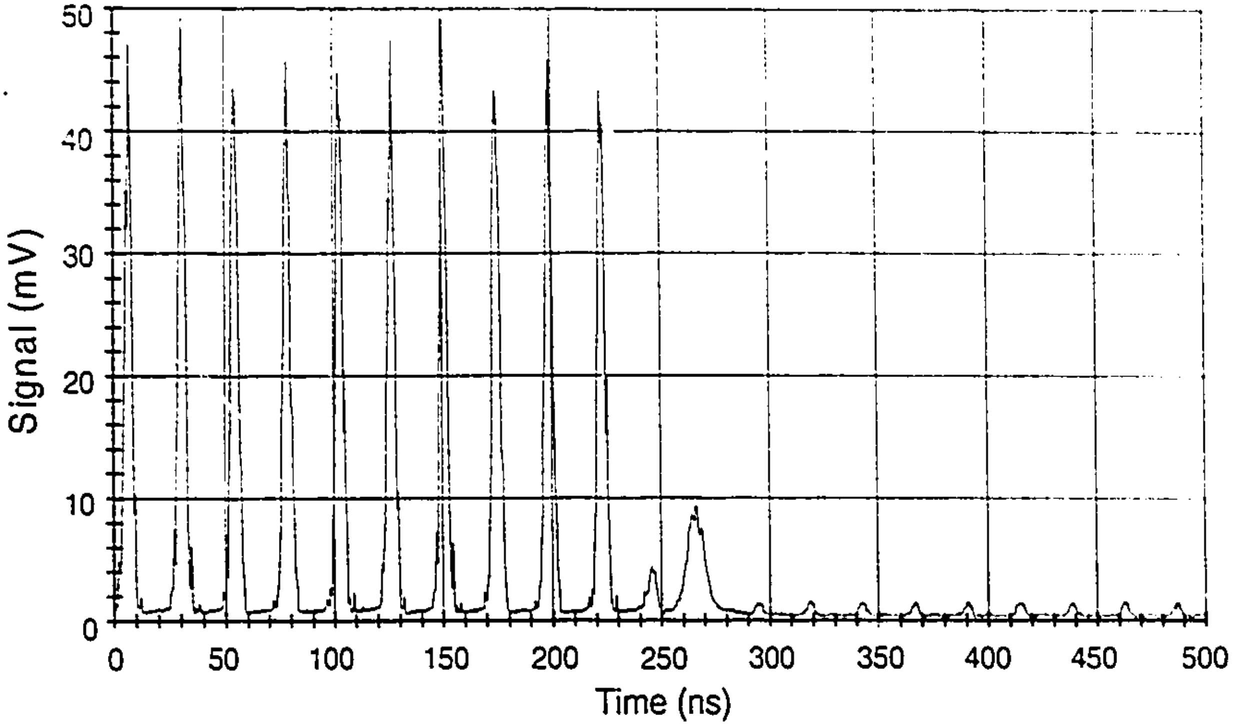

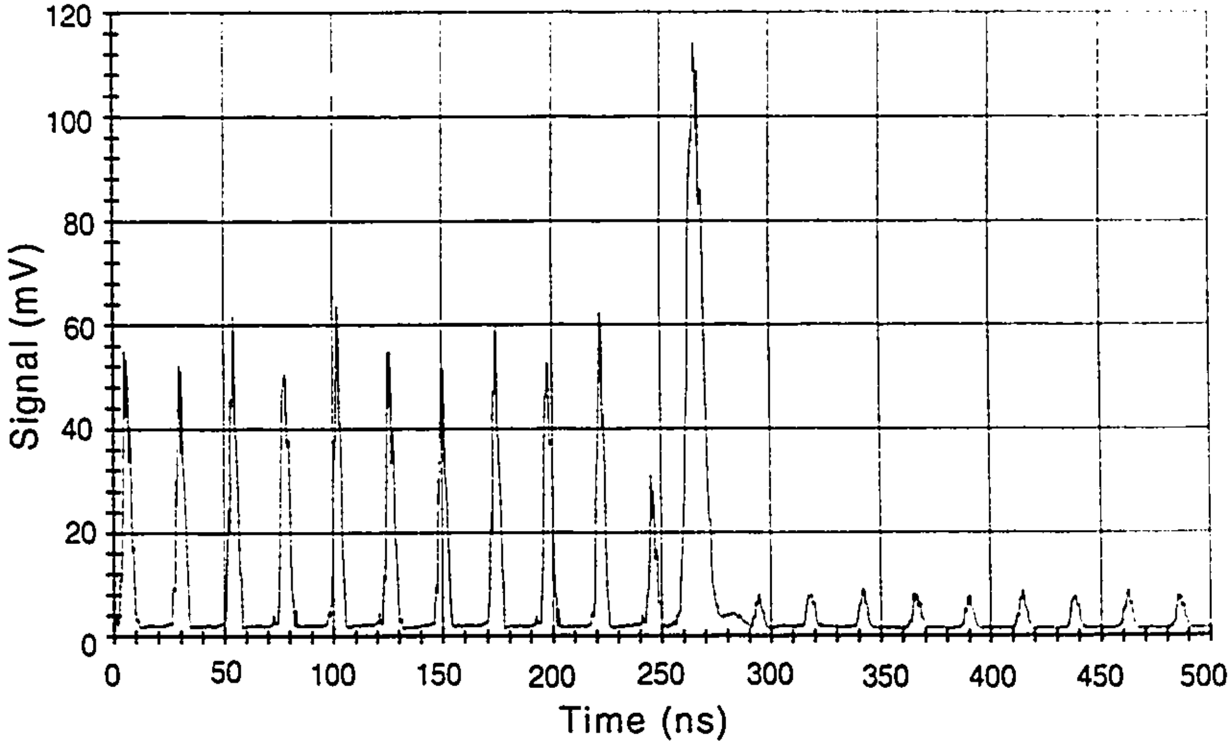

Fig. IV.13 25 km remote switching of a 1527 nm pulse train. 1.1 W, 21 ns pulses give (top) ΔG = -16 for λ = 1554 nm and (bottom) ΔG = -12 dB for λ = 1539 nm.

Short, high energy, pump pulses can restore the gain in times limited by the pump level lifetime. The ON switching pump pulses energy is up to five orders of magnitude greater than that of the OFF switching pulses. Switching ON time is limited by the pump pulse duration and can approach the pump level lifetime (<1 ns for 1480 nm pumping, ≈ 7 µs for other pump wavelengths).

As demonstrated, optical switching at 1550 nm can be done remotely from tens of kilometers because of the very low fiber loss. However, the optical damage threshold places a practical limit on the peak optical power. Furthermore, the next chapter describes how the transmission of the high-power pulses required for remote EDFA switching over long distances is limited by stimulated Raman scattering. These problems caused by the high pulse energy can be reduced by transmitting lower power switching pulses and amplifying them in another EDFA located before the amplifier being switched.

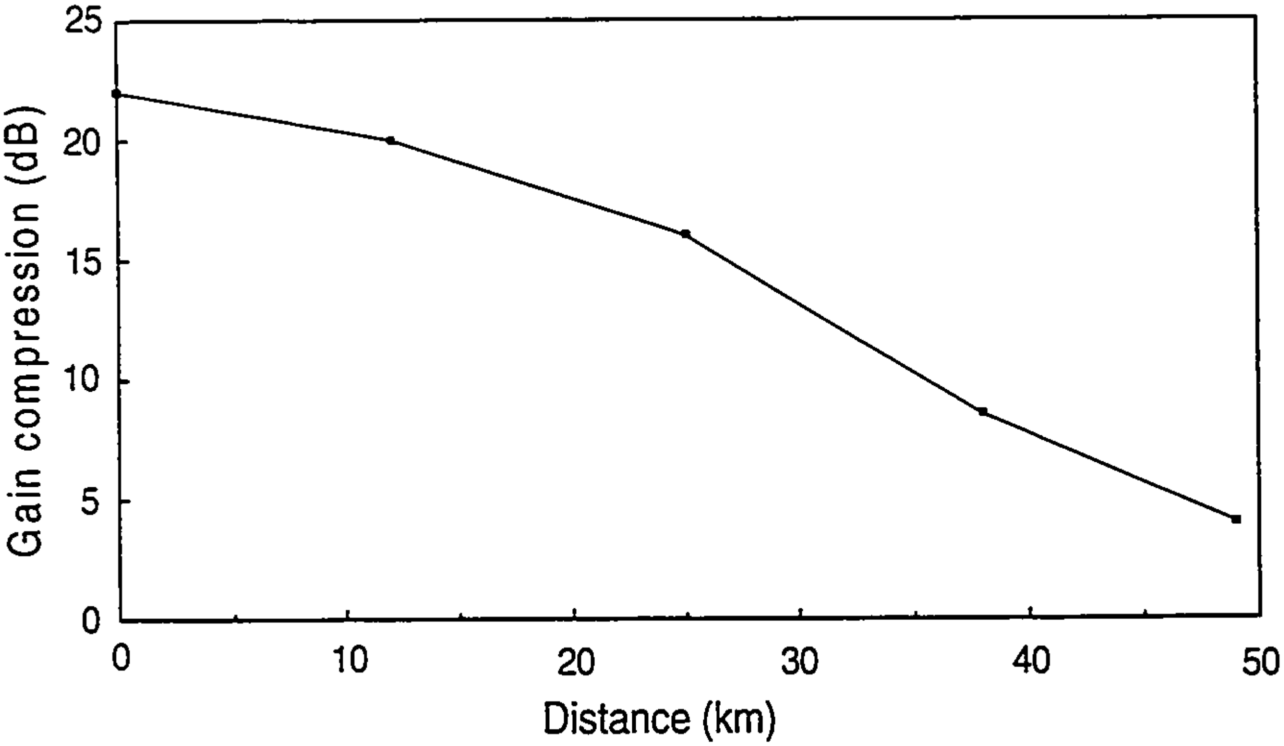

Fig. IV.14. Optimized gain compression vs distance.

Chapter V

Effect of Stimulated Raman Scattering on High-Energy Pulse Transmission

V.1 Introduction

After successfully demonstrating and modelling all-optical EDFA switching, the practicality of using this technique for remote switching was investigated. Transmission of the high power pulses required for switching is limited by several nonlinear effects. For the 1550 nm nanosecond pulses with peak power on the order of ten Watts, the dominant nonlinear effect is stimulated Raman scattering (SRS) [9] (see section I.1.3). The limitations of transmitting high power optical pulses over long distances due to SRS is also of interest for other switching applications and applications involving remote optical powering [83]. For example, with a central power supply the required power for remote devices such as switches and optical receivers can be transmitted as light over optical fibers and converted to electrical energy at remote locations [84].

SRS has been observed in various materials, including optical fiber. However, experimental work in fibers has been mostly limited to using high power pulsed Nd:YAG lasers operating at 532 or 1060 nm [9]. The research on Raman scattering within the 1550 nm telecommunications window has concentrated on Raman amplification and the limitations that it imposes on the total number of channels in dense WDM networks [85]. In the previous research, the Raman interaction involved amplification of two or more input signal beams. In the type of Raman interaction studied here, there is only an input pump beam and the signal beam is generated from amplified spontaneous Raman scattering [86].

V.2 Experimental and Theoretical Results

In this section, the experimental measurements of SRS are described, the pulse propagation is studied with a numerical model, and conclusions are drawn on the limitations of high power pulse propagation in single-mode optical fibers at 1550 nm. In accordance with the literature, in this section the switching pulse is denoted as the pump pulse and the Raman generated pulse is denoted as the Stokes pulse.

Pulses from the 1550 nm Q-switched erbium doped fiber laser with FWHM = 13 and 18 ns were launched into 50 km of single-mode fiber. The input peak power was varied up to about 60 W. The spectral and temporal distributions of the output pulses were monitored at 12 km intervals. Fig. V.1 shows, for different input powers, the measured output power and spectra for 13 ns FWHM pulses propagated through 12 km of fiber. For input powers less than about 10 W, the output pulses resembled the input pulses with the expected attenuation (0.25 dB/km). When the input power is greater than the threshold (= 10 W) a Stokes pulse trails the pump pulse by 20-30 ns.

A 1550 nm pump pulse in silica optical fibers spontaneously generates Stokes photons with a broad spectrum (≈7 THz) centred at 1650 nm. The Stokes photons guided by the fiber in the forwards direction are then amplified by SRS. The Raman gain is proportional to the pump power so there are power and fiber length thresholds. Above threshold, the Raman gain is substantially stronger than the fiber attenuation at the Stokes wavelength.

The output pump pulse is shorter than the input pulse due to depletion of the rear of the pulse by the Stokes pulse. The temporal observance of the trailing pulse has associated with it the appearance of the broad Raman spectrum shown in the bottom of Fig. V.1. The Stokes pulses are inherently noisy in time and spectrum, since they are generated from a spontaneous process. The pump and Stokes pulses are separated in time due to their chromatic group velocity difference. This separation, or walkoff, increases with input power since the Stokes pulse is generated at an earlier point in the propagation for greater input powers. And as the input power is increased, the peak Stokes power increases to a maximum for a 33 W input and then decreases to a plateau for input powers greater than 43 W. When the input pump power is above threshold, Raman conversion proceeds until the pump is depleted to the point where it is below threshold. Thus, the output pump power is fixed at about 8 W, being insensitive to the input power. This illustrates that the output power is limited by SRS. For input powers far above threshold there is also a smearing, in time and frequency, of the Stokes pulse because of the group velocity variation across the Stokes spectrum.

The measured propagation of 26W/18 ns pulses through 50 km of fiber is shown in Fig. V.2. Raman conversion is completed within the first 12 km of fiber. Beyond that, the walkoff increases with distance as the pulses propagate with the attenuation of the Stokes pulse being slightly higher than the pump pulse. The measured walkoff is about 2.4 ns/km.

The propagation of the pump and Stokes pulses are theoretically modeled with the following

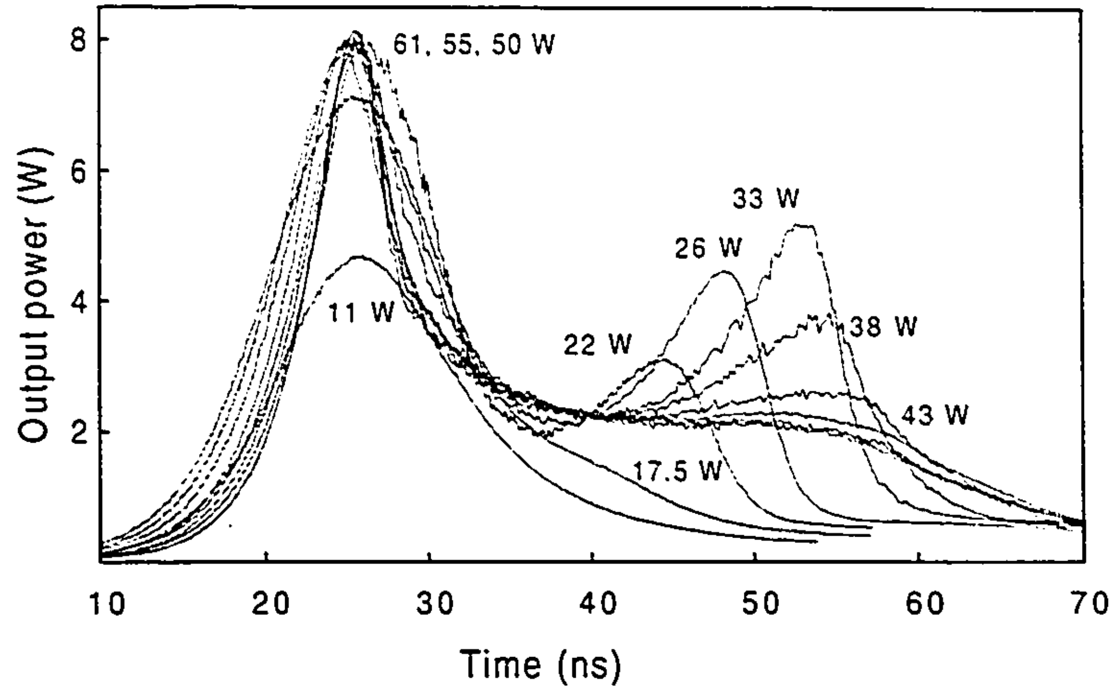

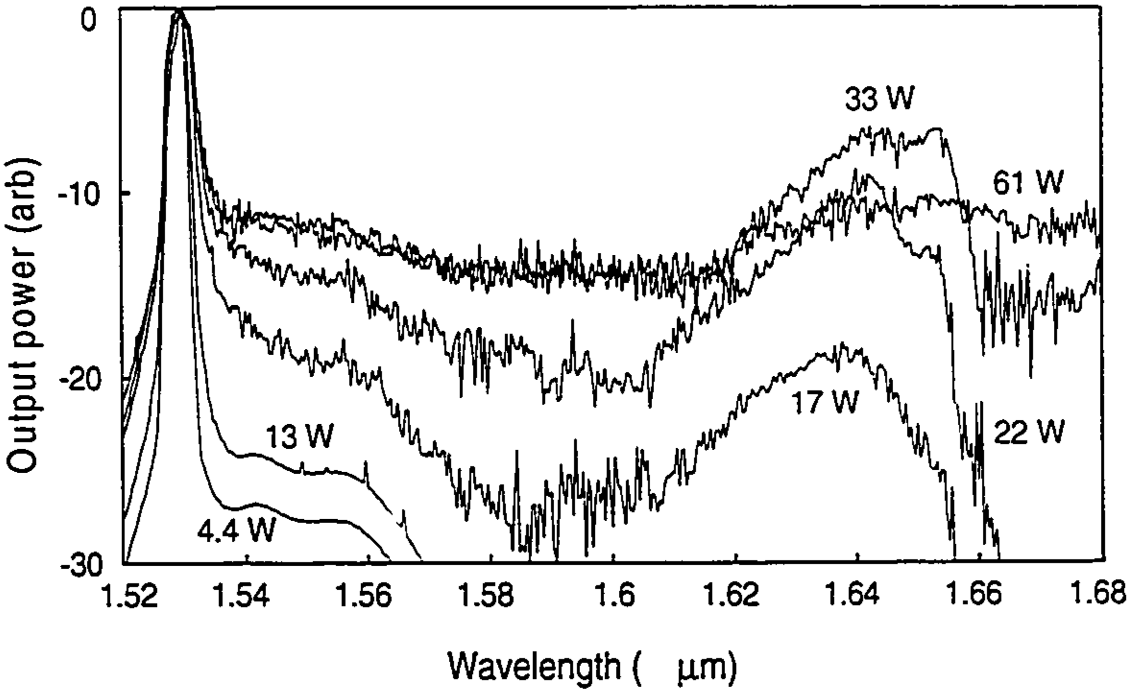

Fig. V.1. Observed output pulse shape (top) and spectra (bottom) after 12 km of fiber for 13 ns FWHM pulses with indicated input powers.

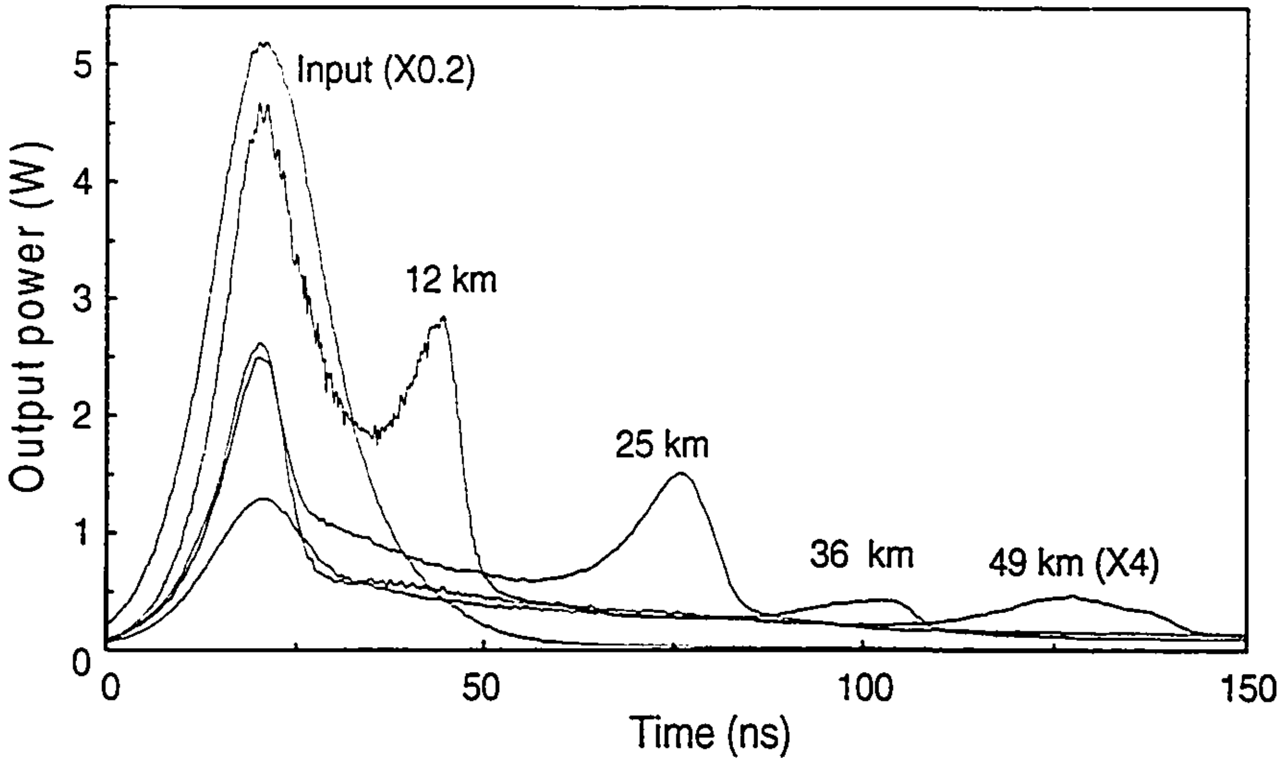

Fig. V.2. Measured propagation of 18 ns FWHM, 26 W input pulses through 50 km of fiber.

coupled equations where subscript p (st) denotes the pump (Stokes) pulse:

$$\frac{\partial A_p}{\partial z} + \frac{1}{v_{gp}}\frac{\partial A_p}{\partial t} + \frac{i}{2}\beta_{2p}\frac{\partial^2 A_p}{\partial t^2} + \frac{\alpha_p}{2}A_p = i\gamma_p\left(|A_p|^2 + 2|A_{st}|^2\right)A_p - \frac{g_R}{2A_{eff}}\frac{\lambda_{st}}{\lambda_p}|A_{st}|^2 A_p \tag{81}$$

$$\frac{\partial A_{st}}{\partial z} + \frac{1}{v_{gst}}\frac{\partial A_{st}}{\partial t} + \frac{i}{2}\beta_{2st}\frac{\partial^2 A_{st}}{\partial t^2} + \frac{\alpha_{st}}{2}A_{st} = i\gamma_{st}\left(|A_{st}|^2 + 2|A_p|^2\right)A_{st} + \frac{g_R}{2A_{eff}}|A_p|^2 A_{st} \tag{82}$$

where A_p (A_{st}) is the complex modal amplitude of the pump (Stokes), normalized to the initial peak amplitude of the pump (A_k is proportional to $\sqrt{P_k}$). In (81) and (82) β_2 is the second order dispersion coefficient, α is the absorption coefficient, g_R is the Raman gain coefficient, γ is the fiber nonlinear coefficient ($\gamma = 2\pi n_2/\lambda_p A_{eff}$) where n_2 is the nonlinear index coefficient, and A_{eff} is the effective fiber cross section. On the left hand side of (81) and (82) the second term containing the group velocity v_g represents the first order dispersion which describes the pulse walkoff, the third term represents the second order dispersion which describes the pulse broadening, and the fourth term represents the fiber attenuation. On the right hand side the first term represents self phase modulation, the second term represents cross-phase modulation, and the third term represents the Raman gain which describes the amplification of the Stokes pulse and depletion of the pump pulse.

The coupled differential equations, (81) and (82), are solved by the split-step Fourier method (beam propagation method) in which the nonlinear and dispersive effects are assumed to act independently over each small distance step [9]. Ideally, at each distance step the spontaneous Raman generation and Raman amplification should be integrated over the entire Raman bandwidth. Reasonably good agreement with theory was obtained however, by assuming that the Raman generated light is monochromatic and at the peak of the gain spectrum and the Raman gain coefficient equals the value at the gain peak. These assumptions lead to the simulation predicting slightly greater Raman conversion than observed experimentally. Furthermore, the number of Stokes photons spontaneously generated along the fiber was approximated by an equivalent Stokes input power as described in Ref. [87]:

$$P_{St}(0,t) = \frac{\sqrt{\pi}\,hc}{2\lambda_{St}} \frac{\Delta f}{\sqrt{I_p g_R L_w}} \tag{83}$$

where Δf is the Raman bandwidth, I_p is the input pulse peak intensity $(P_p(0)/A_{eff})$, and L_w is the walkoff length defined by

$$L_w = \frac{T_0}{\left| \frac{1}{v_g(\lambda_p)} - \frac{1}{v_g(\lambda_{St})} \right|} \tag{84}$$

where T_0 is the pulse width ($T_0 = T_{FWHM}/1.763$ for a sech pulse). This assumption was tested by simulating a pulse propagation with different equivalent input Stokes powers. Increasing the equivalent Stokes input power by three orders of magnitude led to only a doubling of the output Stokes power, thus demonstrating that the model is insensitive to the equivalent Stokes input. The calculations take $\lambda_p = 1530$ nm, $\lambda_{st} = 1630$ nm, $\alpha_p = 0.2$ dB/km, $\alpha_{st} = 0.8$ dB/km, $g_R = 3.2\text{x}10^{-14}$ m/W (assuming two orthogonal polarization coefficients), $A_{eff} = 75$ μm^2, $n_2 = 3.2\text{x}10^{-20}$ m^2/W, $\Delta f = 7$ THz, $\beta_{2p} = -21$ ps^2/km, $\beta_{2st} = -30$ ps^2/km, and the group index $n_g = 1.462$. Modelling was done with 1000

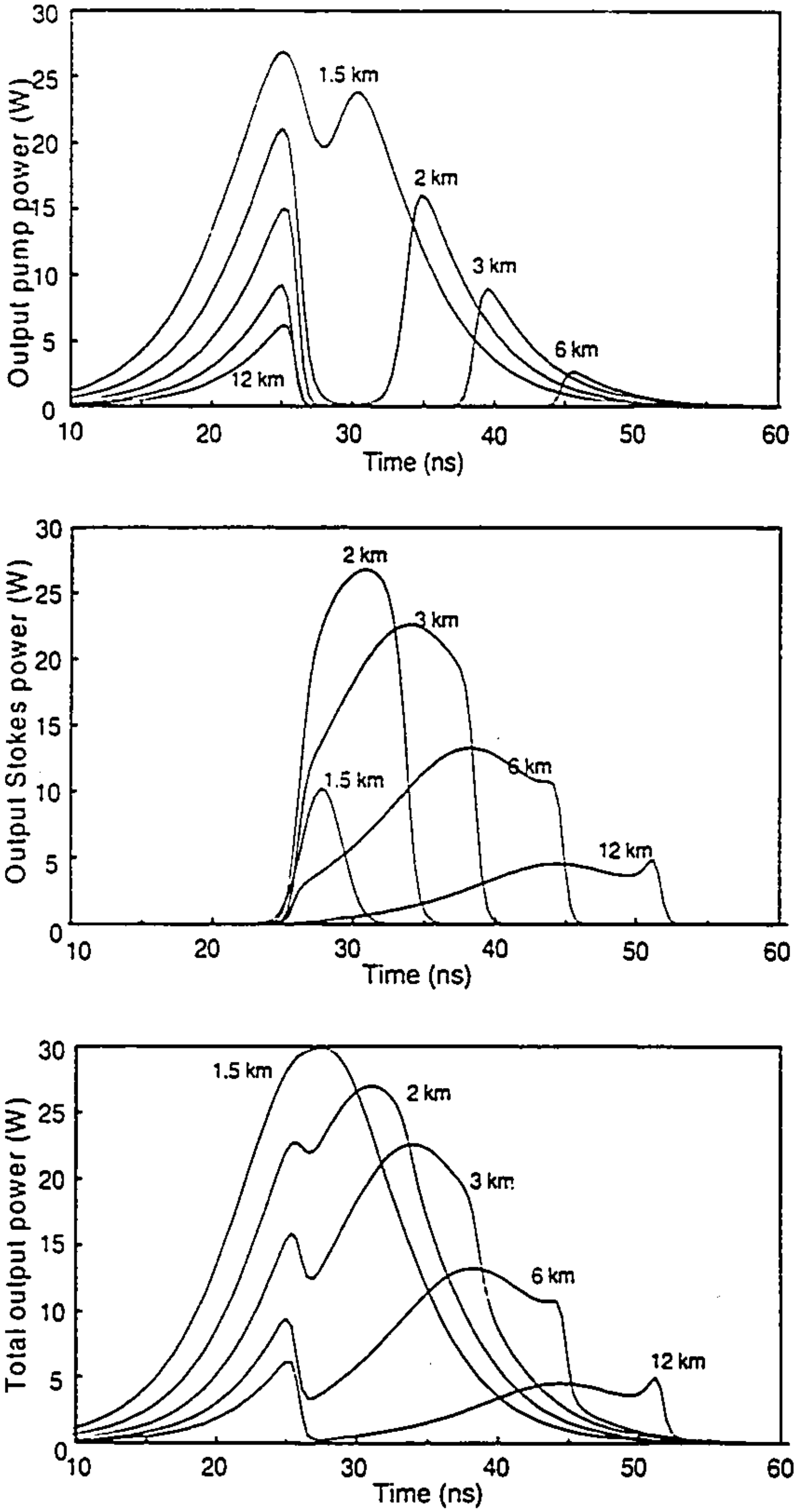

Fig. V.3 Theoretical propagation of pump pulse (top), Stokes pulse (middle), and resultant (bottom) for 33 W/ 13 ns input pulses.

distance steps and 1024 time steps.

Figure V.3 shows theoretically how the pump pulse, Stokes pulse, and resultant evolve in the fiber for input 33 W/13 ns pulses. After about 1 km the Stokes pulse is generated in the peak region of the pump pulse, causing pump depletion. As the two pulses copropagate, the Stokes pulse begins to lag behind the pump pulse, continually converting energy from the pump pulse. After 2 km depletion is completed in the section of the pump pulse just behind the peak. As the walkoff increases, the rear of the Stokes pulse is amplified by the pump tail, creating a second peak in the Stokes pulse. Depletion of the rear half of the pump pulse is complete after 12 km.

Figure V.4 shows the results of the simulation for propagation in 12 km of fiber, corresponding to the measured values in Fig. V.1. The theoretical Raman conversion is slightly higher than that observed and the pulse shape is slightly different. In agreement with experiment, depletion induced narrowing of the pump pulse is shown along with saturation of the output pump power. Experimentally, the wide spectral distribution of the Stokes photons leads to a smoothing of the Stokes pulse, whereas the model assumption of monochromatic Stokes photons leads to the peculiar pulse shapes that develop as shown in Fig. V.3. Because of the assumption of monochromaticity, the theoretical spectrum varies greatly from the measured spectrum. Although group velocity dispersion has negligible effect, self-phase modulation causes some spectral broadening of the pump pulses.

The Raman threshold is illustrated by Figs. V.5 and V.6. Figure V.5 shows the theoretical evolution of the Stokes pulse energy along the fiber for different input pump powers. There is a distance threshold (minimum length of fiber required for significant Stokes conversion) that decreases as the input pump power decreases. As a consequence, for a given fiber length there is an input power threshold (minimum input power for significant Stokes conversion). After the threshold distance is reached, the Stokes pulse experiences exponential gain with gain coefficient $g_R P_p$ until the pump pulse is depleted. The Stokes pulse subsequently decays exponentially. Figure V.6 shows the corresponding evolution of the pump pulse. The pump pulse decays exponentially until the threshold distance. As the Stokes pulse is amplified the pump pulse is depleted exponentially with a larger attenuation coefficient. After pump depletion is completed, the pump pulse again decays exponentially with the characteristic fiber attenuation coefficient. The middle graph in Fig. V.6 shows how the effect of pump depletion on the pump pulse FWHM. This graph illustrates how quickly the

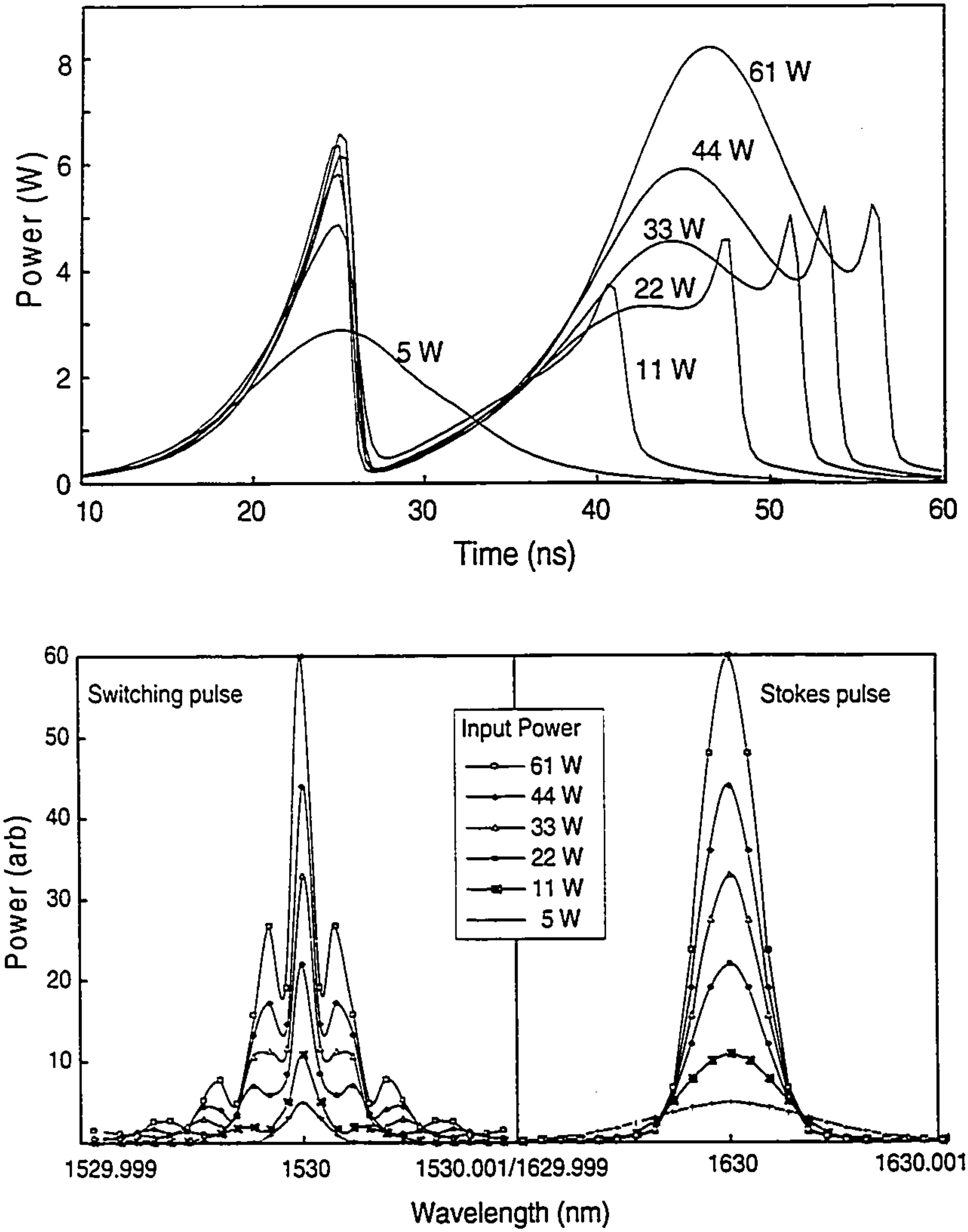

Fig. V.4. Theoretical output power (top) and spectra (bottom) after 12 km of fiber for 13 ns FWHM pulses with indicated input powers.

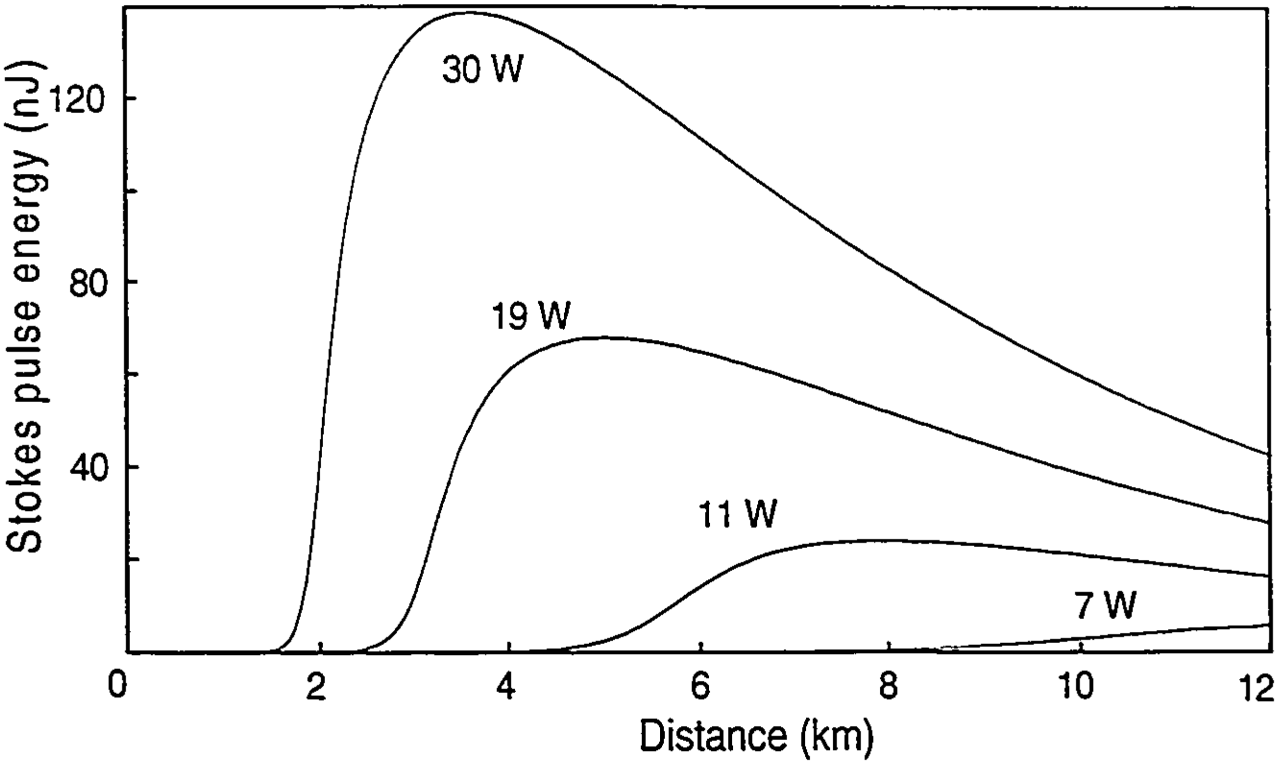

Fig. V.5. Theoretical Stokes pulse energy vs distance for 18 ns switching pulses with indicated input powers.

depletion occurs. The energy curves in the bottom of Fig. V.6 indicate that for a given distance, there is an optimum input power that maximizes the energy transfer. For the example shown, for fibers 8-12 km long an input pump power of 7 W delivers the most energy. For 7 W input power, the Stokes pulse energy indicated in Fig. V.5 has not yet reached a maximum after 12 km. Hence, the energy conversion and consequently the pump depletion is incomplete. Therefore, 7 W input pulses deliver more energy than higher power pulses, since the latter are completely depleted at the output.

This result is further exemplified by the experimental results in Fig. V.7 along with the corresponding theoretical curves in Fig. V.8. In Fig. V.7 the measured output pump power, FWHM, and energy for a 12 km fiber are shown as functions of the input power. The peak output power increases as the input power increases until the threshold is reached. Beyond threshold, the output power is approximately constant. However, the measured energy decreases above threshold because of the decrease in the FWHM. The experimental energy is defined as peak power times FWHM. Although this definition is consistent with the literature, it overestimates the pump energy since (i) typical pulses have an energy less than the peak power times the FWHM and (ii) the pump and

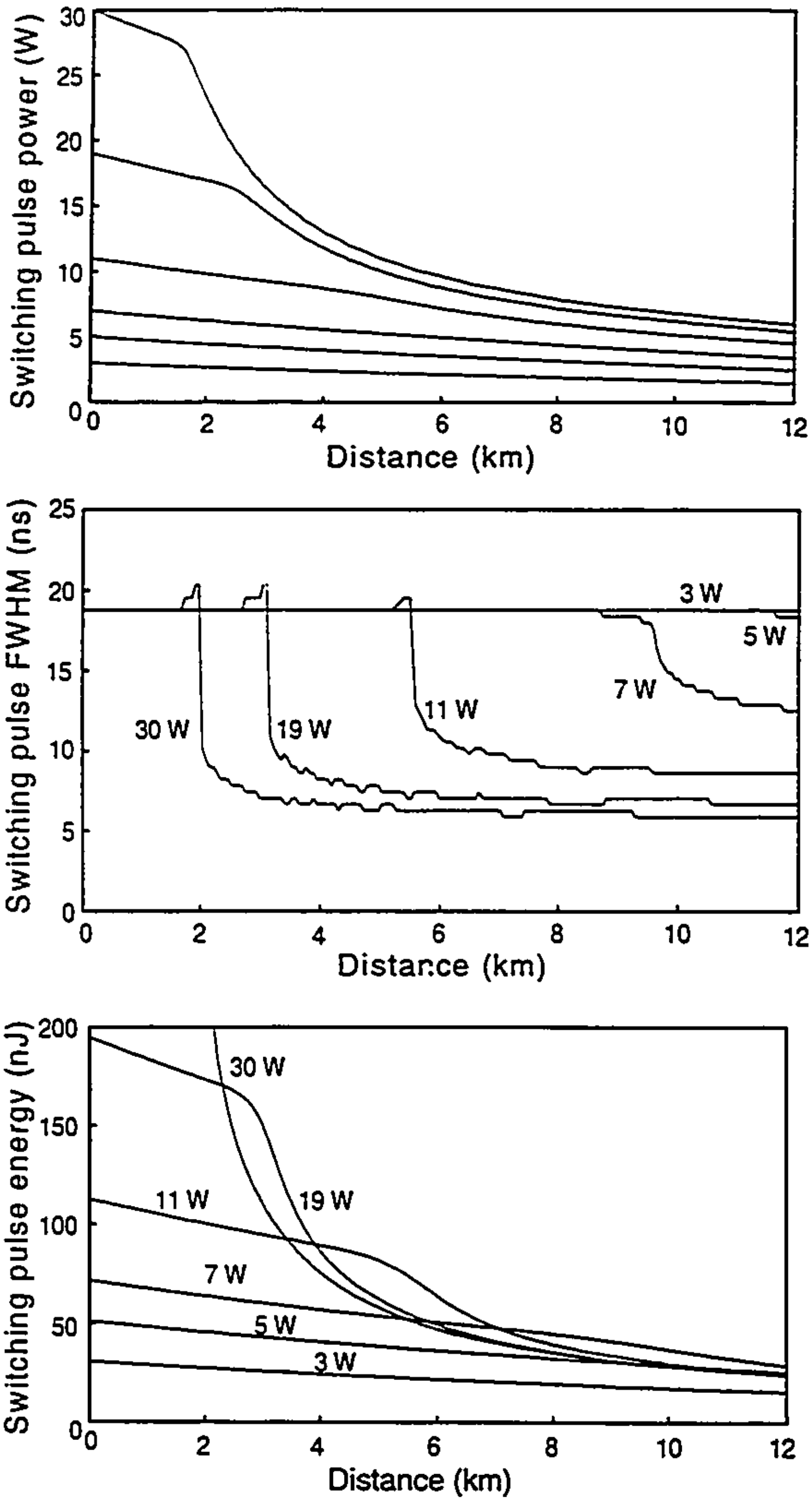

Fig. V.6. Theoretical 18 ns FWHM switching pulse output power (top), FWHM (middle), and energy (bottom) vs distance for indicated input powers.

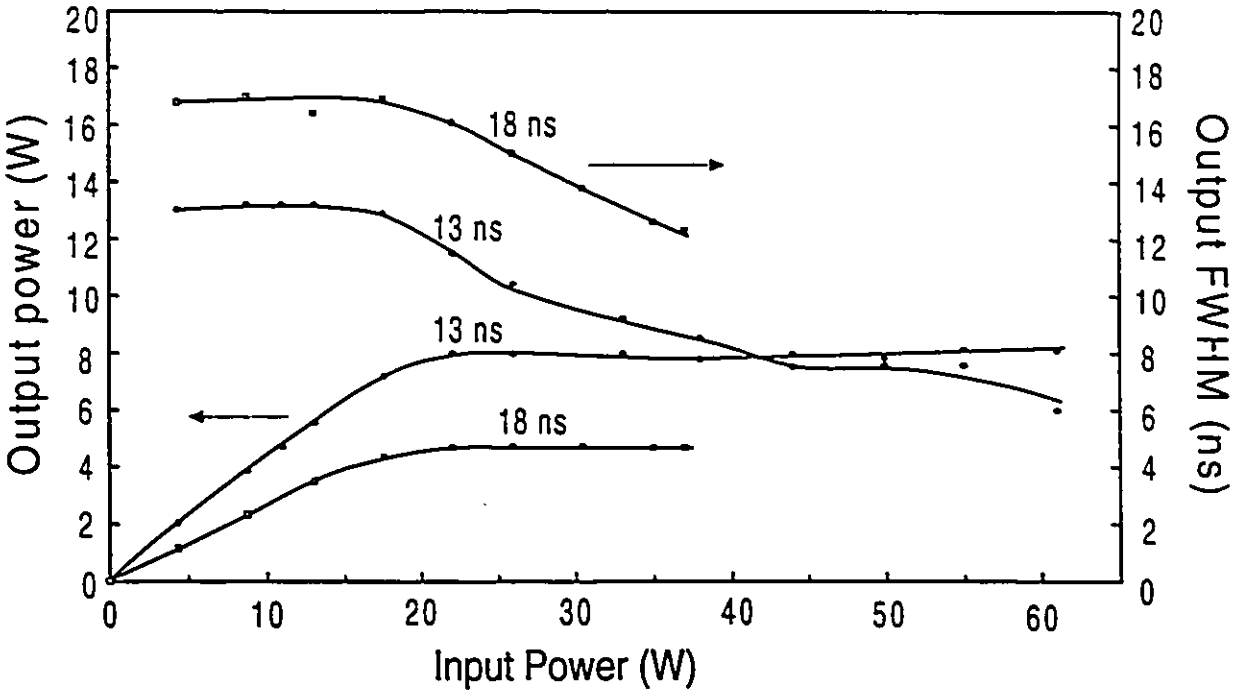

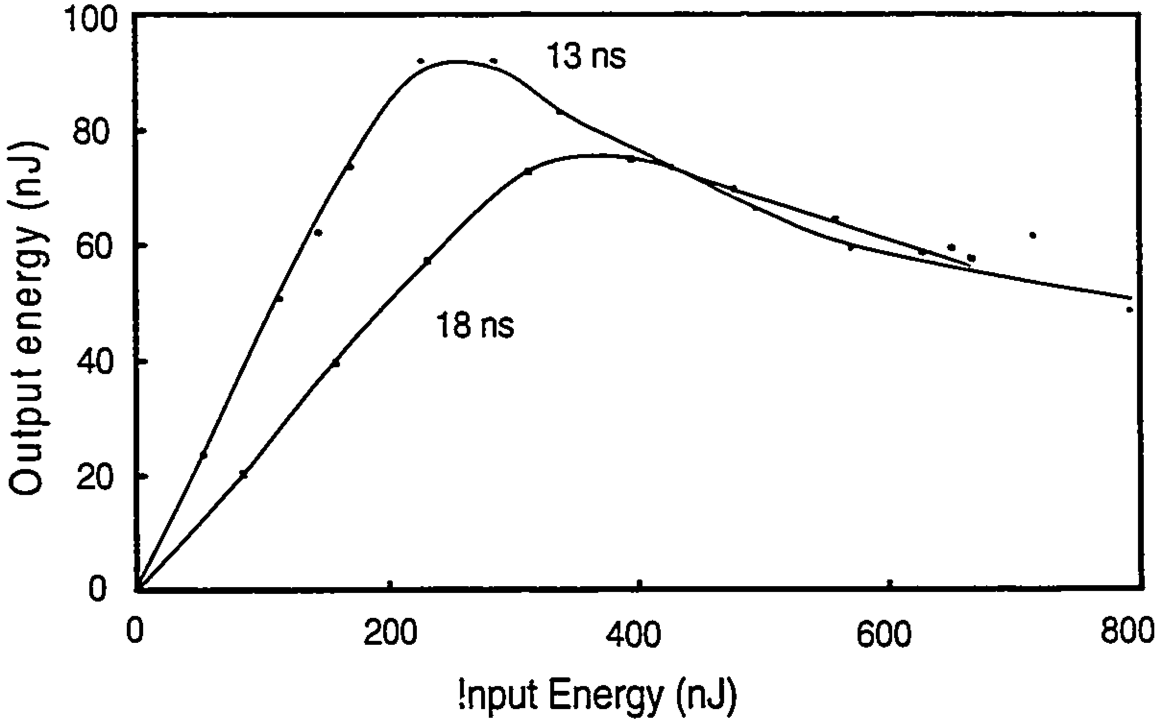

Fig. V.7. Observed output pump pulse power (top), pulsewidth (top), and energy (bottom) vs input power for 13 ns and 18 ns pulses transmitted through 12 km of fiber.

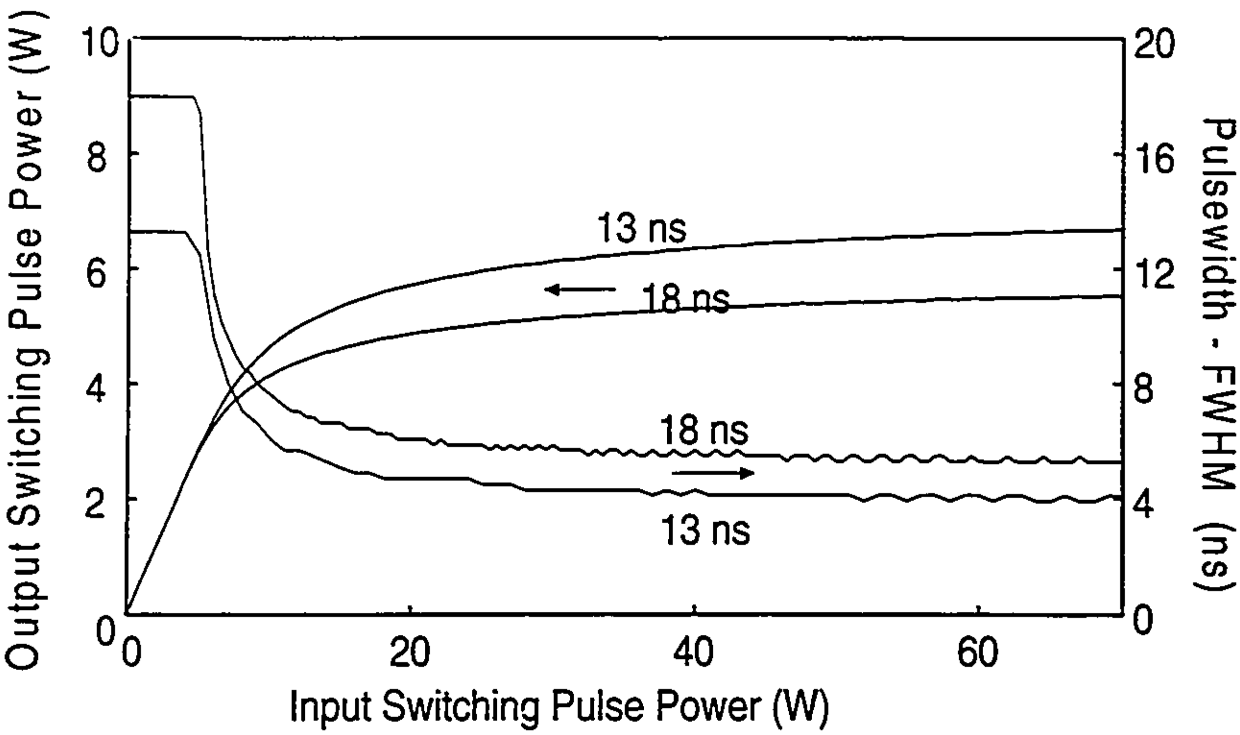

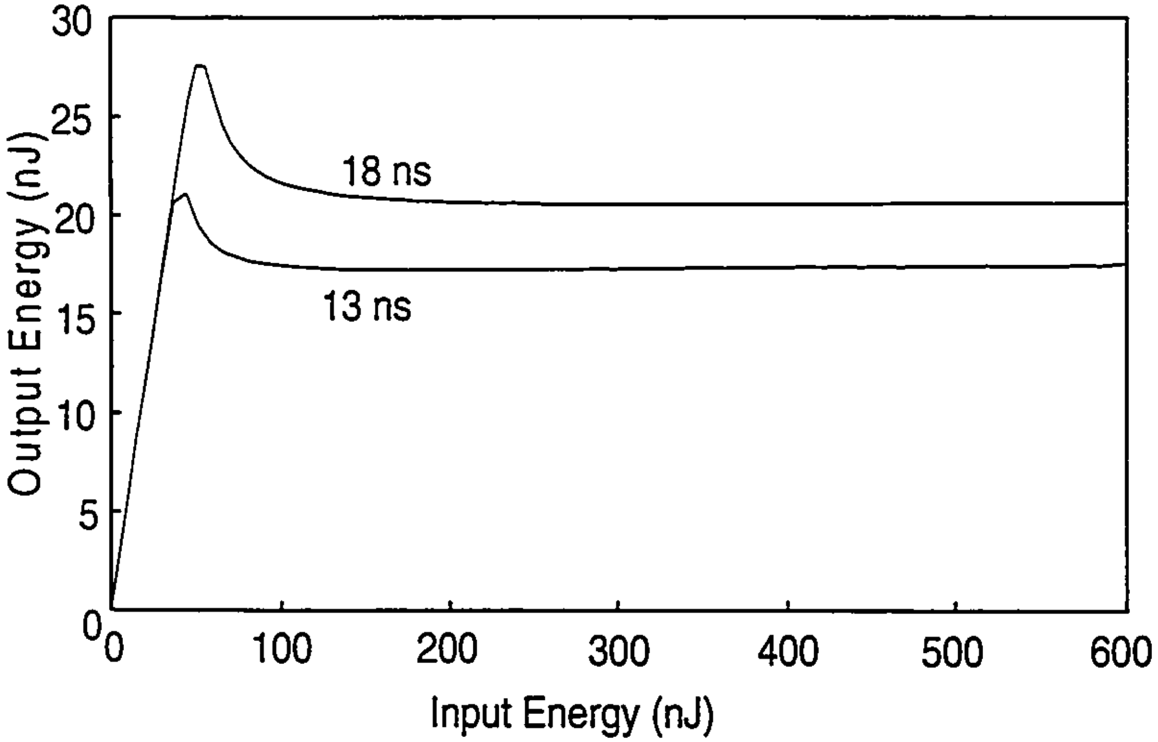

Fig. V.8. Theoretical output pump pulse power (top), pulsewidth (top), and energy (bottom) for 13 ns and 18 ns pulses transmitted through 12 km of fiber.

Stokes energy are indistinguishable at the detector. From the bottom curves of Fig. V.7, there is an optimum input power or energy for a given pulse width that maximizes the amount of energy transferred.

This conclusion is well supported by the theoretical results in Fig. V.8. Increasing the input power yields an increase in the output pump energy until the Raman threshold is reached. Further increasing the input power results in less output energy because of pump depletion. For higher input powers the depletion is complete, resulting in constant output energies. The theoretical result for different fiber lengths is shown in Fig. V.9. For shorter fibers the peak is more pronounced since the threshold occurs closer to the end of the fiber. Hence, Raman conversion is incomplete for a larger range of input powers.

The dependence of the maximum energy transfer on pulse duration and fiber length is shown in Fig. V.10. The curves in this figure were derived by finding, for a given length and pulse duration, the input power that maximized the output energy. The output power curves in the top of Fig. V.10 show that the optimum output peak power is independent of pulse duration for pulses longer than 1 ns. For longer pulses, the optimum input power is just below the SRS threshold, which is independent of pulse duration. Because of walkoff, pulses shorter than 1 ns are not fully depleted by Raman conversion so that higher peak powers can be transmitted. From section III.3, the degree of gain depletion in EDFA optical switching is determined by the switching pulse energy. For a required switching pulse energy there is a trade-off between the switching time and distance as illustrated by the optimized output energy curves in the middle of Fig. V.10. For example, if the remote EDFA requires 20 nJ of energy from a distance of 10 km, then the pulse duration, and hence switching time are limited to being greater than about 10 ns. More pulse energy can be transmitted by using longer pulses with peak powers below the Raman threshold. The bottom curves of Fig. V.10 show that the optimum energy transfer is independent of pulse duration.

V.3 Conclusions

This study has demonstrated two important limitations on the transmission of high power 1550 nm pulses over long single-mode fibers. First, the amount of energy or power that can be delivered within a given time is limited by SRS, regardless of the input power, and second there is an optimum input power that maximizes the energy delivered. Also, SRS generates a 100 nm red-

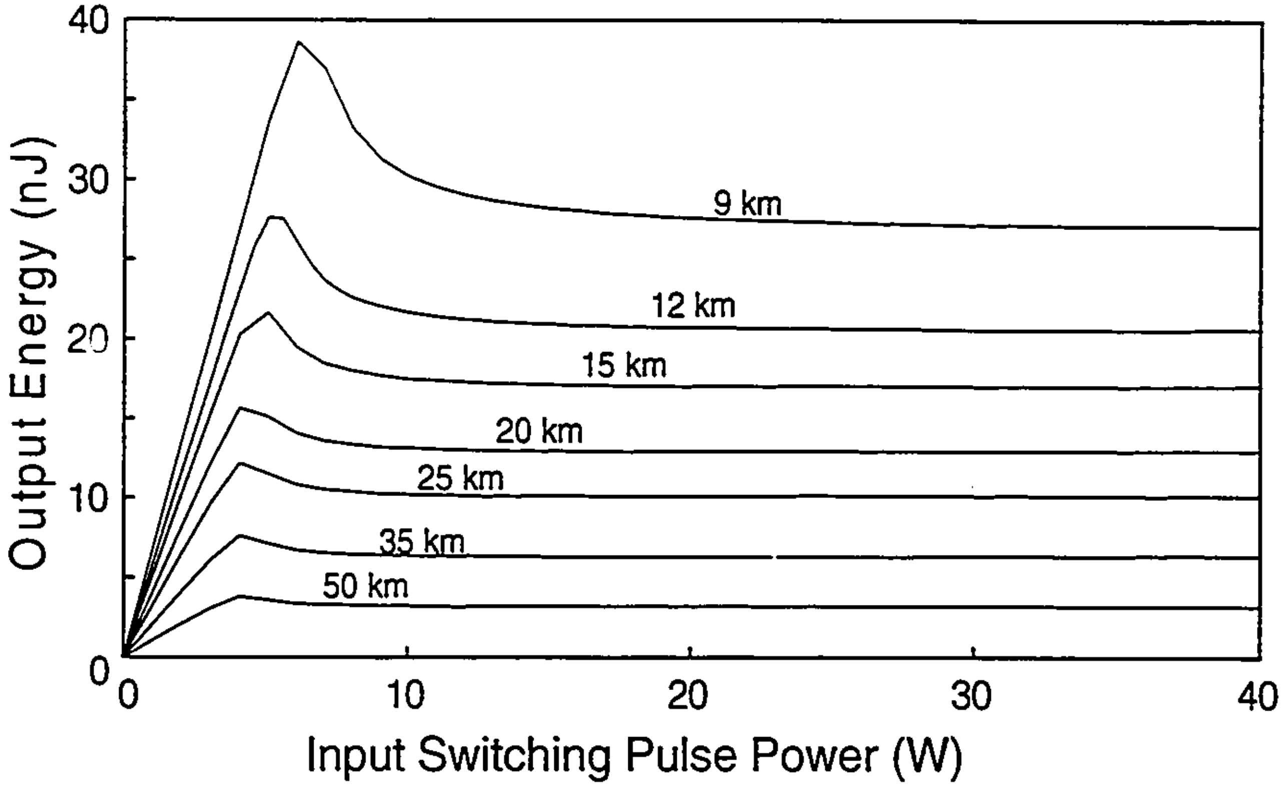

Fig. V.9. Theoretical output pulse energy vs input power for 18 ns input pulses.

shifted trailing pulse that can interfere with the detection of the input pulse depending on the application. For the remote EDFA switching application the Stokes pulse has negligible effect since it is outside of the EDFA bandwidth. To efficiently transmit a given amount of energy, the input power must be below the SRS threshold. Raman conversion can be avoided by using longer pulses which limits the switching time. The limitations are of interest not only for remote EDFA switching but other applications requiring the transmission of high-power 1.55 μm pulses over long distances such as for optically-powered remote switches [84]. There may be different requirements for transmitting high energy optical pulses to remote locations such as constraints on the delivered power, energy, or rise and fall times. For applications which require a certain peak power, SRS can be avoided by transmitting very short pulses. If a certain energy and rise time is required, the switching distance is limited or the degree of switching at a certain distance is limited by SRS.

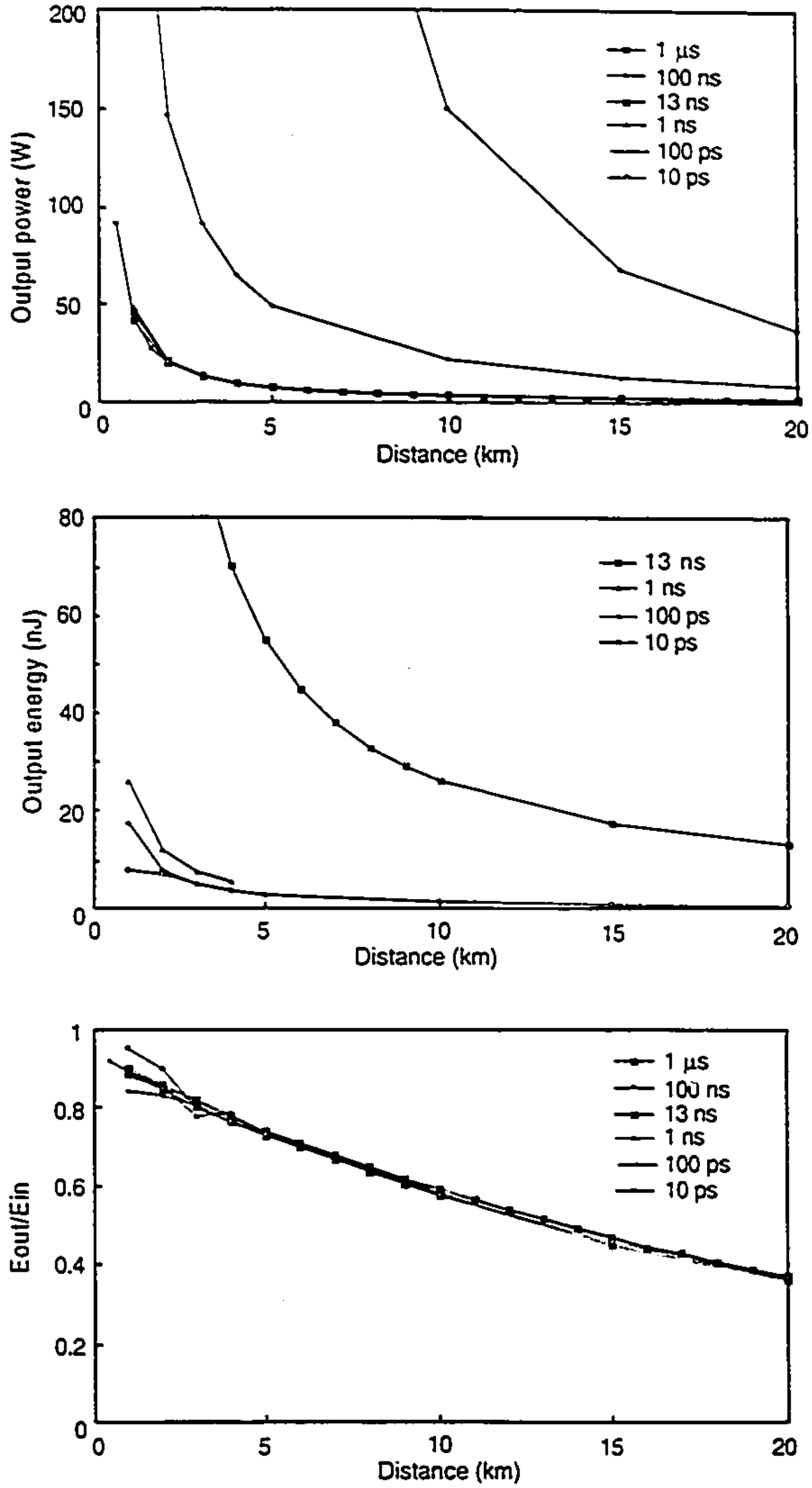

Fig. V.10. Optimum transmitted pulse power, energy, and energy efficiency.

Chapter VI

Bidirectional Fiber Amplifiers

VI.1 Introduction

Several methods of transmitting signals over optical fibers bidirectionally have been proposed [88], [89], [90]. Conversion of installed unidirectional systems to bidirectional operation can double the system capacity [91]. Bidirectional systems can operate in full duplex [91] or use time-compression multiplexing [92]. Proposed bidirectional systems include those that use wavelength division multiplexers to combine and separate counterpropagating signals which occupy different wavelength bands [89], and those that use standard wideband directional couplers to separate counterpropagating signals with arbitrary wavelengths [88]. The former method has the disadvantages that the transceiver pairs are different and the wavelengths are restricted. Although it is more versatile, the latter method has 6 dB excess loss and, in the presence of large received signal power, requires optical isolators after the laser transmitters. Recently, full-duplex and time-compression multiplexed transmission have been demonstrated with diode lasers operating as transmitter and receiver at each end [91], [90]. This method has fewer components but it can not be used for multichannel transmission. Polarization separation has also been demonstrated as a means of separating counterpropagating signals in a point-to-point bidirectional system [93] and as a means of multiplexing unidirectional signals [94]. Even in unidirectional transmission, bidirectionality is required for fault detection techniques such as optical time domain reflectometry (OTDR) [95] and autofiberbreak [96].

In a fiber transmission line containing EDFAs, optical isolators are typically used to prevent reflected light from damaging the lasers [97] and to prevent multiple reflections which can reduce the receiver sensitivity [98] (Fig. VI.1). For direct digital detection at a bit error rate of 10^{-9} the power penalty due to multiple reflection induced relative intensity noise is approximately [98]

$$\text{penalty} = -5\,\mathrm{Log}\left[1 - 144 R_{eff}^{2}\right] \tag{85}$$

where the effective reflectance, R_{eff}, equals $\sqrt{R^{+}R^{-}}\,/2$ for discrete reflections with intensity

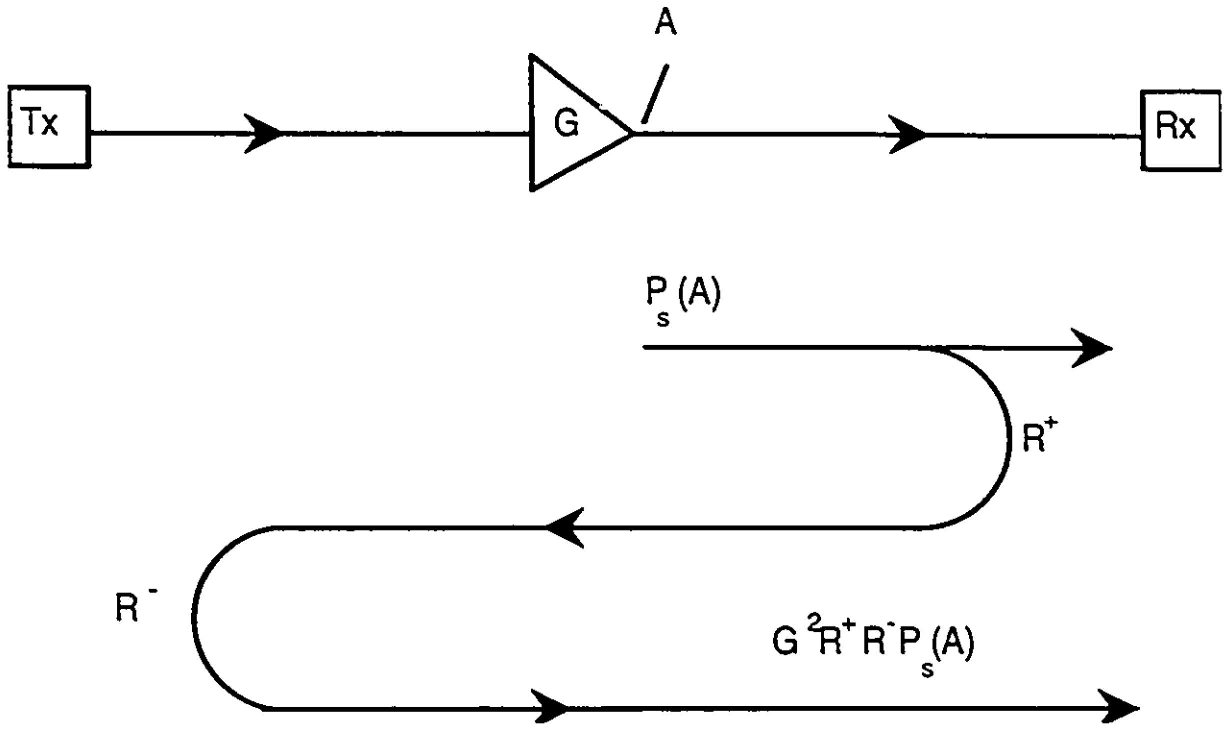

Fig. VI.1. Amplified multiple reflections causing relative intensity noise at the receiver.

reflection coefficients R^+ and R^-. For Rayleigh backscattering (RBS), $R_{eff}=R_{bs}/\sqrt{2}$ where R_{bs}= -32 dB for fibers longer than 20 km [99]. If an unisolated optical amplifier with gain G is located between the reflections, the effective reflectance increases to GR_{eff}. Thus, to limit the power penalty to less than 1 dB, reflections and RBS limit the gain to less than 20 dB without isolation for direct detection of digital signals and even less for photodetection of analog signals.

Since optical isolators only allow unidirectional propagation, they prevent the use of OTDR for fault location. In bidirectional networks, such as for interactive video, signals may be transmitted bidirectionally over a single fiber or two separate fibers. Transmitting bidirectionally over a single fiber can double the capacity of an installed unidirectional link. Whether one or two fibers is preferable for a bidirectional link depends on the particular system. This question is addressed in [100]. Optical isolators can not be used in single-fiber bidirectional networks such as reflective star coupler LAN's [101]. Thus a design is required that meets the apparent mutually exclusive requirements of reflection attenuation and bidirectional transmission. One proposed configuration modulates the pump laser diode for the second signal source [102]. Disadvantages of this approach are that the pump signal itself is not amplified, only unidirectional transmission is possible at 1.5 μm, and one set of receivers and transmitters is not at the same location. For OTDR testing a method has been proposed that uses optical circulators to direct the reflected light at each amplifier through a second fiber [103]. This requires a second installed fiber for the backscattered signal and two pump lasers at each amplifier, one being switchable remotely.

In this chapter alternative methods of sending bidirectional 1.5 μm signals over one fiber using EDFAs with optical isolation are proposed [104]. In Section 2 three types of bidirectional amplifier repeaters are proposed. At each repeater the counterpropagating signals are separated, amplified separately, and then recombined. Signal separation is done by fiber directional couplers, optical circulators, or wavelength selective couplers. The relative merits of the schemes are compared in terms of required pump light, isolation, noise performance, output saturation power, and cost. Alternatively, amplification can be separate from the filtering and isolating functions. These functions can be combined in newly proposed frequency dependent optical isolators described in Section 3. Experimental measurements are then reported in Section 4. In Section 5 a bidirectional amplifier using polarization signal separation is proposed for signals with orthogonal linear polarizations. Conclusions are then given in Section 6.

VI.2 Bidirectional Amplifiers for Single-Mode Fiber

Bidirectional-amplifier repeaters using directional couplers, optical circulators, and wavelength selective couplers (WSCs) are shown in Figs. VI.2, VI.3, and VI.4, respectively. Directional coupler signal separation incurs a 3 dB loss at each coupler so the net fiber-to-fiber gain, G_{net}, is one quarter of the internal gain. This loss can be eliminated by replacing the directional couplers and isolators with optical circulators [103] as shown in Fig. VI.3. Filtering and signal separation can also done with WSCs as shown in Fig. VI.4. In these configurations the top branches amplify light at wavelength λ_1, propagating from left to right and the bottom branches amplify light at wavelength λ_2, propagating from right to left.

Table VI.1 lists the coupling losses, effective reflectance, and required isolation η from (1) for a power penalty <1 dB assuming a net gain, G_{net}, of 25 dB and reflectance, R, of -30 dB. Also shown are the characteristics of amplifying counterpropagating signals in two separate fibers. In all cases the pump power is divided equally between the two erbium-doped fibers.

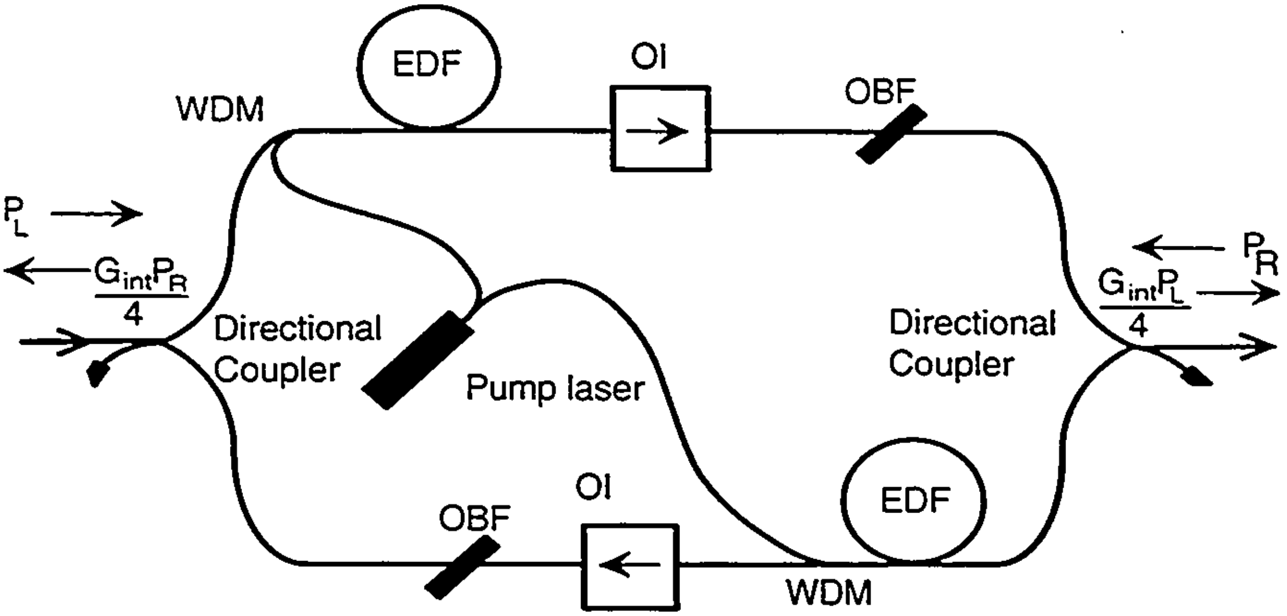

Fig. VI.2. Bidirectional optical amplifier with directional coupler signal separation. OBF is an optical bandpass filter.

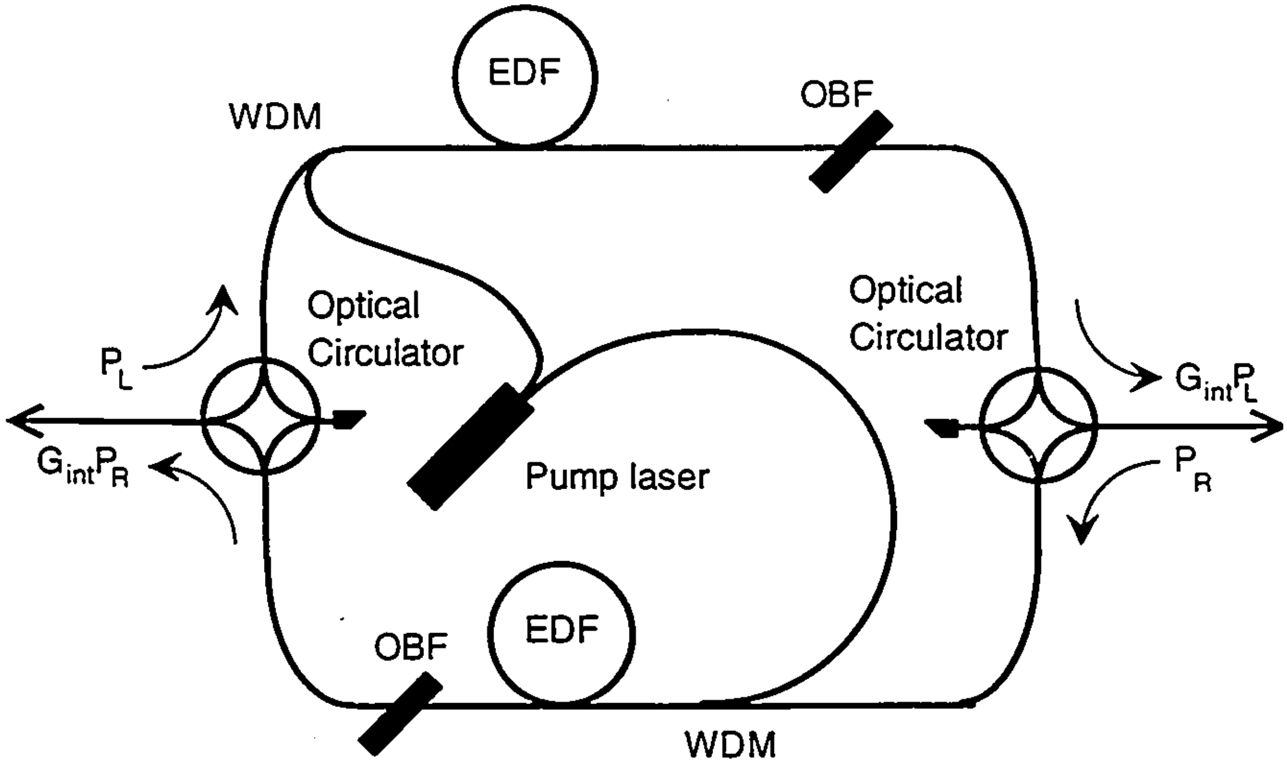

Fig. VI.3. Bidirectional optical amplifier with optical circulator signal separation.

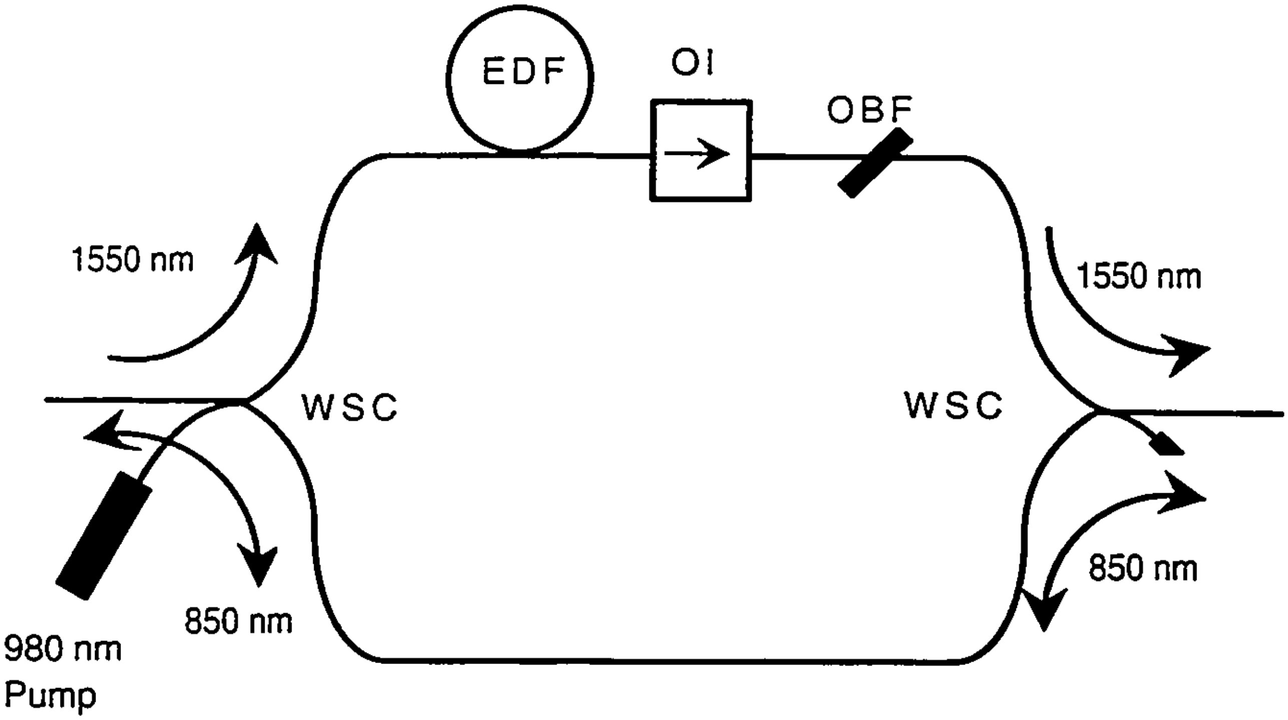

Fig. VI.4. Bidirectional optical amplifier with wavelength selective coupler (WSC) signal separation for OTDR testing.

In the first two configurations reflected light from the left is amplified by the top branch and reflected light from the right is amplified by the bottom branch, so multiple reflections are not eliminated except for certain cases. Multiple reflections can be reduced by assigning non-overlapping optical bands to the two directions. The isolation is provided by the narrow band-pass optical filters in Figs. VI. 2 and VI. 3 and the WSCs in Fig. VI.4. The required filter extinction coefficient η, calculated from (1), is shown in Fig. VI.5 as a function of the product of the net gain and reflectance. The required tunable filters and narrow-band WSCs based on multilayer dielectric filters are commercially available. Low-loss filtering with extinction greater than 95% (13 dB) can also be achieved by depositing dielectric films on bevelled fiber end faces [105].

For OTDR, a wavelength can be used where neither filter or WSC has 100% extinction. For OTDR testing of unidirectional networks the configurations can be simplified as follows: in Fig. VI.2 and VI.3 only one band-pass filter is required to attenuate the backreflected signal light and transmit the reflected OTDR pulses. In Fig. VI.4 only one isolator is required to attenuate the reflected signals.

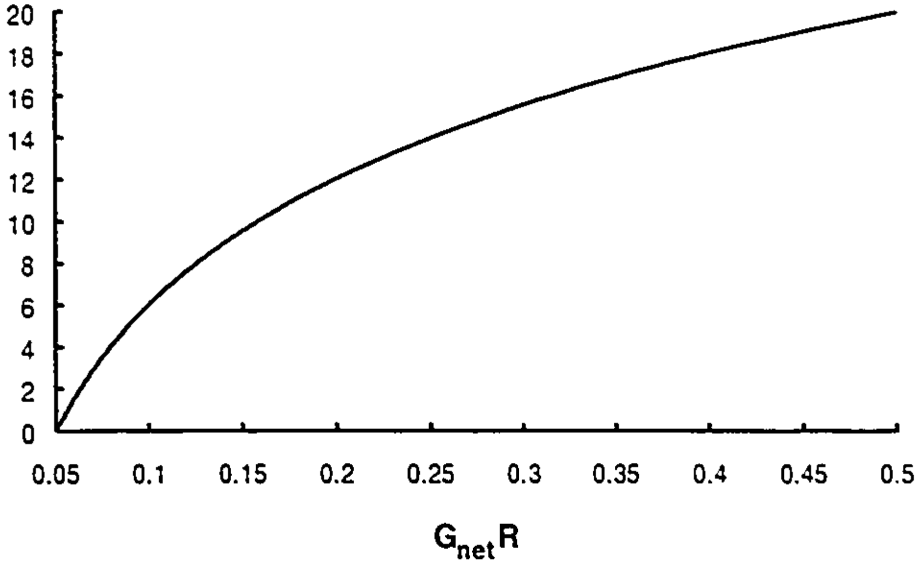

Fig. VI.5. Required filter extinction coefficient versus the product of the net gain and reflectance.

For directional coupler signal separation and small signal amplification, the 6 dB coupling losses can be overcome with a few extra milliwatts of pump power. This is shown quantitatively in Fig. VI.6 which shows the net gain for each module as a function of the total pump power. These curves were calculated using the model given in [53] to calculate, at each pump power value, the fiber length giving maximum internal gain. The parameters used were $\lambda_p = 1.48$ μm, $\lambda_s = 1.55$ μm, $\alpha_s = 2.6$ dB/m, $\alpha_p = 1.6$ dB/m, $P_p^{IS} = 0.430$ mW, $P_s^{IS} = 0.139$ mW, with -30 dBm input signal power. For output powers less than 0 dBm, the directional coupler repeater only requires 1-3 mW more pump power than the optical circulator and WSC repeaters to achieve the same gain. In the saturated regime, the output power is directly proportional to the pump power so the pump power must be 3 dB higher to compensate for the output coupling loss, as indicated in Fig. VI.6. Recall from Section III.4.2 that the optical amplifier noise figure is directly proportional to the input coupling efficiency and only weakly dependent on the output efficiency. Therefore, the minimum noise figure of the optical circulator and WSC configurations is 3 dB plus the component insertion loss whereas the directional coupler configuration noise figure has a 6 dB minimum.

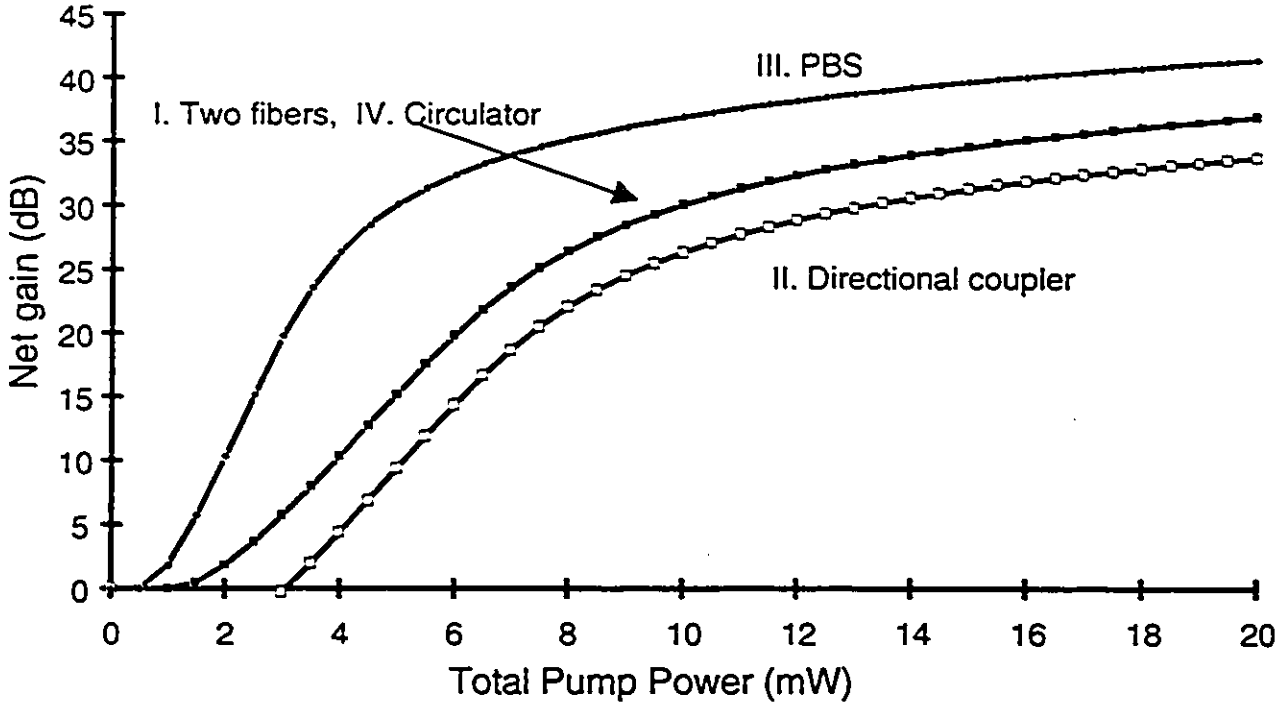

Fig. VI.6. Comparison of the net gain vs total pump power required for the fiber amplifiers.

Configuration	P_p/direction	Input loss (dB)	Output loss (dB)	Effective reflectance $2R_{eff}$	η (dB) (G_{net}=25 dB, R=-30 dB)
Two fibers	$P_p/2$	0	0	$G_{net}R\sqrt{\eta_i}$ 1 iso. $G_{net}R\eta_i$ 2 iso.	10 5
Dir. coupler	$P_p/2$	3	3	$G_{net}R\sqrt{\eta_f}$	10
Circulator, WSC	$P_p/2$	0	0	$G_{net}R\sqrt{\eta_f}$	10
PBS	P_p	0 (Correct pol.)	0	$2\sqrt{(G_{net}R\eta_f)}$	20

Table VI.1 Comparison of bidirectional amplifiers. η_i, and η_f are the extinction ratios of the optical isolator, and the filter and WSC, respectively.

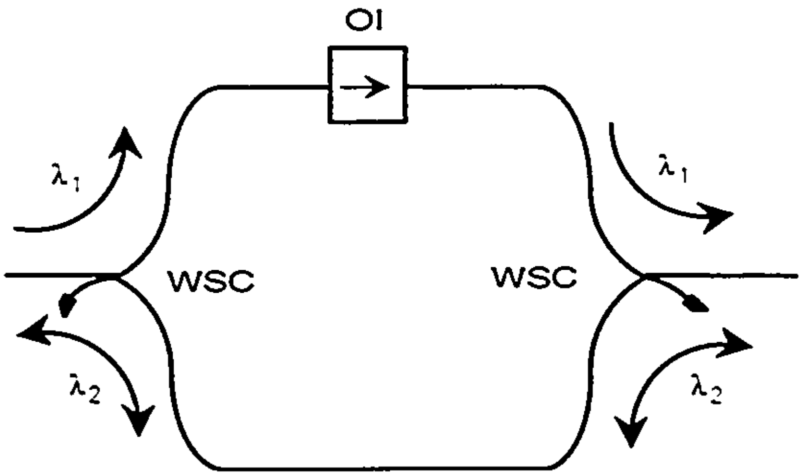

Fig. VI.7. Frequency dependent optical isolator with wavelength selective coupler (WSC) signal separation.

VI. 3 Frequency Dependent Optical Isolators

In the previous section bidirectional fiber amplifiers were described where EDFAs were combined with frequency dependent optical isolators. Alternatively, the amplifier can be removed, resulting in a frequency dependent optical isolator [106]. Frequency dependent optical isolators have the same design as the bidirectional amplifiers in Figs. VI. 2-4, but with the amplifiers removed. For example, a frequency dependent optical isolator using WSCs for OTDR testing of a unidirectional link is shown in Fig. VI.7. The function of this frequency dependent isolator is to allow signal light to propagate from left to right, but not from right to left, and to allow OTDR pulses to propagate in both directions. For bidirectional networks a second isolator can be inserted in the bottom branch to prevent reverse transmission of the signal propagating from right to left. Separating the frequency dependent isolator from the amplifier has the advantage that pump light is not shared between two doped fibers. The experimental demonstration of these devices is described in the next section.

VI.4 Experiments

Two frequency dependent optical isolators (FDOIs) and bidirectional fiber amplifiers were constructed using WSCs or directional couplers. The gain and noise were measured for different amplifier locations with respect to the FDOI. The EDFA with 10 m of fiber described in Section II.6 was used with 1542 and 1525 nm signals. With -20 dBm input power at 1542 nm, its gain was 23 dB. The forward ASE peak is about 15 dB below the output without optical filtering and 40 dB below the output with filtering.

The first FDOI configuration, shown in Fig. IV.7, was made with two 980/1550 nm WSCs to guide the 1550 nm signal in one direction through the top branch and to guide 850 nm OTDR pulses in both directions through the bottom branch. OTDR currently has a higher dynamic range at 850 nm than at 1550 nm because the pulsed laser is more powerful and the detector is more sensitive at 850 nm. Although erbium-doped fiber is relatively transparent at 850 nm, this light is strongly attenuated by an EDFA because it is coupled out by the pump coupler and attenuated by the 1550 nm wavelength-dependent isolators. The bidirectional amplifier in Fig. IV.4 solves this problem by guiding the OTDR pulses around the amplifier. Fig. IV.8 shows the transmission spectra for the FDOI shown in Fig. VI.7. At 1550 nm, the forwards insertion loss is 4 dB, and the backwards attenuation is greater than 35 dB. In both directions the 850 nm insertion loss is 8 dB. This loss can be decreased by using couplers designed for 850 nm rather than 980 nm. With the amplifier in the FDOI as in Fig. VI.4, the small-signal gain at 1542 nm was 18 dB with an ASE peak 15 dB below

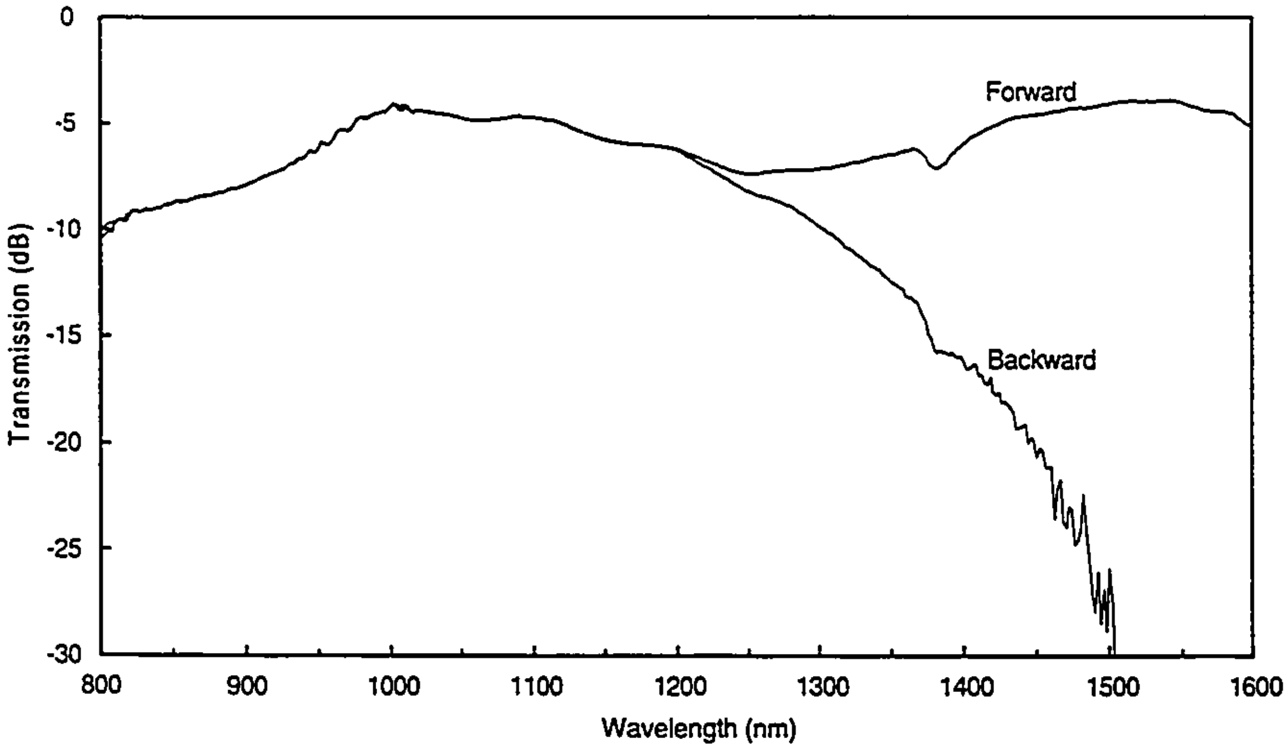

Fig. VI.8. Transmission spectra of frequency dependent optical isolator with wavelength selective couplers for OTDR testing.

the signal.

An FDOI was also made with two directional couplers and two filters for 1525 and 1542 nm, similar to the scheme in Fig. VI.2 without the fiber amplifiers. Its transmission spectrum is shown in Fig. VI. 9. The insertion loss in each direction is about 10 dB, comprising 6 dB coupling loss, and 4 dB insertion loss from the couplers, filters, isolators, splices, and connectors. In each direction the attenuation of the reverse signal band is greater than 30 dB.

The gain and noise were measured using the FDOI configured for 1542 and 1525 nm. With the amplifier before the FDOI the small-signal gain at 1542 nm was 12 dB, and the ASE peak was 40 dB below the output. This forward gain decreased by 1.5 dB with -11 dBm input at 1525 nm in the reverse direction. With the amplifier after the FDOI the gain decreased to 9 dB, and the ASE peak was only 7 dB below the output. This gain decreased by 3 dB with the 1525 nm light in the reverse direction. In this case the FDOI insertion loss reduces the amplifier input power so much that its output is almost lost in the noise background. The signal-to-noise ratio is greater for more powerful

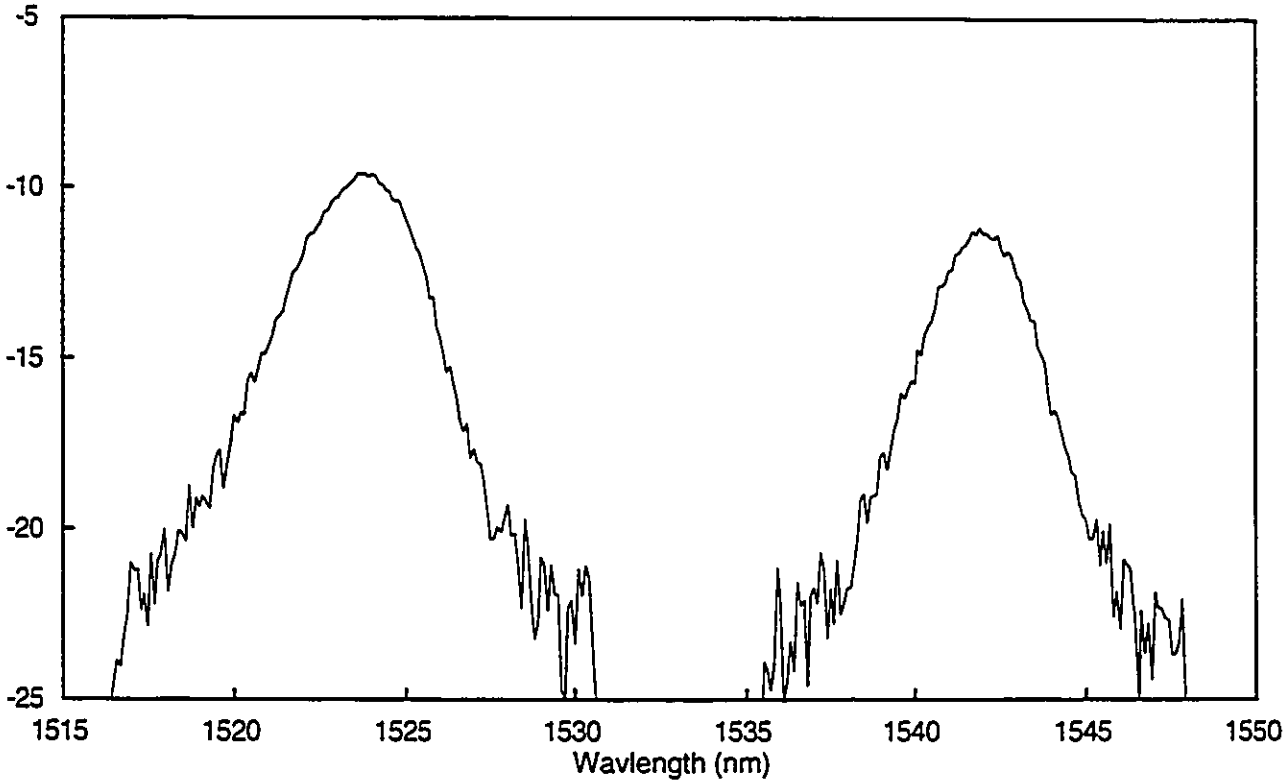

Fig. VI.9. Transmission spectra of frequency dependent optical isolator with directional couplers for bidirectional transmission.

input powers, but with reduced gain. For example, -9 dBm input had a net gain of 7 dB and an ASE peak 20 dB below the signal. With the amplifer in the 1542 nm branch of the FDOI, as in Fig. VI.2, the gain was 13.5 dB and the ASE peak was 37 dB below the output. Because of the optical isolator, the 1525 nm backwards light did not affect the amplifier performance.

The attenuation of light reflected back into each bidirectional amplifier was also compared to the reflection attenuation of the standard EDFA with no isolators. The input power was -20 dBm at 1542 nm. The spectrum of the light emitted from the input port was measured with no reflection after the output port and compared to the spectrum with a 4% (-14dB) reflection after the output port. Fig. IV.10 shows the spectra for the EDFA with no isolators. When there is no reflection, the backwards ASE was dominant with a peak of -16 dBm. With the reflection, the backwards signal power increased by 23 dB to 3 dB, only 1 dB less than the output power.

The reflection attenuation for the bidirectional amplifier with WSCs (Fig. VI.4) was measured for different isolator locations. For no isolator and no reflection, the backwards ASE was dominant with a peak of -18 dBm. With the reflection, the backwards signal power increased to -9 dB. With

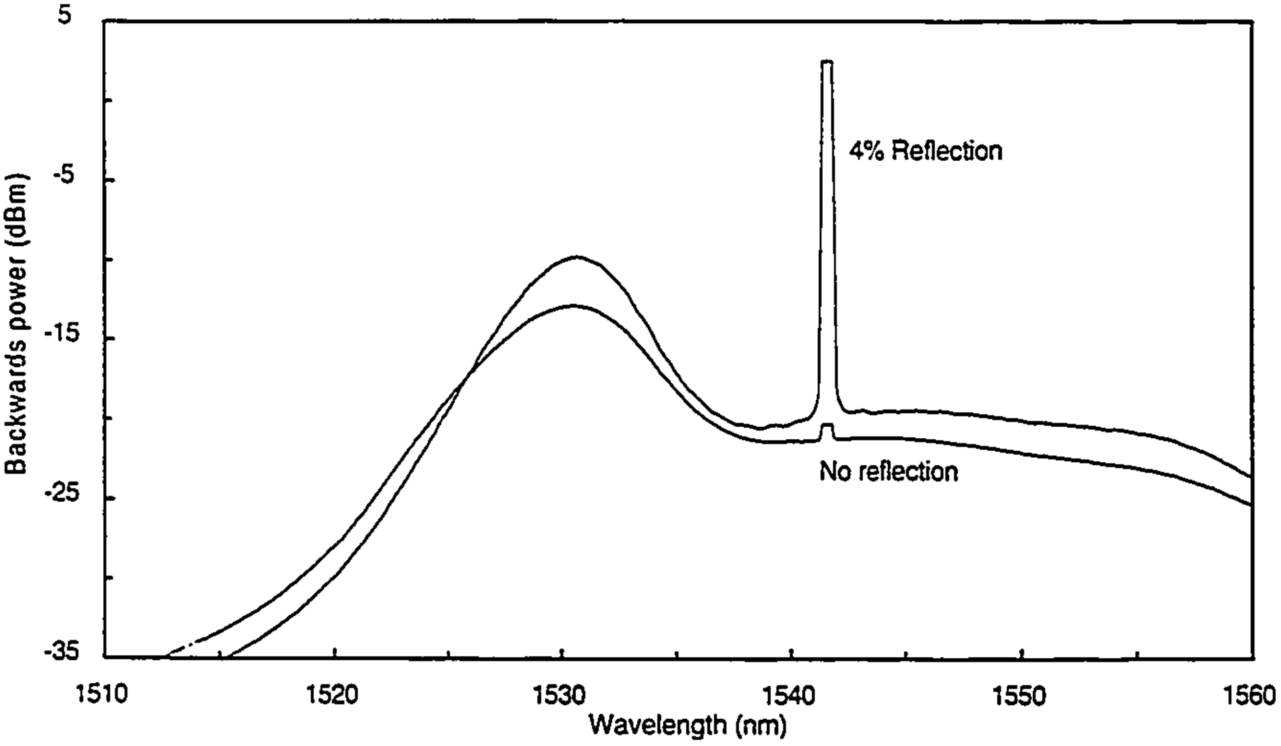

Fig. VI.10. Backwards spectra from EDFA with no output reflection and 4% output reflection.

an isolator after the EDFA, the ASE dominant spectrum was the same for the reflection and no reflection cases. Locating the isolator before the amplifier required an extra pump WSC, resulting in a 2.5 dB gain reduction. Without reflection the backwards signal power was -55 dBm, 2 dB above the ASE peak, and with reflection the backwards signal power was -44 dBm.

The reflection attenuation for the bidirectional amplifier with directional couplers (Fig. VI.2) was also measured for different isolator locations with the EDFA in the 1542 nm signal branch. For no isolator and no reflection the backwards ASE was dominant with a peak of -23 dBm. With the reflection, the backwards signal power increased to -14 dB. With the isolator after the EDFA, the ASE dominant spectrum was the same for the reflection and no reflection cases. With the isolator before the amplifier and no reflection, the backwards ASE was dominant with a peak of -61 dBm. With the reflection the backwards signal power increased to -50 dBm.

VI.5 Conclusions

Several designs of bidirectional fiber amplifiers have been proposed. For full-duplex transmission over single-mode fibers with strong reflection isolation separate wavelength bands must be assigned to the opposite directions and narrow bandpass, low-loss filters with extinction coefficients greater than 90% are required. Although the optical circulator repeater offers a better performance, an optical circulator presently costs more than twice as much as the optical isolator and the directional coupler it replaces. Also, the insertion loss of a circulator is about 1 dB greater than that of an isolator. WSC repeaters also offer better performance than directional coupler repeaters, but at a higher cost. The lower component cost for the directional coupler module must be weighed against its lower saturation output power, higher noise figure, and larger pump power.

As demonstrated experimentally, the amplifier can also be separately located from the frequency dependent isolator. This configuration has the advantage that pump light is not shared between the two doped fibers. Compared to a standard EDFA, the insertion losses of the extra components in the bidirectional amplifiers reduce the gain and signal-to-noise ratio. However, the bidirectional fiber amplifiers satisfy their design criterion in that they are much better at attenuating reflected light.

Chapter VII

Polarization Separated Bidirectional Fiber Networks

VII.1 Introduction

Many proposed architectures of bidirectional optical local-area networks (LAN's) are based on transmissive or reflective star couplers. When a transmissive star coupler serves as the central node each user is connected by two fibers, one for transmission and one for reception. A reflective star coupler network requires a smaller amount of fiber and cascaded directional couplers than a transmissive star [101]. In this implementation each of the users is connected by a single-fiber to the star which reflects an equal fraction of light entering from any fiber to all other fibers. In a reflective star coupler network the counterpropagating transmitted and reflected signals must be separated at each transceiver. If directional couplers are used, optical isolators may be required after each laser for protection from the received light. Although wavelength separation can be used in point-to-point bidirectional links, it is impractical for bidirectional LAN's. Recently, polarization separation has been demonstrated as a means of multiplexing unidirectional signals [94] and as a means of separating bidirectional signals in a point-to-point link [93]. In this chapter, a new method is proposed in which bidirectional signals in a reflective star LAN are separated by allocating orthogonal polarizations to the two directions and transmitting over polarization maintaining fiber (PMF). This method theoretically directs all incident light towards the receivers.

After discussing the transceiver configuration, the novel fiber devices based on an orthogonal polarization variable reflector are introduced. Reflective polarization separated star LAN's are then proposed using a 4-star as an example. A fiber amplifier configuration is then described for polarization separated bidirectional networks. The chapter concludes with a discussion of some of the limiting factors imposed by polarization separation.

The proposed transceiver is shown in Fig. VII.1. A fiber polarizing beam splitter (PBS) selects the x polarized component of the signal laser light for transmission and the y polarized component is radiated out at the index-matched terminator. The y polarized components of the incoming signals are sent to the receiver and the x polarized component is directed towards the laser. Optical isolation is unnecessary assuming negligible polarization conversion and negligible backscattered and reflected

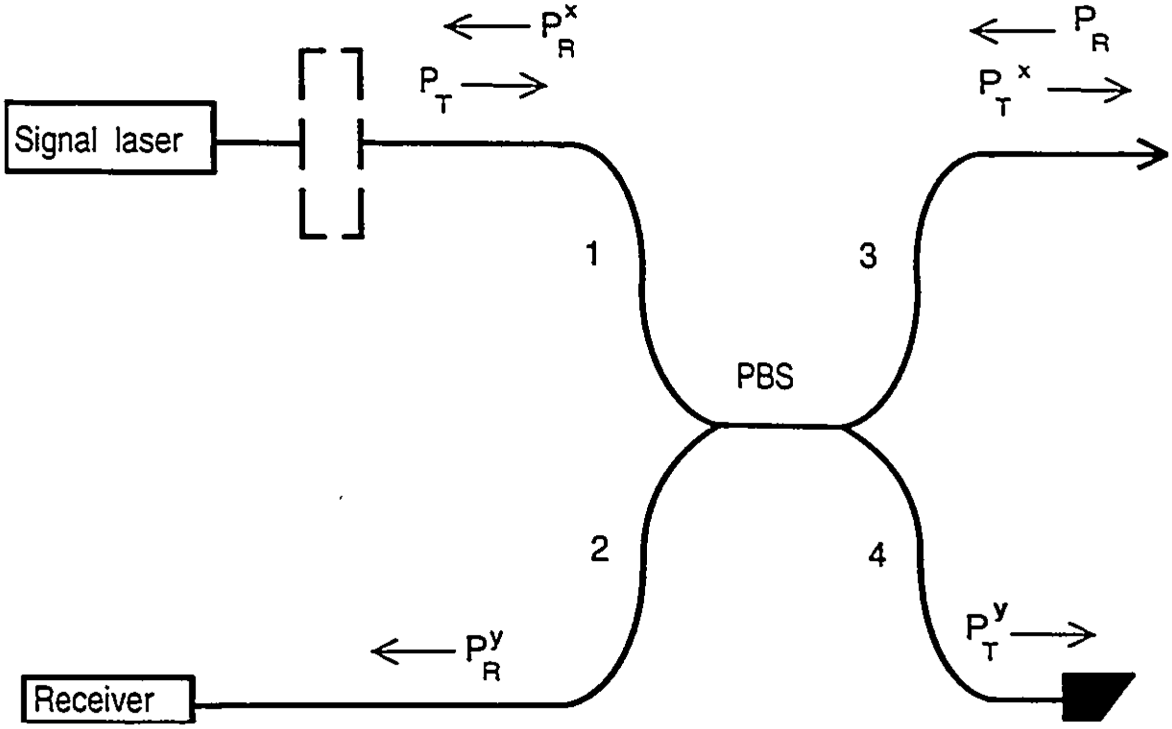

Fig. VII.1 Polarization separated bidirectional transceiver using a fiber polarization beam splitter (PBS).

light. If required, an optical isolator or a fiber polarizer may be inserted in the dashed box to prevent light from entering the laser. This transceiver differs from that shown in Ref. [93] in that a PBS is used instead of a polarization maintaining 3 dB coupler, thus obviating fiber polarizers in front of the receiver. In a point-to-point link one transmitter can be assigned the x polarization and the other can be assigned the y polarization as in [93]. For a LAN, it is simplest if the transceivers are identical. This is realized by connecting the transceivers with a splice that has a 90° rotation of the polarization axes. With this splice, both lasers transmit the same polarization and receive the orthogonal polarization.

VII.2 Polarization Separation Components

The necessary components for polarization separated reflective star coupler networks are now introduced. These are based on a proposed orthogonal polarization variable reflector (OPVR), shown in Fig. VII.2, consisting of a fiber PBS with the output fibers joined with the axes rotated by an angle θ. Jones calculus gives an analytical description of the device's polarization characteristics. To describe the polarization state in a bidirectional configuration, the coordinate system is fixed with the fiber fast and slow axes. A fiber splice with a rotation of angle θ acts as a polarization rotator with a Jones matrix:

$$J_r = \begin{bmatrix} \cos\theta & \sin\theta \\ -\sin\theta & \cos\theta \end{bmatrix} \tag{86}$$

In the reverse direction, the Jones matrix is given by the transverse of J_r. The net effect of the PBS is given by the sum of the multiplication of separate Jones vectors and matrices for each port. For example, if the ports are labelled as in Fig. VII.1 then the polarization at the output port 3 is given by

$$E_3 = \begin{bmatrix} 1 & 0 \\ 0 & 0 \end{bmatrix} E_1 + \begin{bmatrix} 0 & 0 \\ 0 & -j \end{bmatrix} E_2 \tag{87}$$

A π/2 phase shift is assumed between the two output ports. By successively applying the matrices

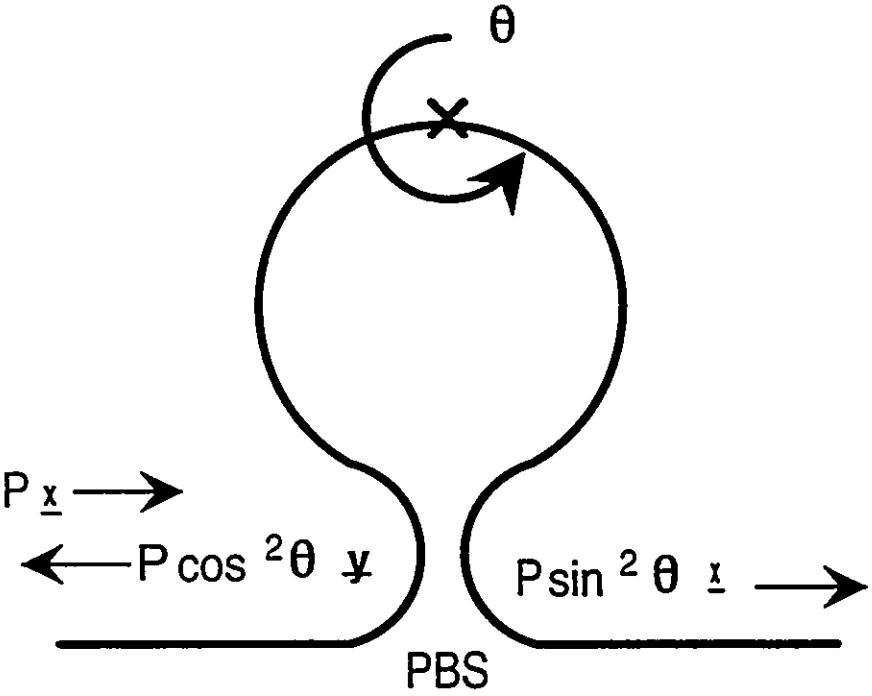

Fig. VII.2. Fiber orthogonal polarization variable reflector of Eqs. (86) and (87) the Jones matrix for an OPVR is found (for light incident from the left as in Fig. VII.1):

$$\begin{aligned} E_1^{out} &= \begin{bmatrix} 0 & j\sin\theta \\ j\sin\theta & 0 \end{bmatrix} E_1^{in} \\ E_2^{out} &= \begin{bmatrix} \cos\theta & 0 \\ 0 & -\cos\theta \end{bmatrix} E_1^{in} \end{aligned} \tag{88}$$

Thus $\cos^2\theta$ of the light is transmitted in the initial polarization and $\sin^2\theta$ is reflected in the orthogonal polarization.

When $\theta = 90°$, the device acts as an orthogonal polarization full reflector (OPFR) which has a resultant Jones matrix identical to that of a Faraday rotating mirror [107]. In a fiber terminated by an OPFR the returning polarization state is always orthogonal to the entrance state, even when non-polarization preserving fiber is used. Applications of the OPFR are eliminating the polarization dependence of non-polarization maintaining fiber Michelson interferometers [107] and to prevent polarization instability in fiber Kerr switches [108]. When $\theta = 45°$, the device acts as an orthogonal polarization half reflector (OPHR). This device reflects half the incident light in the orthogonal polarization and transmits half the incident light in the initial polarization.

VII.3 Polarization Separated Reflective Star Networks

The OPFR, OPHR, and polarization maintaining directional couplers (PMDC) make up all the necessary components for a polarization separated reflective N-star coupler network where $N=M^2$ or $2M^2$ [101]. Fig. VII.3 gives an example of a 4-star reflective network using polarization separation. One quarter of the power of the top transmitter is transmitted to each receiver with polarization orthogonal to the transmitted polarization. A reflective N-star where $N=M^2$ can be constructed by interconnecting MXM star couplers with an OPFR at one output of each MXM star and a 90° splice connecting the outputs of a star to the other stars (cf. Fig. 9 of [101]). Reflective N-stars with $N=2M^2$ can be constructed with OPHR's replacing the reflective 2-stars and 90° splice connecting the MXM stars to the 2X2 stars (c.f. Fig. 13 of [101]). In fact, the OPHR is an example of a reflective 2-star with polarization separation. All of these interconnection methods satisfy the multipath-free

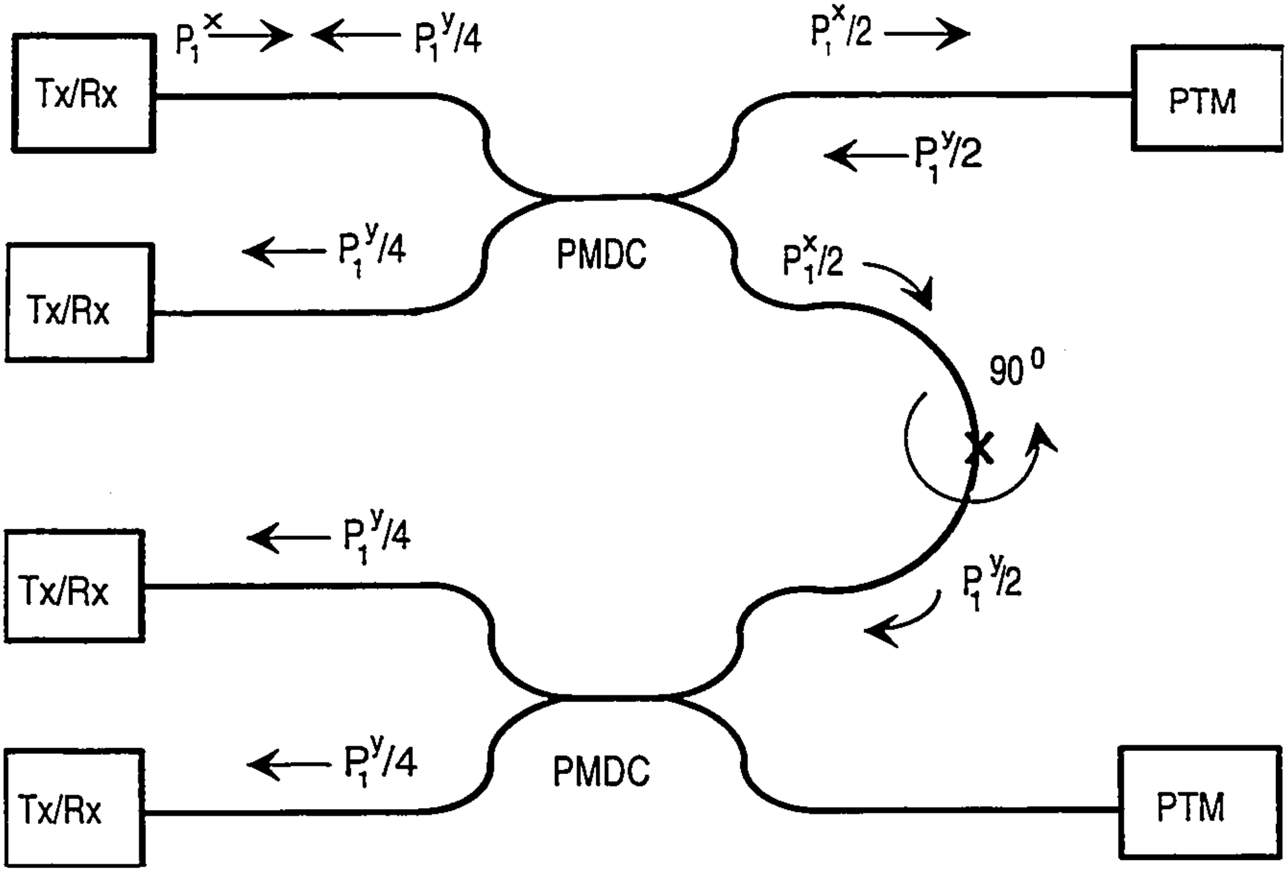

Fig. VII.3 4X4 polarization separated reflective star coupler network using two polarization maintaining directional couplers (PMDC), two orthogonal polarization reflectors (OPR) and a 90° splice.

requirement of reflective star networks provided that the polarization state is preserved.

VII.4 Bidirectional Optical Amplifiers for Polarization Separated Signals

In large LANs optical amplifiers may be required to compensate the splitting losses. High-gain optical amplifiers require optical isolation which makes their use difficult in bidirectional networks [98]. However, optical amplifiers are easily added to polarization separated bidirectional systems even with optical isolators. Fig. VII.4 illustrates how an in-line erbium doped fiber amplifier can amplify counterpropagating, orthogonally-polarized signals with no excess loss [109]. An optical isolator may be inserted as shown to eliminate the signal components in the incorrect polarization, and to prevent backscattered and reflected light from entering the fiber amplifier. Note that the erbium doped fiber must be polarization preserving. In this configuration only the x polarized

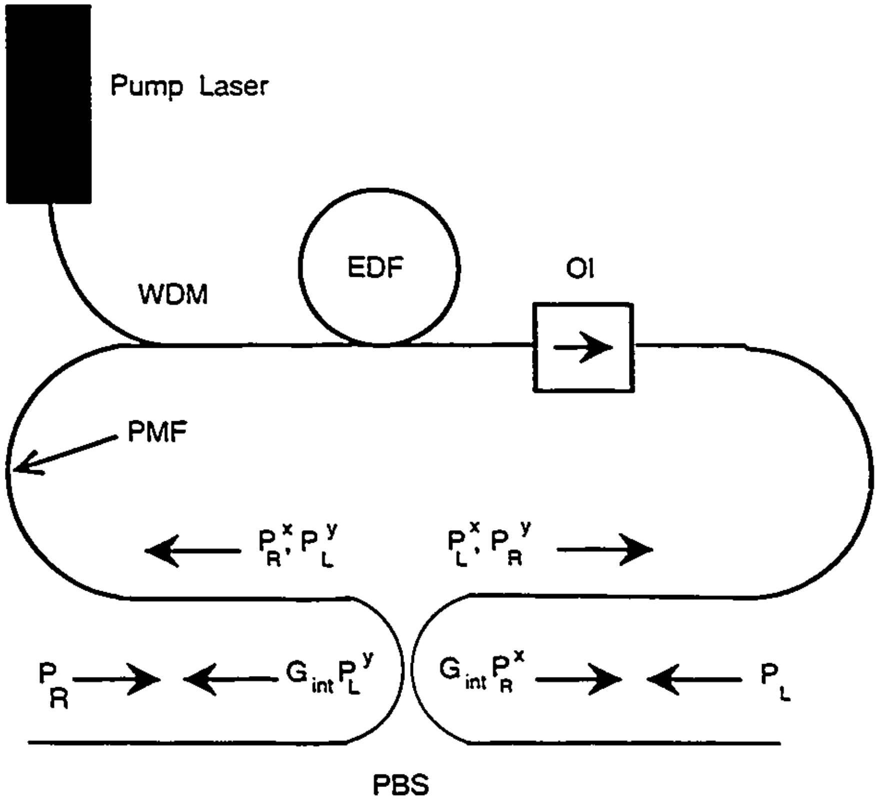

Fig. VII.4 Bidirectional optical amplifier with fiber polarization beam splitter (PBS) signal separation.

component of the right propagating signal and the y polarized component of the left propagating signal are amplified. This bidirectional amplifier, with only one WDM, doped fiber, isolator, multiplexer, and no optical filter, has fewer components than the single-mode fiber amplifiers described in Chapter VI. This configuration makes more efficient use of the pump light since the total pump power is shared by the counterpropagating signals. It thus has a larger saturation output power than the single-mode fiber configurations. Since polarization is maintained during reflection and backscattering, the degree of backreflection attenuation depends mainly on the extent of polarization conversion in the fiber and the polarization isolation of the fiber PBS. These are typically greater than 25 dB [110], [111], which is greater than the limit given in Table VI.1

VII.5 Discussion

The network performance depends critically on the degree of polarization isolation. A fraction of the transmitted signal is directed towards the opposite lasers because of sub-100% laser polarization isolation, imperfect laser/PMF coupling, and sub-optimum PBS isolation. Typically, a fiber PBS has an isolation in excess of 25 dB. Polarization coupling in the PMF also results in light being directed towards the lasers. The degree of polarization coupling depends on the fiber length, transverse stress, and the radii of the fiber bends [110]. The latter two factors are negligible if all bend radii are less than 10 cm and a thick cladding and jacket are used to reduce transverse stress. Assuming x polarized light at 1.55 μm is transmitted over a PANDA fiber (a common type of PMF [110]), after a distance L the power in the orthogonal polarizations is given by

$$P_R^y = P_T^x e^{-\alpha L} \tanh(hL) \tag{89}$$

where α, the loss coefficient, is ≈ 0.06 km^{-1} (0.25 dB/km) and h, the polarization coupling parameter, is ≈ $0.5\mathrm{X}10^{-3}$/km [110]. Assuming a PBS isolation of 25 dB, the power incident on the laser is limited by PBS isolation for distances less than ≈ 6 km and limited by polarization transformation for distances greater than ≈ 6 km. Thus, with proper connections the fraction of power lost due to polarization conversion is less than ≈ 25 dB.

In summary, polarization separated bidirectional fiber networks are proposed. This technique can transmit WDM signals in both direction with no theoretical excess loss. With all-fiber components, polarization separation can be used for both point-to-point and reflective N-star coupler networks where $N = M^2$ or $2M^2$. A bidirectional fiber amplifier for polarization maintaining fiber is also proposed [109]. It attenuates backreflected light and has no theoretical excess loss.

Chapter VIII

Summary and Suggestions for Future Work

In Chapter II an analytical model was presented for rare-earth-doped fiber amplifiers and lasers [44]. Fiber amplifier gain was expressed in terms of system-independent parameters determined from one-beam and two-beam transmission measurements. System-independent formulas were given for the slopes and thresholds of ring and linear fiber lasers. Good agreement between theory and experiment was shown for erbium-doped fiber amplifiers and lasers and thulium-doped fiber lasers. This is the first model that gives ion-independent, closed-form expressions for fiber amplifiers and lasers. It is envisaged that this model will provide a basis for future work in the rapidly developing field of rare-earth-doped fiber lasers and amplifiers [31], [21]. Although this model is applicable to all rare-earth dopants, it was verified experimentally for only erbium-doped amplifiers and lasers and thulium-doped fiber lasers [48]. Therefore, measurements should be done for the other dopants such as neodymium and praseodymium.

Approximate system-independent solutions were also given for fiber amplifiers with excited state absorption at either the pump or signal wavelengths. From this analysis a new technique, requiring only one tunable light source, was proposed for finding the best amplifier pump wavelength when pump ESA is present. This is particularly applicable to pumping erbium at 800 nm, since high-power, low-cost laser diodes are available in that region. This technique still requires an experimental demonstration. The three- and four-level models predict a flattening of the fiber laser slope at higher pumping powers when the fiber is shorter than the optimum length. This effect has yet to be observed since high-power lasers with short fibers have not been measured.

In Chapter III a simple approximate expression for the EDFA amplified spontaneous emission noise bandwidth as a function of the amplifier gain was derived. In contrast with the common assumption of constant bandwidth, it was experimentally shown that the noise bandwidth decreases as the gain increases. A simple approximate expression for the EDFA spontaneous emission factor as a function of the amplifier gain was also derived. This expression enables easy prediction of the amplifier signal-to-noise ratio (SNR). By taking the derivative of the SNR along the fiber length, an alternative expression for the optimum EDFA fiber length was obtained. This is preferable to the usual technique of selecting the fiber length to maximize the gain, because maximum gain does not give maximum SNR. The expression gives good results when signal-spontaneous noise is dominant but requires further refinement when optical filtering does not adequately reduce the spontaneous-spontaneous beat noise.

Remote, all-optical gain switching of EDFAs with short pulses at wavelengths within the amplifier bandwidth was modelled in Chapter IV to determine how the pump and signal powers, pulse energy, fiber length, and dopant concentration affect the switching time and gain compression [81]. Greater than 20 dB gain compression with nanosecond switching times was demonstrated with good agreement between theory and experiment. This work demonstrated interesting properties of EDFA dynamics, previously thought to be limited by the long lifetime of the erbium metastable level. Remote EDFA switching from as far as 50 km away was demonstrated [82]. A comprehensive review of possible applications of this switching effect is still required to determine its practicality. Rapid gain enhancement with high-energy pump pulses should be demonstrated. The observed fiber connector damage should also be studied in detail to give guidelines of the optical damage thresholds of the various connectors.

The effect of stimulated Raman scattering on the transmission of high-power 1550 nm pulses over long single-mode fibers was experimentally and theoretically investigated in Chapter V [86]. It was shown that for a given pulse duration and fiber length, there is an optimum input power that maximizes the energy transfer. This result is not only applicable to remote EDFA switching, but also to other applications requiring high-power pulse transmission [84].

Novel bidirectional amplifiers were proposed in Chapter VI for OTDR testing and bidirectional networks [109], [104]. The fiber amplifier may be incorporated or separated from a frequency dependent optical isolator (FDOI) that is used to allocate frequency bands to the two directions [106]. The preliminary measurements of the FDOI indicate that this device can easily be manufactured with existing commercial components. After packaging the FDOI should be field tested for OTDR testing of unidirectional amplified links.

Bidirectional amplifiers for bidirectional transmission over polarization maintaining fiber were also proposed. This led to the proposal of new all fiber devices for polarization separated reflective star networks in Chapter VII. Experimental testing of these networks and amplifier is required.

Publications, Conference Proceedings, and Patents

1) J. Chrostowski, C. Barnard, P. Myslinski, "Applications of Erbium-Doped Devices," *OSA Annual Meeting*, Toronto, FC2, 1993 [21].

2) P. Myslinski, C. Barnard, X. Pan, Q. Wu, and J. Chrostowski, "Applications of Rare-Earth-Doped Fibers," *IEEE Instrum. Measurements Techniques Conference*, Irvine CA, 1993 [31].

3) C. Barnard, P. Myslinski, J. Chrostowki, and M. Kavehrad, "Analytical Model for Rare-Earth-Doped Fiber Amplifiers and Lasers," to be published in *IEEE J. Quantum Electron.* [44].

4) P. Myslinski, X. Pan, C. Barnard, J. Chrostowski, B.T. Sullivan, and J.F. Bayon, "Q-switched Thulium Doped Fibre Laser," *Opt. Engineering.*, vol. 32, pp. 2025-2030, 1993 [48].

5) P. Myslinski, C.Barnard, G. Cheney, J. Chrostowski, B. Syrett, and J. Glinski, "Nanosecond all-optical gain switching of an erbium-doped fibre amplifier," *Opt. Commun.* vol. 97, pp. 340-346, 1992 [81].

6) C.W. Barnard, P. Myslinski, and J. Chrostowski, "50 km remote all-optical nanosecond gain switching of an erbium-doped fiber amplifier," *CLEO*, CTuF4, Baltimore, 1993 [82].

7) C. Barnard and J. Chrostowski, "Polarization Independent Transmissive/Reflective Optical Switch," U.S. patent application 08/099453, 1993 [84].

8) C.W. Barnard, P. Myslinski, J. Chrostowski, and M. Kavehrad, "Limitations Imposed by Stimulated Raman Scattering on 1550 nm High-Energy Pulse Transmission," to be presented at *ICAPT '94*, Toronto, 1994 [86].

9) C.W. Barnard, J. Chrostowski, and M. Kavehrad, "Bidirectional Fiber Amplifiers," *Photon. Technol. Lett.*, vol. 4, pp. 911-913, 1992 [104].

10) C.W. Barnard, M. Kavehrad, and J. Chrostowski, "Bidirectional Fiber Amplifiers," *Proceedings of the Second IEEE International Workshop on Photonic Networks, Components, and Applications*, Montebello, pp. 2.2.1-2.2.6, 1992 [109].

11) C. Barnard and N. Teitelbaum, "Frequency-Dependent Optical Isolator," U.S. patent 5,280,549; 1994 [106].

References

[1] E. Yoneda, K. Kikushima, and K. Suto, "All-Optical Analog Video Distribution System Using Erbium-Doped Fiber," *Proceedings of the First IEEE International Workshop Photonic Networks, Components, and Applications*, Montebello, pp. 173-182, 1991.

[2] P.W. France, Ed., *Optical Fibre Lasers and Amplifiers*, CRC Press, Boca Raton, 1991.

[3] G. Eisenstein, "Semiconductor Optical Amplifiers," *Proc. IEEE, July '89*, 25, 1989.

[4] J.C. Simon, "Semiconductor Optical Amplifiers," *OFC '90*, San Francisco, Minitutorial ThF1, 1990.

[5] K.T. Koai and R. Olshansky, "Simultaneous Optical Amplification, Detection, and Transmission Using In-Line Semiconductor Laser Amplifiers," *IEEE Photon. Technol. Lett.* vol. 4, pp. 441-443, 1992.

[6] D.J. Malyon and W.A. Stallard, "Bidirectional Multilaser Amplifier System Experiment," *Electron. Lett.*, vol. 25, pp. 1366-1368, 1989.

[7] D. Cotter, "Stimulated Brillouin Scattering in Monomode Optical Fiber," *J. Opt. Commun.* vol. 4, p. 10, 1983.

[8] D. Cotter, "Fibre Nonlinearities in Optical Communications," *Opt. Quant. Electron.*, vol. 19, p. 1, 1986.

[9] G. P. Agrawal, *Nonlinear Fiber Optics*, Academic Press, Toronto, 1989.

[10] A. Penzkofer et al, "High Intensity Raman Interactions," *Prog. Quant. Electr.* vol. 6, p. 55, 1979.

[11] R. H. Stolen et al, "Parametric Amplification and Frequency Conversion in Optical Fibers," *IEEE J. Quant. Elect.* vol. 18, p. 1062, 1982.

[12] K. Washio et al, "Efficient Large-Frequency-Shifted Three-Wave Mixing in Low Dispersion Wavelength Region in Single-Mode Optical Fibre," *Electron. Lett.* vol. 16, p. 658, 1980.

[13] R.M. Jopson, A.H. Gnauck, and R.M. Derosier, "Compensation of Fibre Chromatic Dispersion by Spectral Inversion," *Electron. Lett.* vol. 29, pp. 576-578, 1993.

[14] C.R. Giles, E. Desurvire, "Modeling Erbium-Doped Fiber Amplifiers," *J. Lightwave Technol.*, vol. 9, pp. 271-283, 1991.

[15] R.I. Laming, J.E. Townsend, D.N. Payne, F. Meli, G. Grasso, and E.J. Tarbox, "High-Power

Erbium-Doped-Fiber Amplifiers Operating in the Saturated Regime," *IEEE Photon. Technol. Lett.* vol. 3, pp. 253-255, 1991.

[16] J.F. Massicott, R. Wyatt, B.J. Ainslie, and S.P. Craig-Ryan, "Efficient, High Power, High Gain, Er^{3+} Doped Silica Fibre Amplifier," *Electron. Lett.*, vol. 26, pp. 1038-1039, 1990.

[17] A. Takada, K. Iwatsuki, and M. Saruwatari, "Picosecond Laser Diode Pulse Amplification up to 12 W by Laser Diode Pumped Erbium-Doped Fiber," *IEEE Photon. Technol. Lett.*, vol. 2, p. 122, 1990.

[18] Y. Miyajima, T. Komukai and T. Sugawa, "1.31-1.36 μm Optical Amplification in Nd^{3+}-doped Fluorozirconate Fibre," *Electron. Lett.*, vol. 26, 194-195, 1990.

[19] Y. Ohishi, T. Kanamori, T. Nishi, and S. Takahashi, "A High Gain, High Output Saturation Power Pr^{3+} Doped Fluoride Fiber Amplifier Operating at 1.3 μm," *IEEE Photon. Technol. Lett.*, vol. 3, pp. 715-717, 1991.

[20] S.I. Najafi, Ed., *Introduction to Glass Integrated Optics*, Artech House, Boston, 1992.

[21] J. Chrostowski, C. Barnard, P. Myslinski, "Applications of Erbium-Doped Devices," *OSA Annual Meeting*, Toronto, FC2, 1993.

[22] T. Kitagawa, K. Hattori, K. Shuto, M. Yasu, M. Kobayashi, and M. Horiguchi, "Amplification in Erbium-Doped Silica-Based Planar Lightwave Circuits," *Electron. Lett.* vol. 28, pp. 1818-1819, 1992.

[23] R. Brinkmann, W. Sohler, H. Suche, "Continuous-Wave Erbium-Diffused $LiNbO_3$ Waveguide Laser," *Electron. Lett.*, vol. 27, pp. 415-417, 1991.

[24] E. Lallier, J.-P. Pochelle, M. Papuchon, Q. He, M. De Micheli, D. B. Ostrowsky, C. Grezes-Besset, and E. Pelletier, "Integrated $Nd:MgO:LiNbO_3$ FM Mode-Locked Waveguide Laser," *Electron. Lett.* vol. 27, pp. 936-937, 1991.

[25] G. Nykolak, M. Haner, P.C. Becker, J. Shmulovich, and Y.H. Wong, "Systems Evaluation of an Er^{3+}-Doped Planar Waveguide Amplifier," *IEEE Photon. Technol. Lett.*, vol. 5, pp. 1185-1187, 1993.

[26] T. Feuchter, E.K. Mwarania, J. Wang, L. Reekie, and J.S. Wilkinson, "Erbium-Doped Ion-Exchanged Waveguide Lasers in BK-7 Glass," *IEEE Photon. Technol. Lett.*, vol. 4, pp. 542-544, 1992.

[27] R.J. Mears and S.R. Baker, "Erbium fibre amplifiers and lasers," *Opt. Quantum. Electron.*,

vol. 24, pp. 517-538, 1992.

[28] L.T. Blair and H. Nakano, "High Sensitivity 10 Gbit/s Optical Receiver Using Two Cascaded EDFA Preamplifiers", *Electron. Lett.*, vol. 27, pp. 835-836, 1991.

[29] A.M. Hill, R. Wyatt, J.F. Massicott, K.J. Blyth, D.S. Forrester, R.A. Lobbett, P.J. Smith, D.B. Payne, "39.5 Million-Way WDM Broadcast Network Employing Two Stages of Erbium-Doped Fibre Amplifiers", *Electron. Lett.*, vol. 26, pp. 1882-1884, 1990.

[30] L.F. Mollenauer, B.M. Nyman, M.J. Neubelt, G. Raybon, and S.G. Evangelides, "Demonstration of soliton transmission at 2.4 Gbit/s over 12,000 km," *Electron. Lett.*, vol. 27, pp. 1203-1205, 1990.

[31] P. Myslinski, C. Barnard, X. Pan, Q. Wu, and J. Chrostowski, "Applications of Rare-Earth-Doped Fibers," *IEEE Instrum. Measurements Techniques Conference*, Irvine CA, 1993.

[32] C.J. Koester and E. Snitzer, "Amplification in a Fiber Laser," *Appl. Optics*, vol. 3, pp. 1182-1186, 1964.

[33] G.J. Cowle, D.N. Payne, and D. Reid, "Single-Frequency Travelling-Wave Erbium-Doped Fibre Laser," *Electron. Lett.*, vol. 27, pp. 229-230, 1991.

[34] P. Myslinski, J. Chrostowski, J.A. Koningstein, and J.R. Simpson, "High Power Q-Switched Erbium Fiber Laser," *IEEE J. Quantum Electron.*, vol. 28, pp. 371-377, 1992.

[35] C.Y. Chen, M.M. Choy, M.J. Andrejco, M.A. Saifi, and C. Lin, "A Widely Tunable Erbium-Doped Fiber Laser Pumped at 532 nm," *IEEE Photon. Technol. Lett.*, vol. 2, pp. 18-20, 1990.

[36] R.P. Davey, N.L. Langford, and A.I. Ferguson, "Subpicosecond Pulse Generation from Erbium Doped Fibre Laser," *Electron. Lett.*, vol. 27, pp. 726-728, 1991.

[37] M.J.F. Digonnet, "Closed-Form Expressions for the Gain in Three- and Four-Level Laser Fibers," *IEEE J. Quantum Electron.*, vol. 26, pp. 1788-1796, 1990.

[38] J. Chen, X. Zhu, and W. Sibbett, "Derivation of the Threshold Pump Power of Erbium-Doped Fiber Lasers," *Opt. Lett.*, vol. 17, pp. 926-928, 1992.

[39] M. Mignon and E. Desurvire, "An Analytical Model for the Determination of Optimal Output Reflectivity and Fiber Length in Erbium-Doped Fiber Lasers," *IEEE Photon. Technol. Lett.*, vol. 4, pp. 850-852, 1992.

[40] A.O. Nielsen, J.H. Povlsen, A. Bjarklev, O. Lumholt, T.P. Rasmussen, and K. Rottwitt, "Fast Method for Accurate Prediction of Fibre Laser Oscillation Wavelength," *Electron. Lett.*, vol.

27, pp. 1644-1645, 1991.

[41] P. Urquhart, "Praseodymium-Doped Fiber Amplifiers: Theory of 1.3 μm Operation," *IEEE J. Quant. Elect.* vol. 28, pp. 1962-1965, 1992.

[42] A.A.M. Saleh, R.M. Jopson, J.D. Evankow, and J. Aspell, "Modeling of Gain in Erbium-Doped Fiber Amplifiers," *IEEE Photon. Technol. Lett.*, vol. 2, pp. 714-717, 1990.

[43] T. Pfeiffer, H. Schmuck, and H. Bülow, "Output Power Characteristics of Erbium-Doped Fiber Ring Lasers,"*IEEE Photon. Technol. Lett.*, vol. 4, pp. 847-849, 1992.

[44] C. Barnard, P. Myslinski, J. Chrostowki, and M. Kavehrad, "Analytical Model for Rare-Earth-Doped Fiber Amplifiers and Lasers," to be published in *IEEE J. Quantum Electron.*

[45] S. Oshiba et al, "Recent Progress in InGaAsP High Power Laser," *OFC '90*, San Francisco, TUC1, 1990.

[46] A. Larsson et al, "A 980 nm pseudomorphic Single Quantum Well Laser for Pumping Erbium-Doped Optical Fiber Amplifiers," *IEEE Photon. Technol. Lett.* vol. 2, p. 540, 1990.

[47] W.L. Barnes, R.I. Laming, E.J. Tarbox, and P.R. Morkel, "Absorption and Emission Cross Sections of Er^{3+} Doped Silica Fibres," *IEEE J. Quantum Electron.*, vol. 27, pp. 1004-1010, 1991.

[48] P. Myslinski, X. Pan, C. Barnard, J. Chrostowski, B.T. Sullivan, and J.F. Bayon, "Q-switched Thulium Doped Fibre Laser," *Opt. Engineering.*, vol. 32, pp. 2025-2030, 1993.

[49] J.Y. Allain, M. Monerie, and H. Poignant, "Ytterbium-Doped Fluoride Fibre Laser Operating at 1.02 μm"

[50] R. Reisfeld and C.K. Jorgensen, *Lasers and Excited States of Rare Earths*, Springer Verlag, New York, 1977.

[51] M.J.F. Digonnet and C.J. Gaeta, "Theoretical Analysis of Optical Fiber Laser Amplifiers and Oscillators," *Appl. Opt.*, vol. 24, pp. 333-342, 1985.

[52] T. Pfeiffer and H. Bülow, "Analytical Gain Equations for Erbium-Doped Fiber Amplifiers Including Mode Field Profiles and dopant Distribution," *IEEE Photon. Technol. Lett.*, vol. 4, pp. 449-451, 1992.

[53] I.M.I. Habbab and L.J. Cimini Jr., "Optimized Performance of Erbium-Doped Fiber Amplifiers in Subcarrier Multiplexed Lightwave AM-VSB CATV Systems," *J. Lightwave Technol.*, vol. 9, pp. 1321-1329, 1991.

[54] P.R. Morkel and R.I. Laming, "Theoretical Modeling of Erbium-doped Fiber Amplifiers with Excited-State Absorption," *Opt. Lett.*, vol. 14, pp. 1062-1064, 1989.

[55] B. Pedersen, S.A. Zemon, and W.J. Miniscalco, "Analysis of Erbium-Doped Fiber Amplifiers Pumped at 800 nm," *SPIE* vol. 1581, pp. 293-302, 1991.

[56] R.I. Laming, S.B. Poole, and E.J. Tarbox, "Pump excited-state absorption in erbium-doped fibers," *Opt. Lett.* vol. 13, pp. 1084-1086, 1988.

[57] E. Desurvire, "Analysis of Distributed Erbium-Doped Fiber Amplifiers with Fiber Background Loss," *IEEE Photon. Technol. Lett.*, vol. 3, pp. 625-628, 1991.

[58] W.J. Miniscalco, "Very High Gain Er^{3+} Fiber Amplifier Pumped at 980 nm," *OFC '90*, San Francisco, FA2, 1990.

[59] W.L. Barnes, P.R. Morkel, L. Reekie, and D.N. Payne, "High-Quantum-Efficiency Er^{3+} Fiber Lasers Pumped at 980 nm," *Opt. Lett.*, vol. 14, pp. 1002-1004, 1989.

[60] A.E. Willner, E. Desurvire, H. M. Presby, C.A. Edwards, and J. R. Simpson, "Use of LD-Pumped Erbium-doped fiber Preamplifiers with Optimal Noise Filtering in a FDMA-FSK 1 Gb/s Star Network," *IEEE Photon. Technol. Lett.*, vol. 2, p. 669, 1990.

[61] N.A. Olsson, "Lightwave Systems with Optical Amplifiers," *J. Lightwave Technol.*, vol. 7, p. 1071, 1989.

[62] G. Herzberg, *Atomic Spectra & Atomic Structure*, Dover Publications, New York, 1944.

[63] E. Desurvire and J.R. Simpson, "Amplification of Spontaneous Emission in Erbium Doped Single-Mode Fibers," *J. Lightwave Tech.*, vol. 7, pp. 835-845, 1989.

[64] J. N. Sandoe et al, "Variation of Er^{3+} cross section for stimulated emission with glass composition," *J. Phys. D*, vol. 5, p. 1788, 1972.

[65] W. Koechner, *Solid-Sate Laser Engineering*, Springer-Verlag, New York, 1988.

[66] D.E. McCumber, "Theory of Phonon-Terminated Optical Masers," *Phys. Rev.*, vol. 134, pp. A299-A305, 1964.

[67] W.J. Miniscalco and R. S. Quimby, "General Procedure for the Analysis of Er^{3+} Cross-Sections," *Opt. Lett.*, vol. 16, pp. 258-260, 1991.

[68] R.I. Laming, "Noise Characteristics of Erbium-Doped Fiber Amplifier Pumped at 980 nm," *IEEE Photon. Technol. Lett.*, vol. 2, pp. 418-421, 1990.

[69] T. Okoshi and K. Kikuchi, *Coherent Optical Fiber Communications,* Kluwer Academic

Publishers, Norwell, MA, 1988.

[70] B.E.A. Saleh and M.C. Teich, *Fundamentals of Photonics*, John Wiley, Toronto, 1991.

[71] R.M. Gagliardi and S. Karp, *Optical Communications*, John Wiley, Toronto, 1976.

[72] T. Okoshi, "Exact Noise-Figure Formulas for Optical Amplifiers and Amplifier-Fiber Cascaded Chains," *IEEE/OSA Topical Meeting on Optical Amplifiers and their Applications, Monterrey*, PDP11, 1990.

[73] J. L. Gimlett, M.Z. Iqbal, J. Young, L. Curtis, R. Spicer, and N. K. Cheung, "11 Gbit/s Optical Transmission Experiment using 1540 nm DFB Laser with Non-Return-to Zero Modulation and pin/HEMT Receiver," *Electron. Lett.*, vol. 25, p. 596, 1989.

[74] P.A. Humblet and M. Azizoglu, "On the Bit Error Rate of Lightwave Systems with Optical Amplifiers," *J. Lightwave Technol.*, vol. 9, pp. 1576-1582, 1991.

[75] B.P. Cavanagh, I.W. Marshall, G. Sherlock, and H. Wickes, "Comparison of Bulk Buried Heterostructure and Multiple Quantum Well Laser Amplifier Switches," *Electron. Lett.*, vol. 27, pp. 263-265, 1991.

[76] E. Desurvire, "Erbium-Doped Fiber Amplifiers: Basic Physics and Theoretical Modeling," *Int. J. of High Speed Electron.* vol. 2, pp. 89-114, 1991.

[77] M. Zirngibl, "All-Optical Remote Gain Switching in Er-doped Fibre Amplifiers," *Electron. Lett*, vol. 27, pp. 1164-1166, 1991.

[78] E. Desurvire, C.R. Giles, and J.R. Simpson, "Gain Dynamics of Erbium-Doped Fiber Amplifiers," *SPIE*, vol. 1171, pp. 103-117, 1989.

[79] P. Myslinski, G. Cheney, J. Chrostowski, B. Syrett, and J. Glinski, "Nanosecond All-Optical Gain Switching of an Erbium-Doped Fibre Amplifier," *Proceedings of the Second IEEE International Workshop on Photonic Networks, Components, and Applications*, Montebello (1992), pp. 1.10.1-1.10.6.

[80] E. Desurvire, "Analysis of Transient Gain Saturation and Recovery in Erbium-Doped Fiber Amplifiers," *IEEE Photon. Technol. Lett.*, vol. 1, pp. 196-199, 1989.

[81] P. Myslinski, C.Barnard, G. Cheney, J. Chrostowski, B. Syrett, and J. Glinski, "Nanosecond all-optical gain switching of an erbium-doped fibre amplifier," *Opt. Commun.* vol. 97, pp. 340-346, 1992.

[82] C.W. Barnard, P. Myslinski, and J. Chrostowski, "50 km remote all-optical nanosecond gain

switching of an erbium-doped fiber amplifier," *CLEO*, CTuF4, Baltimore, 1993.

[83] T.C. Banwell, R.C. Estes, L. A. Reith, P.W. Shumate, E.M. Vogel, "Powering the Fiber Loop Optically - A Cost Analysis," *J. Lightwave Technol.*, vol. 11, pp. 481-494, 1989.

[84] C. Barnard and J. Chrostowski, "Polarization Independent Transmissive/Reflective Optical Switch," U.S. patent application 08/099453, 1993.

[85] M. Ikeda, "Stimulated Raman Amplification Characteristics in Long Span Single-Mode Silica Fibers", *Opt. Commun.* vol. 39, pp. 148-152, 1981.

[86] C.W. Barnard, P. Myslinski, J. Chrostowski, and M. Kavehrad, "Limitations Imposed by Stimulated Raman Scattering on 1550 nm High-Energy Pulse Transmission," to be presented at *ICAPT '94*, Toronto, 1994.

[87] D. Schadt, *Contributions to Nonlinear Pulse Propagation in Single Mode Optical Fibers*, Ph. D. Thesis, The Royal Institute of Technology, Stockholm, 1989.

[88] B.S. Kawasaki, K.O. Hill, D.C. Johnson, and A.U. Tenne-Sens, "Full Duplex Transmission Link over Single-Strand Optical Fiber," *Opt. Lett.*, vol. 1, pp. 107-108, 1977.

[89] R.J.S. Bates, J.D. Spalink, S.J. Butterfield, J. Lipson, C.A. Burrus, T.P. Lee, and R.A. Logan, "1.3/1.5 µm Bidirectional WDM Optical-Fibre Transmission System Experiment at 144 Mbit/s," *Electron. Lett.*, vol. 19, pp. 458-459, 1983.

[90] N. Kashima, "A New Approach to an Optical Attenuator for a Time compression Multiplex System Using a Laser Diode as Both Transmitter and Receiver," *J. Lightwave Technol.*, vol. 9, pp. 987-990, 1991.

[91] P.A. Andrekson and N. A. Olsson, "Optical Full-Duplex Transmission with Diode Laser Amplifiers," *J. Lightwave Technol.*, vol. 9, pp. 737-740, 1991.

[92] N. Kashima, "Properties of Commercial 1.3 µm Fabry-Perot Laser Modules in a Time compression Multiplexing System," *J. Lightwave Technol.*, vol. 9, pp. 918-923, 1991.

[93] Y. Sasaki, K. Tajima, and I. Yokohama, "Bidirectional Optical Transmission Using Polarised Light Waves," *Electron. Lett.*, vol. 23, pp. 692-694, 1987.

[94] A.S. Siddiqui and J. Zhou, "Two-Channel Optical Fiber Transmission using Polarization Division Multiplexing," *J. Opt. Commun.*, vol. 12, pp. 47-49, 1991.

[95] L.C. Blank and J.D. Cox, "Optical Time Domain Reflectometry on Optical Amplifier Systems," *J. Lightwave Technol.*, vol. 7, pp. 1549-1555, 1989.

[96] P.A. Rosher, S.C. Fenning, P. Cochrane, and A.R. Hunwicks, "An Automatic Optical Fibre Break Location Scheme for Duplex and Diplex Transmission Systems," *Br. Telecom. Technol. J.*, vol. 6, pp. 54-59, 1988.

[97] B.C. Clarke, "The Effect of Reflections on the System Performance of Intensity Modulated Laser Diodes," *J. Lightwave Technol.*, vol. 9, pp. 741-749, 1991.

[98] J.L. Gimlett, M.Z. Iqbal, L. Curtis, N.K. Cheung, A. Righetti, F. Fontana, G. Grasso, "Impact of Multiple Reflection Noise in Gbit/s Lightwave Systems with Optical Fibre Amplifiers," *Electron. Lett.*, vol. 25, pp. 1393-1394, 1989.

[99] E. Brinkmeyer, "Backscattering in Single-Mode Fibres", *Electron. Lett.*, vol. 16, pp. 329-330, 1983.

[100] L.J. Baskerville, "Two Fibers or One? (A Comparison of Two-Fiber and One-Fiber Star Architectures for Fiber-to-the-Home Applications)," *J. Lightwave Technol.*, vol. 7, pp. 1733-1740, 1989.

[101] A. A. M. Saleh and H. Kogelnik, "Reflective Single-Mode Fiber-Optic Passive Star Couplers," *J. Lightwave Technol.*, vol. 6, pp. 392-397, 1988.

[102] M. Suyama, S. Watanabe, I. Yokota, and H. Kuwahara, "Bidirectional Transmission Scheme Using Intensity Modulation of 1.48 μm Pump Laser Diode for Erbium-Doped Fibre Amplifier", *Electron. Lett.*, vol. 27, pp. 89-91, 1991.

[103] Y. Sato and K. Aoyama, "OTDR in Optical Transmission Systems Using Er-Doped Fiber Amplifiers Containing Optical Circulators," *IEEE Photon. Technol. Lett.*, vol. 3, p. 1001, 1991.

[104] C.W. Barnard, J. Chrostowski, and M. Kavehrad, "Bidirectional Fiber Amplifiers," *Photon. Technol. Lett.*, vol. 4, pp. 911-913, 1992.

[105] J. Stone and L.W. Stulz, "FiEnd Filters: Passive Multilayer Thin-Film Optical Filters Deposited on Fibre Ends," *Electron. Lett.*, vol. 26, pp. 1290-1291, 1990.

[106] C. Barnard and N. Teitelbaum, "Frequency-Dependent Optical Isolator," U.S. patent 5,280,549; 1994.

[107] M. Martinelli, "A Universal Compensator for Polarization Changes Induced by Birefringence on a Retracing Beam," *Opt. Commun*, vol. 72, pp. 341-344, 1989.

[108] T. Morioka, H. Takara, K.Mori and M. Saruwatari, "Ultrafast Reflective Optical Kerr

Demultiplexer Using Polarisation Rotation Mirror," *Electron. Lett.*, vol. 28, pp. 521-522, 1992.

[109] C.W. Barnard, M. Kavehrad, and J. Chrostowski, "Bidirectional Fiber Amplifiers," *Proceedings of the Second IEEE International Workshop on Photonic Networks, Components, and Applications*, Montebello, pp. 2.2.1-2.2.6, 1992.

[110] J. Noda, K. Okamoto, and Y. Sasaki, "Polarization-Maintaining Fibers and Their Applications," *J. Lightwave Technol.*, vol. 4, p. 1071, 1986.

[111] M. Eisenmann and E. Weidel, "Single-Mode Fused Biconical Coupler Optimized for Polarization Beamsplitting," *J. Lightwave Technol.*, vol. 9, pp. 853-858, 1991.